

August 2016

Nano-Crystalline Metal Matrix Nano-Composites Reinforced By Graphene and Alumina: Effect of Reinforcement Properties and Concentration on Mechanical Behavior

Meysam Tabandeh Khorshid
University of Wisconsin-Milwaukee

Follow this and additional works at: <https://dc.uwm.edu/etd>

 Part of the [Materials Science and Engineering Commons](#)

Recommended Citation

Tabandeh Khorshid, Meysam, "Nano-Crystalline Metal Matrix Nano-Composites Reinforced By Graphene and Alumina: Effect of Reinforcement Properties and Concentration on Mechanical Behavior" (2016). *Theses and Dissertations*. 1314.
<https://dc.uwm.edu/etd/1314>

This Dissertation is brought to you for free and open access by UWM Digital Commons. It has been accepted for inclusion in Theses and Dissertations by an authorized administrator of UWM Digital Commons. For more information, please contact open-access@uwm.edu.

**NANO-CRYSTALLINE METAL MATRIX NANO-COMPOSITES REINFORCED BY
GRAPHENE AND ALUMINA:
EFFECT OF REINFORCEMENT PROPERTIES AND CONCENTRATION ON MECHANICAL
BEHAVIOR**

by

Meysam Tabandeh-Khorshid

A Dissertation Submitted in
Partial Fulfillment of the
Requirements for the Degree of

Doctor of Philosophy

in Engineering

at

The University of Wisconsin-Milwaukee

August 2016

ABSTRACT

NANO-CRYSTALLINE METAL MATRIX NANO-COMPOSITES REINFORCED BY GRAPHENE AND ALUMINA: EFFECT OF REINFORCEMENT PROPERTIES AND CONCENTRATION ON MECHANICAL BEHAVIOR

by

Meysam Tabandeh-Khorshid

The University of Wisconsin-Milwaukee, 2016
Under the Supervision of Professor Pradeep K. Rohatgi

Metal matrix composites (MMCs) and Metal Matrix Nano-composites (MMNCs) are promising materials for a number of aerospace, defense, and automobile applications. Among all MMCs and MMNCs, aluminum is the most widely used matrix due to its low density coupled with high stiffness, high specific strength, high specific modulus and low thermal expansion coefficient. While high strengths have been shown in MMCs, they are known to have very limited ductility. However, there are indications that reducing reinforcement size to the nanoscale may improve strain to failure in addition to increase strength. Reducing grain size to the nanoscale has been found to improve material properties specially strength until grain size of around 10 nm. From this preliminary evidence, it would appear that nanocrystalline (NC) metallic materials and NC MMNCs may result in the best properties. Yet, in these materials, the effect of processing conditions and reinforcement type, size, and concentration on material performance is not well understood.

Currently, mainly Powder Metallurgy (PM) techniques appear to be capable of generating NC metallic materials. Milling is used to mix matrix and reinforcement particles as well as reduce the size of particles. The majority of work in synthesizing NC metallic materials has employed

cryomilling, which is milling of the metallic powders in a medium of liquid nitrogen (LN2) using stearic acid as a process control agent (PCA). After cryomilling, the milled powder is nanosize, but requires a high temperature/high vacuum degassing step to remove the PCA. However, there are several medium/PCA combinations that could be used that may produce the same results as the relatively complex and expensive LN2/Stearic acid combination. To date, these alternatives remain unexplored.

To consolidate the milled powders techniques such as HIP, CIP, single action compaction, extrusion, and forging can be used. However, to achieve close to theoretical densities it is necessary to perform the consolidation at high temperature. The high temperature causes coarsening of the powder grains and results in a larger grain size. Since it appears that the grain size is one of the main factors in determining the strength and ductility of the material, it is important to understand how reinforcement additions affect grain growth. Furthermore, plastic deformation seems to be required to achieve maximum density. Plastic deformation results in work hardening, which strengthens the material at the expense of ductility. The effect of reinforcement additions on work hardening has also received limited attention.

In order to better understand the effect of reinforcement type, size, and concentration on the processing and mechanical behavior of NC metals and MMNCs, pure Al was mixed with varying concentrations of graphene nanoplatelets (GNPs) and 47 nm alumina nanoparticles ($\text{Al}_2\text{O}_{3\text{np}}$). Instead of cryomilling, milling was conducted at room temperature in ethanol, where ethanol acted as both the medium and PCA. Degassing was accomplished by heating to only 135°C rather than to several hundred degrees. This processing method is considerably less complex and therefore less expensive and results in milled powders of the same size as those achieved by cryomilling followed by high temperature/high vacuum degassing.

The consolidation of the powders was conducted by single action cold compaction and single action hot compaction. This method should minimize textural effects that are produced by other consolidation techniques such as extrusion. Relative density (i.e. the density of the sample divided by the theoretical density) of the final consolidated samples reached nearly 100% in all graphene-reinforced samples regardless of graphene concentration; whereas in $\text{Al}_2\text{O}_{3\text{np}}$ -reinforced samples the achievable densities were in the range of 85-95% of theoretical density depending on $\text{Al}_2\text{O}_{3\text{np}}$ concentration. These are similar to the relative densities achieved by LN2 cryomilling/HIP/extrusion processing and shows that the room temperature ethanol/cold compaction/hot compaction is a viable alternative synthesis method.

As stated above, mechanical properties of the material are primarily governed by grain size and work-hardening and that it is likely that reinforcement additions have a significant effect on these properties. To understand the strengthening mechanisms of MMNCs, pure NC Al was reinforced with varying concentrations of $\text{Al}_2\text{O}_{3\text{np}}$ and GNPs. The results show that i) room temperature milling in ethanol followed by a relatively low temperature drying treatment can produce NC Al and NC Al MMNCs with grain sizes comparable to materials produced by cryomilling, ii) grain boundary strengthening as described by the Hall-Petch relation accounts for the strength of Al- $\text{Al}_2\text{O}_{3\text{np}}$ MMNCs, and iii) grain boundary strengthening, solute strengthening, and CTE mismatch strengthening also appear to contribute to the strength in Al-GNP MMNCs. To investigate the tribological behavior of aluminum matrix composites reinforced by GNPs and pure aluminum, pin-on-disk experiments were conducted on samples synthesized in the study. In the experiments, the influence of reinforcement, volume fraction, normal load, and sliding velocity on the tribological performance was investigated. Results showed that the wear rate of Al-1wt.% GNP is increased with increasing normal loads. However, the coefficient of friction (COF) of the Al-

1wt.% GNP decreased with increasing normal loads. Formation of carbon film on the worn surface of Al-1wt.% GNP sample and morphology of the worn surfaces of aluminum and composite samples were analyzed by Optical Microscope (OM) and Scanning Electron Microscope (SEM). It was found that the graphene nanoplatelets reinforced nano-composites showed superior tribological properties and demonstrated the ability of the self-lubricating nature of the composite during tribological conditions.

Moreover, diametrical compression of small disk specimens was used to understand the mechanical properties of metal matrix nano composites. Analysis was performed using an inverse method that couples digital image correlation and the analytical closed form formulation. This technique was capable of extracting the tension and compression modulus values in the metal matrix nanocomposite disk specimens. This method for characterization of metal matrix composites have the potential to accelerate the development and study of advanced composite materials.

© Copyright by Meysam Tabandeh-Khorshid, 2016
All Rights Reserved

To
My Parents

TABLE OF CONTENTS

ABSTRACT	ii
LIST OF FIGURES.....	x
LIST OF TABLES.....	xvii
1. Introduction.....	2
1.1. Composite Materials	2
1.1.1. Metal Matrix Composites (MMCs)	3
1.1.2. Metal Matrix nano-Composites (MMNCs).....	3
1.2. Processing of MMCs and MMNCs	4
1.2.1. Vapor deposition.....	4
1.2.2. Liquid state processing	5
1.2.3. Solid state processing.....	7
1.2.3.1. Consolidating	10
1.2.3.1.1. Cold compaction	10
1.2.3.1.2. Hot compaction	11
1.3 Strengthening mechanisms of MMCs and MMNCs	13
1.3.1 Grain refinement strengthening.....	13
1.3.2. Orowan strengthening mechanism	14
1.3.3. Coefficient of Thermal Expansion (CTE) mismatch.....	15
2. Literature Review	18
2.1. Producing MMCs and MMNCs by powder metallurgy method.....	18
2.2. Graphene	18
2.3. Synthesizing Metal Matrix Composites reinforced by Graphene	21
2.3.1. Liquid State Processing to synthesize MMNCs reinforced by Graphene	21
2.3.2. Solid State Processing to synthesize MMNCs reinforced by Graphene	22
2.4. Characterization of MMNCs reinforced by Graphene.....	25
2.5. Properties of MMNCs reinforced by Graphene	32
2.5.1. Mechanical Properties and Strengthening Mechanisms.....	33
2.5.2. Tribological Properties	40
2.6. Cryomilling.....	40
2.7. Predicting Mechanical Properties of MMCs and MMNCs.....	44
2.7.1. Young's Modulus	44
2.7.2. Yield strength.....	48
3. Experimental Procedure.....	53
4. Results and Discussion	59
4.1. Characterization.....	59
4.2. Grain Size Measurements	75
4.3. Mechanical Properties	79
4.3.1. Hardness Measurements	79
4.3.2. Compression Test Results.....	83
4.4. Strengthening Mechanisms.....	85
4.5. Tribological properties	91

4.6.	Diametrically loaded cylinder for the study of NS MMNCs using Digital Image Correlation (DIC)	100
4.6.1.	Preliminary study	101
4.6.2.	Theory	101
	Analytical solution of diametrically loaded cylinder.....	101
	Diametrically loaded cylinder experiments using DIC	104
4.6.3.	Results	106
4.6.4.	Limitations.....	110
5.	Summary and Conclusion	112
6.	References	117
7.	CURRICULUM VITAE.....	131

LIST OF FIGURES

Figure 1. Schematic illustration to show different types of Liquid State Processing method; a) Stir Casting, b) Squeeze Casting, and c) Pressure Infiltration [1].	6
Figure 2. Different types of ball mill; a) planetary ball mill, b) attritor mill, c) Spex high energy ball mill, and d) cryomill [2].....	9
Figure 3. Cold compaction methods; a) Cold Isostatic Press (CIP), and b) Single action cold compaction [1].	11
Figure 4. Schematic of hot consolidation processing; a) hot extrusion, b) hot forging, and c) hot rolling [1].	12
Figure 5. Orowan strengthening mechanism a) Dislocation moving toward particles, b) Dislocation passing the particles, and c) Formation of loops around particles.	14
Figure 6. Schematic of the processing procedure to obtain graphene nanoplatelets reinforced metal matrix nanocomposites [32].....	22
Figure 7. Optical micrographs of extruded pure Al and Al–0.1 wt% graphene [17].	26
Figure 8. a) Secondary electron FESEM micrograph of the multilayered morphology of graphene nanoplatelets [20], b) TEM image of few-layers graphene [18], c) SEM image of few layered graphene (FLG) attached to Al powder using a planetary mill at 100 RPM (FLG is marked by an arrow) [35], d) SEM image of FLG embedded and dispersed in Al powder using an attrition mill at 500 RPM [35].....	26
Figure 9. a) SEM surface image of Mg–1.5Al–0.18GNP [34], b) SEM image of Al/0.3wt%GNP composite [19], c) and d) SEM images of Mg matrix composites reinforced by GNP synthesized by ultrasonic processed + solid state stirred at different magnifications [32].	27

Figure 10. a) Fracture surface of 0.3 wt.% GNP/Al composite; the inset shows the GNS pulled out [16], b) Mg, c) Mg–0.5Al–0.18GNP, and d) Mg–1.5Al–0.18GNP composite [34].	28
Figure 11. a) TEM image of hot-rolled Al/0.3 vol% composite. White arrows are graphene nanoplatelets and highly deformed regions are shown by circle [35], b) HRTEM image of the graphene nanoplatelet embedded in the magnesium matrix [32], c) and d) TEM image of hot-rolled Al/0.3 vol% composite. Number of layers of FLGs show by red lines [35].	29
Figure 12. a) SEM image of an Al flake surface with adsorbed GO nanosheets; b) the EDS of selected area in (a) [16].	30
Figure 13. a) X-Ray diffraction of pure aluminum, Al-1.0wt% MWNT composite, and Al-0.1wt% graphene composite after extrusion [17], b) XRD of GNP, pure Mg and Mg-xAl-0.18GNP composites (x=0.5; 1.0; 1.5) [34].	31
Figure 14. a) Raman spectrum of initial graphite powder, exfoliated graphite powder and hot-rolled Al/FLG composites [35], b) Raman spectra of single- and double-layer graphene [36]. ..	32
Figure 15. Hardness measurements of MMNCs reinforced by graphene [32] [17] [19] [34] [20].	34
Figure 16. Yield, UTS and Compression strength of MMNCs reinforced by GNP [17] [16] [19] [34] [35].	34
Figure 17. Effect of milling time on Flexural Strength of aluminum matrix composites reinforced by GNPs [18].	35
Figure 18. Theoretical prediction of yield strength of composite materials based on different models and an experimental result [35] [42] [43] [44] [45].	39
Figure 19. a) Schematic design of a typical cryomilling attritor mill and b) the cryomilling attritor mill which used for producing Al-Al ₂ O ₃ [51].	42

Figure 20. Schematic representation of grain refinement mechanism during ball milling in microscopic level for an individual grain [58].	42
Figure 21. Grain size as a function of milling time for cryomilled and ball milled powders [59] [60] [61] [62].	43
Figure 22. True tensile stress as a function of true strain of cryomilled 5083 Al alloys consolidated with different consolidation methods including CIP + ext, HIP + ext1 [52].	43
Figure 23. Prediction of young's Modulus of composites versus particles volume fraction at different degrees of bonding.	47
Figure 24. Percentage of change in Young's Modulus of the compsoites versus particle volume fraction.	48
Figure 25. Prediction of yield strength of the composites versus particle volume fraction.	50
Figure 26. Percentage of change in Yield Strength of the composites versus particle volume fraction.	51
Figure 27. Schematic illustrations to show the attritor milling powder processing technique at room temperature.	54
Figure 28. SEM micrograph of aluminum powders at different magnifications a) 400X and b) 1500X.	59
Figure 29. SEM micrograph of alumina nanoparticles at different magnifications a) 70000X, b) 150000X.	59
Figure 30. SEM micrograph of Graphene nanoplatelets at different magnifications a) 3000X, b) 5000X, c) 20000X and d) 20000X.	60
Figure 31. Relative density measurements of different samples from Archimedes method.	60

Figure 32. SEM morphology of milled powders. a) Pure aluminum at 1000X, b) pure aluminum at 2000X, and c) aluminum-1%GNP at 4500X after 6 hours of milling.	61
Figure 33. XRD spectrum of aluminum powder after 6 hours of ball milling.	63
Figure 34. XRD spectrum of Al-5%Al ₂ O ₃ with average particle size of 47nm composite powders milled for 6hr.	63
Figure 35. XRD spectrum of Al-1%graphene nanoplatelets composite powders milled for 6hr.	64
Figure 36. XRD spectrum of hot compacted pure aluminum sample.....	64
Figure 37. XRD spectrum of hot compacted Al-5%Al ₂ O ₃ composite sample.	65
Figure 38. XRD spectrum of hot compacted Al-1% graphene nanoplatelets composite sample.	65
Figure 39. XRD patterns of pure Al (black) and Al-matrix composites reinforced by 1 wt.% GNP before (blue) and after (red) heat treatment.	66
Figure 40. XRD results of as received GNPs [71]......	67
Figure 41. SEM micrographs of the fractured sections from (a) pure Al, (b) Al-1 wt.% GNP, and (c) and (d) Al-5 wt.% Al ₂ O ₃ samples with different magnifications.....	68
Figure 42. (a) SEM micrograph of the fractured Al-1%GNP specimen and the corresponding EDS dot maps of (b) C (red) and (c) Al (blue) elements.	69
Figure 43. EDS intensity plots from the fractured sections of (a) Al-5 wt.% Al ₂ O ₃ and (b) Al-1 wt.% GNP.	69
Figure 44. TEM images of pure aluminum sample to show a) and b) microstructures at different magnifications, c) oxygen enriched locations, and d) dislocation structure.	70
Figure 45. TEM images of Al-5%Al ₂ O ₃ sample to show a) and b) layered microstructures at different magnifications, c) dislocation structures in bright field and d) dislocation structures in dark field.	71

Figure 46. TEM images of Al-5%Al ₂ O ₃ sample to show a) and b) alumina nanoparticles in the layered microstructures at different magnifications, c) and d) the EDS results on the aluminum matrix and alumina nanoparticles respectively.....	72
Figure 47. TEM images to show the microstructures and grain size distributions of Al-1%GNP samples with increasing magnifications. Embedded GNPs and Al matrix are indicated using red and blue arrows, respectively, in (c) and (d).....	73
Figure 48. Selected Area Diffraction Pattern (SAD) on Al-1%GNP sample.	74
Figure 49. a) and b) TEM images of Al-5%GNP at different magnifications.....	74
Figure 50. The distance between layers of graphene in Al-5%GNPs sample.	75
Figure 51. Crystallite size measurements of pure aluminum, aluminum matrix composites reinforced by graphene nanoplatelets and aluminum matrix composites reinforced by nano alumina particles using Scherrer equation.	76
Figure 52. $\Delta D_{\text{milling}}$ ($D_{\text{As-Received}} - D_{\text{milling}}$) versus weight fraction of the milled powders.	77
Figure 53. Percentage of grain growth after single action hot compaction for pure aluminum and composite samples.	77
Figure 54. Average grain sizes of pure Al, Al-1 wt.% GNP, and Al-5 wt.% Al ₂ O ₃ characterized using XRD and TEM analyses.....	78
Figure 55. Young's Modulus measurements by nano indenter for selected samples.....	81
Figure 56. Hardness measurements by nano indenter for selected samples.	81
Figure 57. Hardness results from nano indenter test and Hardness Rockwell F measurements for selected samples.....	82
Figure 58. Variation of (a) HR_F with annealing time for NC pure aluminum and NC MMNC samples and (b) time constant, τ , with Al ₂ O ₃ concentration.....	83

Figure 59. Ultimate compression strength (UCS) results of Al-Al ₂ O ₃ samples.	84
Figure 60. Ultimate compression strength (UCS) results of Al-GNPs samples.	85
Figure 61. TEM results of clustered GNPs in the Al-5%GNPs.....	85
Figure 62. Variation of HR _F with inverse square root of grain size for NC pure aluminum and NC MMNCs after consolidation and after annealing heat treatments. The average hardness vs. inverse square root of grain size measurements for the Annealed Al-GNP specimens were unchanged as shown in Table 5 and thus are not included in this figure.....	88
Figure 63. Variation of COF with normal load at sliding speed of 100 rpm for pure Al, Al-0.1wt.% GNP and Al-1wt.% GNP.....	92
Figure 64. Variation of wear rate with normal load (N) at sliding speed of 100 rpm for pure Al, Al-0.1wt.% GNP and Al-1wt.% GNP.	93
Figure 65. Optical micrographs of worn surfaces of (a) pure aluminum and (b) Al- 1wt.% GNPs.	94
Figure 66. Variation of COF with sliding speed at different normal loads for Al-1wt.%GNP....	95
Figure 67. Variation of wear rate with sliding speed at different normal loads for Al- 1wt.% GNP.....	96
Figure 68. SEM micrograph of Al-1 Wt.% GNP at different loads and sliding speeds at magnification of 100X. (The sliding direction is from bottom to top in the SEM images).....	97
Figure 69. SEM micrographs of the worn surfaces of different samples at speed of 100 rpm and load of 5 N at magnification of 200X.	98
Figure 70. (a) SEM micrographs and (b) EDS results of wear debris of Al-1 Wt.% GNP sample.	99
Figure 71. A cylinder shape sample subjected to compression load P.	102

Figure 72. Schematic of diametrically loaded cylinder and location of the cameras.	105
Figure 73. DIC results of shear strain in the elastic region (left column) and before failure (right column) for a) pure aluminum, b) Al-5%Al ₂ O ₃ , and c) Al-5%GNP.	107
Figure 74. Stress versus shear strain from DIC results for pure aluminum and Al-5%Al ₂ O ₃	108
Figure 75. Stress versus transverse strain from DIC results for pure aluminum and Al-5%Al ₂ O ₃	108
Figure 76. Schematic of microstructure interactions of a) Al and b) Al-5%Al ₂ O ₃	109

LIST OF TABLES

Table 1. Physical and mechanical properties of Graphene.	19
Table 2. Summary of powder metallurgy method to synthesize MMNCs reinforced by graphene.	24
Table 3. Different theoretical models for prediction of MMCs strength.....	38
Table 4. Crystallite size measurements of pure aluminum, aluminum matrix composites reinforced by graphene nanoplatelets and aluminum matrix composites reinforced by nano alumina particles using Scherrer equation.	75
Table 5. HRF measurements and standard deviation for pure aluminum and composite samples.	80
Table 6. Summary of modulus from diametrical disk compression test.....	106

ACKNOWLEDGEMENTS

Firstly, I would like to express my sincere gratitude to my advisor Prof. Pradeep Rohatgi for his continuous support and help in my PhD study and related research.

I would like to thank my co-advisor Dr. C.-S. Kim for his support, feedback, and help in preparation of scientific paper.

Beside my advisor, I would like to thank my dissertation committee Prof. H. Lopez, and Prof. R. Amano for their support, feedback, and for their participation in my committee. I also want to thank Dr. R. El-hajjar for his support, feedback, help in preparation of scientific paper and for his participation in my committee.

My sincere thanks also goes to Dr. J.B. Ferguson and Dr. Benjamin Schultz who helped me a lot since January 2012, when I joined Prof. Rohatgi's group. Without their precious support it would not be possible to conduct this research.

I would like to thank Shelley Fowler for her kindness help and moral support and wish her peace in heaven.

Special thanks to Dr. S. Hardcastle in AAF at UW-Milwaukee for his support in SEM and XRD work and Dr. H. Owen from biological sciences department at UW-Milwaukee for her support in SEM.

Special thanks to Dr. Sohn and his PhD student Le Zhou at University of Central Florida for providing TEM facilities and support.

I would like to thank the technicians in the machine shop at UW-Milwaukee, especially Mr. John Condon for their help preparing samples for my research.

I thank my fellow labmates, the students of the Center for Composite Materials at UW-Milwaukee and my friends for their help and support.

Last but certainly not least, I would like to thank my family: my parents, my brother and sister, and my fiancée for their love and support.

Chapter 1.

Introduction

1. Introduction

1.1.Composite Materials

Composite materials are engineered or naturally occurring materials which contain two or more distinct materials with significantly different chemical, physical and mechanical properties. The individual materials that make composites are called constituents. The physical, chemical and mechanical properties of each constituent material remain separate at the microscopic and macroscopic scale within the finished structure of composites and this is one of the most important benefits of composite materials compared to alloys. These constituents work together to improve the properties of the composites.

Generally, composites have two parts: matrix and reinforcement. The matrix holds the reinforcements in composites. The reinforcement is usually stronger and stiffer than the matrix, and gives the composite its good properties. Once the size of one of these parts is in the range of nanometers, the composite is called nano-composite. There are different classifications for composite materials reference to the shape, size and type of matrix and reinforcement. One classification is based on type of matrix and according to this one there are three types of composites:

1. Metal Matrix Composites (MMCs)
2. Ceramic Matrix Composites (CMCs)
3. Polymer Matrix Composites (PMCs)

Another category is based on shape of reinforcements. There are four types of composites based on shape of reinforcement.

1. Particulate reinforced composites

2. Short fiber or whisker reinforced composites
3. Continuous fiber or sheet reinforced composites
4. Laminate composite

Since metal matrix composites and metal matrix nano-composites are studied here, these terms are discussed more in this research.

1.1.1. Metal Matrix Composites (MMCs)

A metal matrix composite (MMC) is a composite material which has a metal as matrix. The other constituents could be a different metal or another material, such as a ceramic or organic compound. MMCs have lots of applications in different industries such as automotive, aerospace, sports, etc. In spite of the fact that MMCs are more expensive than the conventional materials, in some industries conventional materials are being replaced by MMCs. This is due to better properties and performance of MMCs compared to the conventional materials. As a result, the improvement in properties can justify the added cost. The applications of MMCs in different industries will certainly increase as manufacturing costs of these materials are reduced.

1.1.2. Metal Matrix nano-Composites (MMNCs)

Metal Matrix nano-Composite (MMNC) is one of the categories of MMCs. The size of one of the constituents of MMNCs is in the order of nanometer (10^{-9} m). This could be the particle size of reinforcements, particle size of matrices or grain size of matrices. MMNCs usually have better properties compared to the MMCs and they are very promising materials and suitable for a large number of applications. The nano-particles or nano-structures in MMNCs can improve the mechanical properties, thermal properties and wear resistance of the base material. Producing MMNCs is more challenging, and as a result they are likely to be more expensive. The main

challenge in producing these composites is distribution and deagglomeration of nano-reinforcements into the metal matrices and their boundary with the interface. In the liquid state processing of MMNCs, in addition to distribution of nano-particles in metal matrices, there is another important issue which is low wettability between matrices and reinforcements. This problem also exists in the processing of MMCs; however, since the surface area of nano-sized particles is much higher compare to micron-sized particles, this problem is more severe in MMNCs.

1.2. Processing of MMCs and MMNCs

Basically, in the processing of MMCs and MMNCs the main goal is distributing and probably deagglomeration of reinforcements into the matrices. To get the best possible properties in the MMCs and MMNCs the best and uniform distribution of reinforcements in the metal matrices is necessary.

There are different methods to produce MMCs and MMNCs. These methods are divided into three main categories including Vapor Deposition, Liquid State Processing and Solid State Processing. These methods are explained in more details in the next section.

1.2.1. Vapor deposition

The first method of producing MMCs and MMNCs is vapor deposition method. In this method usually the matrix alloy in vapor form deposits on reinforcements preform. This method is divided into two categories: Chemical Vapor Deposition (CVP) and Physical Vapor Deposition (PVD). The difference of these two methods is how the vapor of the matrix alloys is prepared.

The vapor deposition method has some advantages including:

- (a) The environment is very clean and there is an excellent control on amount of impurities
- (b) It has very good repeatability and reproducibility
- (c) There is a good control on the volume fraction of matrix and reinforcements through control of matrix coating thickness
- (d) There is a uniform distribution of fibers in the matrix alloy

However, this method is an expensive method and needs special equipment for processing of MMCs and MMNCs. In addition, there are some limitations on the shape and size of the components which produce with this method.

1.2.2. Liquid state processing

In the liquid state processing at least one of the constituents is in the state of liquid. Generally, metal matrix is in the liquid state and the reinforcement is in the solid state which is added to the molten metal. The liquid state processing has some advantages and disadvantages. This method is one of the cheapest method of producing MMCs and MMNCs which the main advantages. However, since the temperature during this method is very high, there are some undesirable reactions take place during processing. As a result, in this category of processing, it is difficult to control the final composition of the composites. In addition, it is difficult to distribute and deagglomerate the reinforcements in the matrices in this method compare to other methods. The liquid state processing can be divided in different methods including Stir Casting, Squeeze Casting, Pressure Infiltration, and Pressureless infiltration. Figure 1 schematically shows different types of liquid state processing method to synthesize MMCs and MMNCs. In stir casting processing reinforcements which are usually ceramic particles are added to the molten metal matrices. The reinforcements distribute and deagglomerate in the molten metal by using an

impeller or rotor. After suitable time of stirring by the impeller the composite materials pour in a mold to solidify. It is difficult to distribute the reinforcement especially nano-sized reinforcement into the molten metal by this method which is a disadvantage of this method. In addition, there is a limitation on amount of reinforcement which can be added to the matrix in this method; as a result, it is not a good method of producing MMCs with high volume fraction of reinforcement. Figure 1a schematically shows the stir casting method.

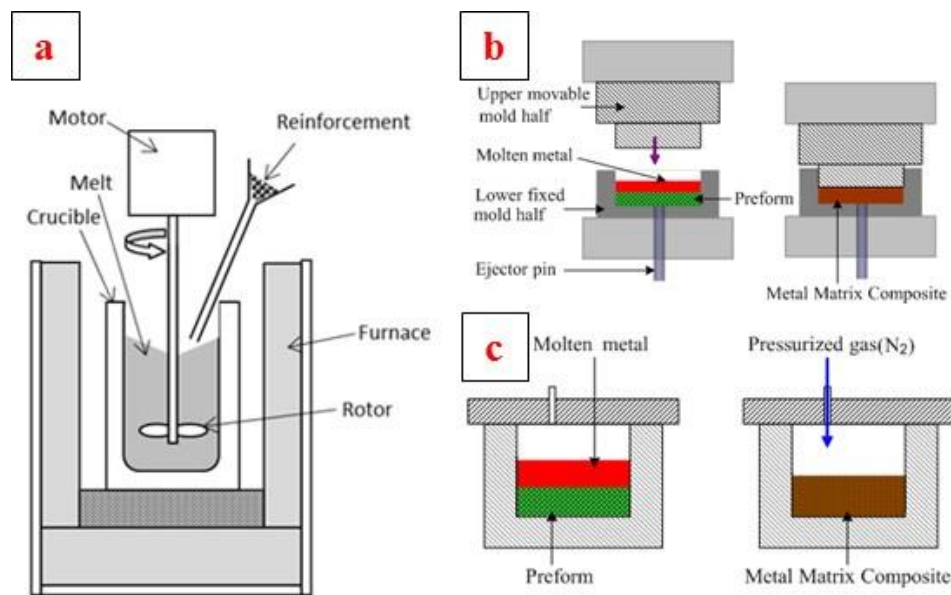


Figure 1. Schematic illustration to show different types of Liquid State Processing method; a) Stir Casting, b) Squeeze Casting, and c) Pressure Infiltration [1].

Squeeze casting is another liquid state processing method of producing MMCs and MMNCs. In this method, a preform of reinforcement which has porosities in it is produced from the reinforcement materials. Then, the molten metal matrix is poured above the preform as it shown in Figure 1b and filtrated into the preform by using a ram.

Another liquid state method of producing MMCs and MMNCs is pressure infiltration method. Figure 1c schematically shows the pressure infiltration method of producing MMCs. This method is very similar to the squeeze casting method. To infiltrate the molten metal into the

porous preform, an inert gas like argon or nitrogen is using to apply pressure instead of using a mechanical ram.

The last liquid state processing that is discussed here is pressureless infiltration method. In this method, the infiltration occurs spontaneously and there is no need of external applied pressure to infiltrate the molten metal matrix into the preform.

1.2.3. Solid state processing

The last but not the least category of producing MMCs and MMNCs is solid state processing. In this method, all of the constituents are in the state of solid. This method is also called powder metallurgy method. Basically, the temperature during this method is much lower compare to the liquid state processing; as a result, there is no undesirable chemical reaction happens in this method. This is the main advantage of this method. Also, there is a complete control on the final composition of the MMCs and MMNCs in this method. Moreover, the distribution and deagglomeration of the reinforcements occurs better in this method. This method is more suitable to produce MMNCs. However, this method is usually more expensive compare to the liquid state processing which is the disadvantage of this method. Also, it is difficult to produce very complicated shapes by solid state processing.

Generally, the solid state processing or powder metallurgy method has two steps which are milling and consolidation. These two steps are explaining in the next section. The main purpose of milling is to deagglomerate the reinforcement powder especially nano-sized powder. Milling also distributes the reinforcement powder into the matrix powder. Milling is very appropriate method to distribute and deagglomerate the powders during processing of MMCs and MMNCs

compare to other methods. There are three parameters in the milling process which are very important and control the energy of milling.

The first parameter is ball to powder weight ratio (BPR). As BPR increase the energy of the ball mill increases. However, by increasing the BPR the surface area of the balls increases as well; as a result, the probability of contamination of the powders by milling media like balls increases. Then, the optimum BPR is very important. The common BPR is from 10 to 20 in the literature.

Speed of the ball mill is the second parameter. By increasing the speed of the ball mill the energy of the milling increases. However, depends on the type of ball mill there is a limitation for the speed.

The third parameter of the milling is time of milling. It is very important to find out an optimum time of milling during powder metallurgy method to get the best results. The deagglomeration and distribution of the reinforcement powders into the metal matrices are not complete at short milling time. Long milling time can cause the contamination of the powders which can affect the final properties of the MMCs and MMNCs.

Four different types of milling including “Planetary ball mill”, “Attritor mill”, “Spex high energy ball mill” and “Cryomill” are using to produce MMCs and MMNCs. Figure 2 shows these four types of ball mills. Figure 2a shows a planetary ball mill. The vials and the supporting disc in this type of ball mill rotate in opposite directions. Based on this type of movement which is planet-like movement, it is called Planetary Ball Mill. Planetary ball mills use centrifugal acceleration field to mill the powders and materials. There exist two centrifugal fields in a planetary ball mill, one from the rotation of the vial and the other one from the rotation of the

supporting disc. The balls and materials inside vials have two relative motions including a rotary motion around the mill axis and a planetary motion around the vial axis [2]. There are two types of forces including impact and shear forces are applied on the powders during milling by planetary ball mill.

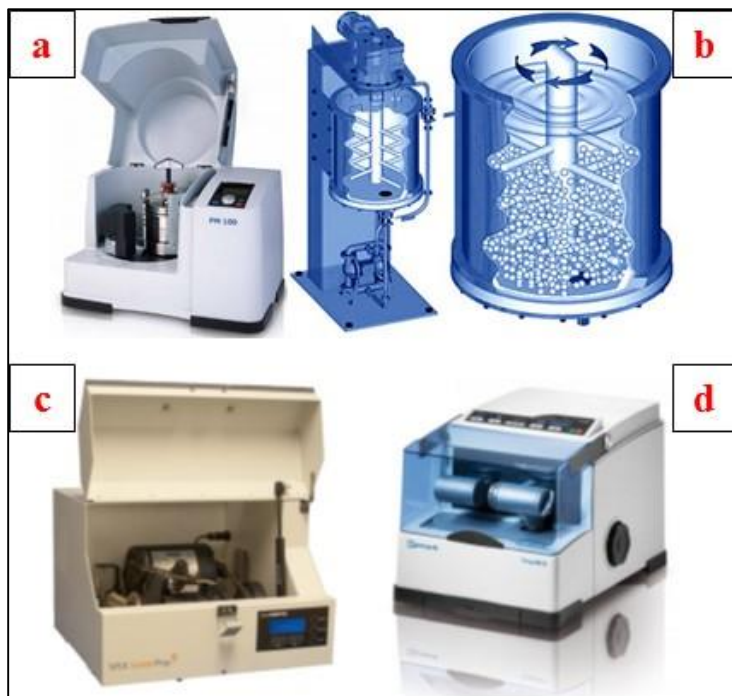


Figure 2. Different types of ball mill; a) planetary ball mill, b) attritor mill, c) Spex high energy ball mill, and d) cryomill [2].

The attritor was invented in 1922 by Szegvari in the USA for a quick dispersion of fine sulphur particles needed to complete the vulcanization of rubber. Attritor mill consist of a cylinder chamber with a shaft in the center which has multiple impellers sticking out from it (Figure 2b). The impellers apply different forces including impact and shear to charges inside of the container and causing reducing powder size and distribution of different powders. The dominant force in the attritor mill is shear force.

The Spex high energy ball mill has been developed in the USA under the trade name Spex mills (Figure 2c). The mill has one vial containing powders and milling balls, secured in the

clump. This vial energetically moves back and forth several thousand times a minute combined with lateral movements of the end of the vial. As a result, it moves like eight-shape or infinity sign-shape [2]. The energy of this type of ball mill is the highest one compare to other mills and the dominant force during milling is impact force.

The Cryomill is modified for milling in cryogenic temperature. The vial is cooled down with liquid nitrogen during milling and the temperature keeps constant and equal to -196°C . Figure 2 is shown a Cryomill made by Retsch Company. The movement of the vial in this mill is very similar to the Spex high energy ball mill.

1.2.3.1. Consolidating

After milling, composite powders are produced with a good distribution of reinforcements into the matrix. In the last step of producing MMCs and MMNCs by powder metallurgy method the loose composite powders should be consolidated by applying force on them. Generally, the consolidation process takes place at two steps including cold compaction and hot compaction.

1.2.3.1.1. Cold compaction

In the first step which is cold compaction, the consolidation occurs at about room temperature. There are two common methods to do cold compaction which are Cold Isostatic press (CIP) (Figure 3a) and single action cold compaction (Figure 3b). It is almost impossible to get highly consolidated sample by cold compaction. As we can see in Figure 3a, in the Cold Isostatic press (CIP) method, samples are immersed into a pressure tank filled with a liquid suspension. Subsequently the samples are hydraulically subjected to isostatic pressure. The isostatic pressure causes a uniform shrinkage of green bodies.

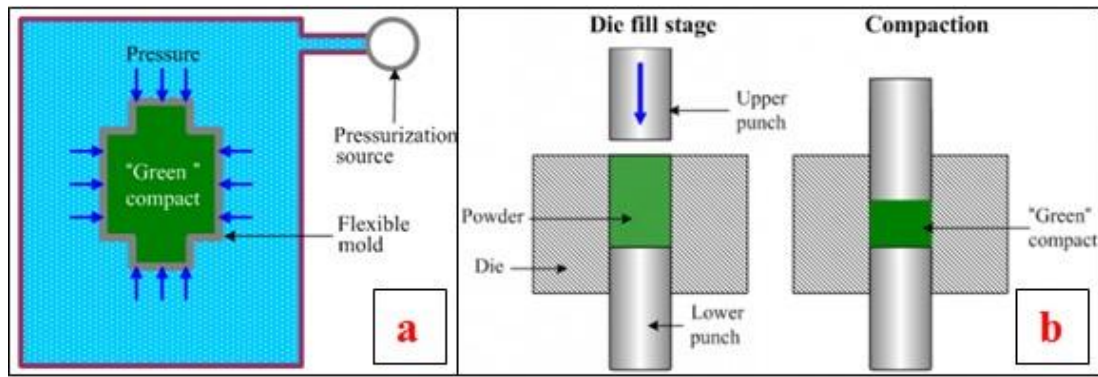


Figure 3. Cold compaction methods; a) Cold Isostatic Press (CIP), and b) Single action cold compaction [1].

The next cold compaction method is single action cold compaction (Figure 3b). In this method a given amount of powder is fed into the die cavity. Then, uniaxial pressure is applied to the powder in a die between two rigid punches. This method is less expensive compare to the CIP method and effectively used for mass production of simple parts. However, the relative density of the green body from single action compaction is lower than that of the CIP method. Also, since the pressure is applied from one direction in this method, there is a gradient in density of green bodies produced from the single action compaction method. This problem is much more dreadful in the longer green bodies. As a result, there is a limitation in the length of green body samples in this method.

1.2.3.1.2. Hot compaction

Then, after cold compaction it is necessary to do the next consolidation step at higher temperature. By applying high pressure or plastic deformation at high temperature the remaining porosities of the cold compacted samples will remove by diffusion, deformation and flowing of the powders at high temperature. After these two steps a highly dense sample will produce. Hot extrusion is a method of deformation of materials and metal powders. This process is using to create samples with a constant cross-sectional area. There are two different methods of extrusion including Direct Extrusion and Indirect Extrusion which schematically show in Figure 4a. The first advantage of this method is its ability to produce very complex cross-section samples. For

the last step of powder processing, extrusion can be used at high temperature. The deformation which occurs during extrusion of powders at high temperature causes to produce very highly dens samples.

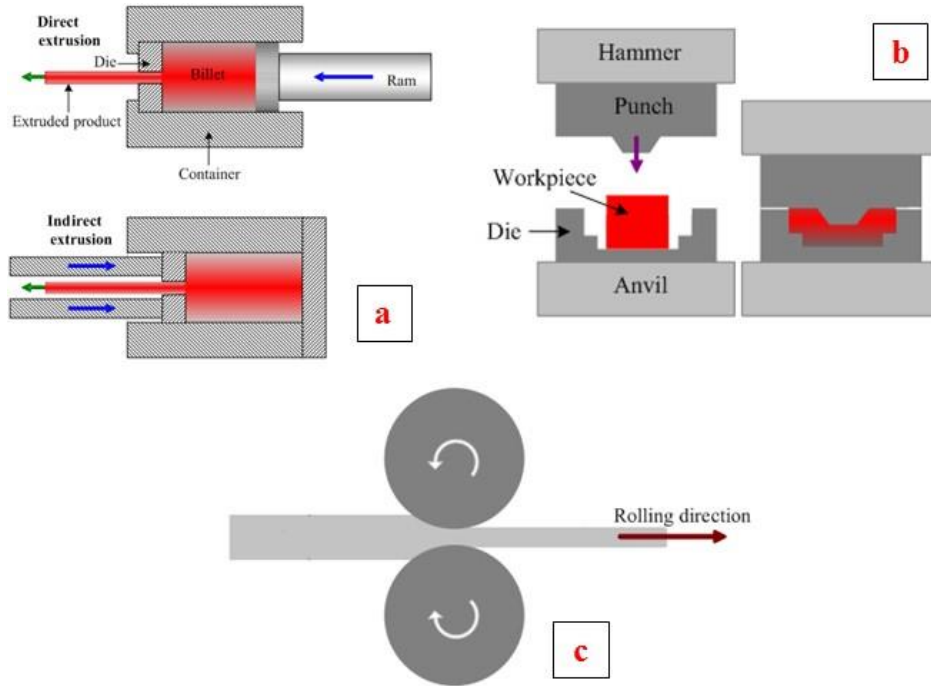


Figure 4. Schematic of hot consolidation processing; a) hot extrusion, b) hot forging, and c) hot rolling [1].

Hot forging is a compressive metal forming process, involving shaping a metal piece by hammer, press or rolls. Figure 4b schematically shows the forging process. In the hot forging the temperature of the sample is high during processing. This method is not very common method for consolidation of powders after cold compaction. The next deformation processing of metal powders is rolling. In this process, cold compacted sample is passed through one pairs of rolls to reduce the thickness and remove the remaining porosities of cold compacted samples. Figure 4c schematically shows the rolling process of materials. This process is using to produce sheet of materials. If the temperature of the sample is above its recrystallization temperature during rolling, then the process is called hot rolling. Hot Isostatic Press (HIP) process is one of the most

expensive methods of powder processing. The process of HIP is the same as CIP. Figure 3a schematically shows the CIP method which is the same as HIP. The only different in these two processes is the operating temperature. The final consolidated sample from HIP is usually denser compare to a CIPed sample. Figure 3b schematically shows the single action cold compaction process which is the same as single action hot compaction method. The mold is the same and pressure applies from one direction of the sample. The operating temperature during this process is higher than the recrystallization temperature of materials.

1.3 Strengthening mechanisms of MMCs and MMNCs

Different strengthening mechanisms are introduced for the MMCs and MMNCs. Three most important strengthening mechanisms in MMCs and MMNCs are Grain refinement strengthening, Orowan strengthening and coefficient of thermal expansion (CTE) mismatch strengthening which explain as follow:

1.3.1 Grain refinement strengthening

Grain refinement strengthening (Hall–Petch strengthening or Grain boundary strengthening) is one of the strengthening mechanism in MMCs and MMNCs. In this mechanism, changing the average grain (crystallite) size affect the mechanical properties of the materials. Basically, grain boundaries obstruct dislocation movement and cause changing in mechanical properties. Then, by decreasing the average grain size the obstacles for dislocation movement are increase; as a result, mechanical properties of materials like yield strength increase.

In 1951, Hall [3] showed that the length of slip bands or crack lengths correspond to grain sizes and there could be a relationship between these two. Hall has investigated

deformation of mild steel and concentrated on the yielding properties of that. In 1953, Petch [4] has published a paper concentrated more on brittle fracture of polycrystalline materials. He has measured the variation in cleavage strength with respect to ferritic grain size at very low temperatures and introduced a relationship exact to the Hall's equation. Then, the relationship between grain size and yield strength is named Hall-Petch equation after Hall and Petch. The Hall-Petch equation is as follow:

$$\sigma_y = \sigma_0 + \frac{K_{H-P}}{\sqrt{D}}$$

where σ_y is the yield stress, σ_0 is a materials constant for the starting stress for dislocation movement (or the resistance of the lattice to dislocation motion), k_{H-P} is the strengthening coefficient (a constant unique to each material), and D is the average grain diameter.

1.3.2. Orowan strengthening mechanism

The next strengthening mechanism is Orowan strengthening. This mechanism schematically shows in Figure 5.

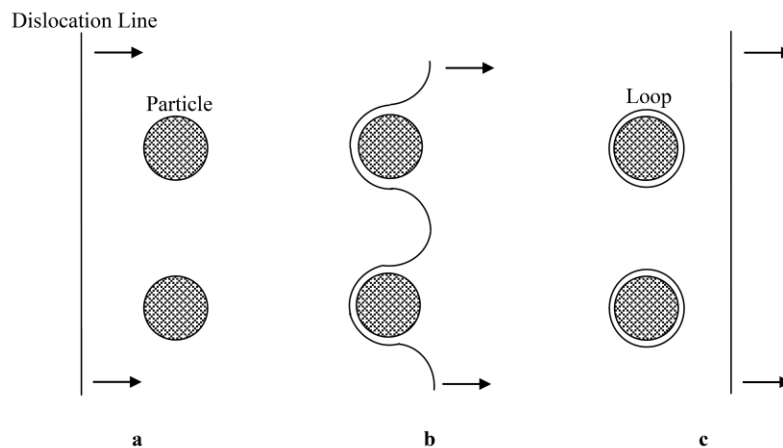


Figure 5. Orowan strengthening mechanism a) Dislocation moving toward particles, b) Dislocation passing the particles, and c) Formation of loops around particles.

In this mechanism dislocations reach the reinforcement particles in the MMNCs. Since the reinforcement particles are usually hard and non shearable, then the two segments of the dislocation line at either end of the particles attracts and finally a loop will form around the particle. After dislocations pass the particles, residual dislocation loops are left around each particle, increasing the material's strength. If the particles are assumed to be equiaxed, the strength increment ($\Delta\sigma$) is estimated as:

$$\Delta\sigma = \frac{2Gb}{L}$$

where

$$L = 0.6d\left(\frac{2\pi}{V}\right)^{\frac{1}{2}}$$

where G is shear modulus, L is the interparticle spacing, b is the Burger's vector, V is the volume fraction, and d is the grain diameter of the reinforcements [5].

1.3.3. Coefficient of Thermal Expansion (CTE) mismatch

Generally, there is a high temperature processing during synthesizing of MMCs and MMNCs. Coefficient of thermal expansion (CTE) of matrix and reinforcement in MMCs and MMNCs usually are not the same. As a result, during cooling from processing temperature to room temperature the difference of CTE of matrix and reinforcements cause plastic deformation around particles and reinforcements. Due to the plastic deformation, the dislocation density around particles and interface of matrix and reinforcements is high. This phenomenon has approved by TEM micrographs for different MMCs and MMNCs [6]. Generation of dislocations due to CTE mismatch causes the strengthening of MMCs and MMNCs. The dislocation density generated (ρ) is a function of reinforcement size (d), volume fraction (V), the product of the

thermal mismatch (ΔC), and the temperature change (ΔT). The strength (σ_d) can be estimated by the following relationship:

$$\sigma_d = \alpha G b \rho^{\frac{1}{2}}$$

where

$$\rho = \frac{12 \Delta C \Delta T V}{b d}$$

where G is the material's shear modulus, b is the Burger's vector and α is a constant between 0.5 and 1 [5].

Chapter 2.

Literature Review

2. Literature Review

2.1. Producing MMCs and MMNCs by powder metallurgy method

Powder metallurgy method is one of the popular methods of producing MMCs and MMNCs. Pure aluminum and aluminum alloys are one of the most widely used materials in MMCs and MMNCs as matrix from research and industrial viewpoints. This is due to their outstanding properties, such as light weight, high strength, high specific modulus, low thermal expansion coefficient, and good wear resistance [5]. For processing of aluminum matrix composites (AMCs) and aluminum matrix nano-composites (AMNCs), different types of milling including Planetary ball mill [7], attritor mill [5], Spex high energy ball mill [8] and cryomill [9] have been used by previous investigators. Each method has its own advantages and disadvantages. Different types of materials can be used as reinforcement in AMCs and AMNCs. The common reinforcement materials which have been used in aluminum matrices are Al_2O_3 [10], B_4C [11], SiC [12], AlN [13], CNTs [14] [15], etc. Recently, some researchers are using graphene as reinforcements for aluminum matrices [16] [17] [18] [19] [20]. In the previous studies powder metallurgy method was used to produce AMNCs.

2.2. Graphene

Graphene, one of the allotropes of elemental carbon, is a planar monolayer of carbon atoms arranged into a two-dimensional (2D) honeycomb lattice with a carbon–carbon bond length of 0.142 nm [21]. It has emerged as a new material in 21st century and received worldwide attention in nearly every field of science and engineering because of its exceptional optical, mechanical, charge transport and thermal properties. Properties of graphene are presented in Table 1. Recent researches have shown that graphene based materials can have a

significant influence on electronic and optoelectronic devices, chemical sensors, nanocomposites and energy storage [22].

Table 1. Physical and mechanical properties of Graphene.

Property	Unit	Data	Reference
Specific surface area	m^2g^{-1}	2630	[23]
Electron mobility	$\text{cm}^2\text{V}^{-1}\text{s}^{-1}$	1500	[24]
Electron resistivity	$\Omega.\text{cm}$	10^{-6}	[24]
Thermal conductivity	$\text{Wm}^{-1}\text{K}^{-1}$	5.3×10^3	[24]
Coefficient of thermal expansion	K^{-1}	-8×10^{-4}	[25]
Elastic modulus	TPa	0.5-1	[26]
Tensile strength	GPa	130	[26]

The most common method to produce graphene is exfoliation method. Writing with a graphite pencil is the first exfoliation method to produce graphene from graphite. However, by this method the thickness of graphene sheets is not controllable. Andre Geim's group in Manchester [27] produce a single layer of graphene to investigate its properties. They showed that by gently rubbing or pressing freshly cleaved graphite crystal on a silicon oxide wafer, a single atomic layer of graphene flake forms and visible under an optical microscope due to thin film interference effects [28]. However, this method is good to investigate the properties of graphene. For the case of using graphene in other researches like using graphene as reinforcement in metal matrices, this method of exfoliation is not applicable.

Recently, researchers exfoliate graphene with some new methods (chemically, mechanically or combination of these two) and use the exfoliated graphene as reinforcement in metals [18].

Mina Bastwros et. al. [18] have used a method called modified Brodie's method to exfoliate graphite and produce graphene oxide. In this method, they mixed 10 g of graphite, 160 ml of nitric acid, and 85 g of sodium chlorate at room temperature. The mixture was stirred for

24 hours. Then, they washed the slurry for four times with 5% hydrochloric acid and distilled water. By this method, they produce intercalated graphite through sedimentation. Then, they dry the solution at 60°C. Finally, the intercalated graphite was exfoliated to monolayer or few layers of graphene oxide by using ultrasonic power [18].

In another research by Ting He et. al. [29] they have used mechanical method to exfoliate graphite and produce alumina/ graphene composites. In this method, wet milling was used to mechanically exfoliate graphite. Pure alumina with an average particle size of 150 nm and natural graphite powder were mixed and milled in ethanol by planetary ball mill. The BPR and the rotation speed in the research were 30:1 and 250 rpm, respectively. Hot pressed in vacuum at 1100°C and 60 MPa has been used to consolidate the alumina/graphene composite [29].

Weifeng Zhao et. al. [30] have used a method which is a combination of chemical and mechanical method to exfoliate graphene. In this method, 0.02 g of graphite nanosheets with a thickness of 30-80 nm were dispersed in 80 ml of anhydrous N,Ndimethylformamide (DMF) solvent. Then, the slurry was milled for 30 hours by a planetary ball mill with the speed of 300 rpm. During milling the dominant force which applies to the nanosheets should be shear force to exfoliate graphite and produce graphene. Graphite layers have the weak van der Waals bonding and DMF-graphene has a strong bond. As a result, the shear force during milling can exfoliate graphite nanosheets into graphene. Then, the result slurry was centrifuged at 10000 rpm for 20 minutes to separate exfoliated graphene from unexfoliated and partially exfoliated graphite nanosheets. In the last step the DMF was evaporated from the supernatant under vacuum and the graphene powders were washed with ethanol [30].

Qianqian Li et. al. [31] have used a block copolymer Disperbyk-2150 (BYK Chemie GmbH) in ethanol to disperse Multi Walled Carbon NanoTubes (MWCNTs) for 15 minutes in an ultrasonic bath. The ratio of the block copolymer to MWCNTs was 1:1. Then, the solution was stirred for 30 minutes at 250 rpm [31].

These are the methods which are applicable to exfoliate graphene and used the exfoliated graphene as reinforcement in metal matrices.

2.3. Synthesizing Metal Matrix Composites reinforced by Graphene

As we mentioned earlier there are different methods to synthesize MMCs and MMNCs. To the knowledge of the author, only the liquid state processing and solid state processing have been used to synthesize MMNCs reinforced with graphene.

2.3.1. Liquid State Processing to synthesize MMNCs reinforced by Graphene

Chen et. al. [32] have synthesized magnesium matrix composite reinforced by graphene nanoplatelets by a combination of liquid state processing and solid state stirring. Their method schematically shown in Figure 6. The graphene nanoplatelets are added to the molten magnesium at 700°C by an automatic feeding system. The graphene nanoplatelets are dispersed in molten magnesium by ultrasonic processing for 15 minutes (Figure 6a). Then, the molten metal including dispersed graphene nanoplatelets was poured to a plate mold (Figure 6b). The microstructure of the samples after casting did not show a good dispersion of graphene nanoplatelets into the Mg matrix. To get better dispersion of graphene nanoplatelets into the composite plates, friction stir processing has been applied on the cast plates. The microstructure of the composite samples after friction stir processing showed a good dispersion of graphene nanoplatelets into the Mg matrix.

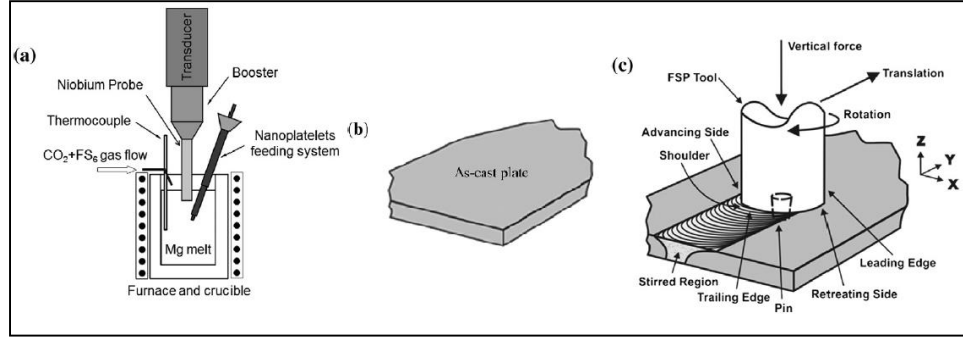


Figure 6. Schematic of the processing procedure to obtain graphene nanoplatelets reinforced metal matrix nanocomposites [32].

Fadavi Bostani et. al. [33] have produced Al alloy matrix composite reinforced by nano SiC and graphene nanosheets (GNSs) with the combination of solid and liquid state processing. The nano SiC and GNSs were milled by planetary ball mill in argon atmosphere at liquid nitrogen temperature. Then, pure aluminum was added to the milled powders and milling continued for 1.5 hours. The milled powders were added to A356 aluminum alloy at semi-solid temperature (605°C) and stirred for 5 min at 400rpm. During stirring, non-contact ultrasonic casting was also applied to the composite; then, poured into a preheated cast iron mold [33].

2.3.2. Solid State Processing to synthesize MMNCs reinforced by Graphene

Most of the metal matrix nanocomposites reinforced by graphene have been synthesized by solid state processing. There are two general steps in the solid state processing of MMNCs reinforced by graphene.

In the first step graphene is mixed, milled and dispersed into metal powders. Different types of milling at different atmospheres have been used to disperse graphene reinforcement into metal matrices.

Bartolucci et. al. [17] have thermally exfoliated graphite oxide to synthesize graphene nanoplatelets and used the graphene nanoplatelets as reinforcement into pure Al matrix. The Al

powder and graphene nanoplatelets were mixed by Acoustic mixer for 5 min and the mixed composite powders were milled by Attritor for 1 hr at argon atmosphere [17]. Wang et. al. [16] have synthesized MMNCs reinforced by graphene using flake powder metallurgy method. Graphite oxide (GO) was dispersed into deionized water to exfoliate graphene sheets. Flaky shape aluminum powder was produced by attritor mill and treated in 3wt% polyvinyl alcohol (PVA) aqueous solution to introduce a hydrophilic PVA membrane on the Al flakes. The GO aqueous solution was added drop by drop to the PVA Al flakes slurry to synthesize GO/Al composite powders. The GO/Al composite powders were heated to 550°C in the Argon atmosphere for 2 hours to reduce GO to graphene nanosheets and synthesize GNSs/Al composite powders [16]. Bastwros et. al. [18] have exfoliated graphene by modified Brodie's method and dispersed into aluminum alloy 6061 by SPEX high energy ball mill. The ball milling was conducted in ambient condition without using process control agent [18]. Rashad et. al. [19] dispersed graphene nanoplatelets (GNPs) with the average thickness of 5-15 nm into the acetone for 1 hr by ultrasonication. The slurry of GNPs in acetone and pure aluminum powder were mixed together by mechanical agitator for 1 hr to disperse GNPs into the aluminum matrix [19]. Rashad et. al. [34] have dispersed GNPs in ethanol by ultrasonication. Then, the solution was added drop wise into magnesium and aluminum solution in ethanol. Mechanical agitator was used to disperse the GNPs reinforcements into the metal matrix. The mixture was filtered and vacuum dried at 70°C [34]. Pérez-Bustamante et. al. [20] have synthesized GNP/Al composites by milling the powders in SPEX high energy ball mill at Argon atmosphere and using methanol as PCA. Shin et. al. [35] have produced Al matrix composite reinforced by few layered of graphene (FLG) using different types of milling. FLG was exfoliated by planetary ball mill in isopropyl alcohol atmosphere for 1 hour; then the exfoliated FLG was dried at 150°C for 3 hours.

Table 2. Summary of powder metallurgy method to synthesize MMNCs reinforced by graphene.

Matrix	Reinforcement	Types of milling	Atmosphere of milling	PCA	consolidation	Ref
Pure Al	Graphene (Thermal exfoliation of graphite oxide)	Acoustic mixer (5 min)+Attritor (1 hr)	Argon	Stearic Acid (2wt%)	HIP (375°C for 20 min)+Hot Extrusion 550°C	[17]
Pure Al	GO nanosheets dispersed into deionized water	Attritor to produce flaky shape Al+PVA aqueous solution+reduction of GO/Al at 550°C Ar for 2 hr to produce GNSs/Al	Polyvinyl alcohol (PVA)		Sintering in Ar at 580°C for 2hr+Hot extrusion 440°C	[16]
Al6061	Exfoliate Graphene synthesized by modified Brodie's method	SPEX 8000x	Ambient condition	-	Hot press at 100MPa for 10 min at 630°C (Mushy zone)	[18]
Pure Al	Graphene nanoplatelets (GNPs) (thickness 5-15 nm)	GNPs were ultrasonicated in acetone and added to the slurry of aluminum in acetone. Mixing by mechanical agitator for 1 hr	Acetone		Cold compaction (170 MPa)-sintering at 600°C for 6hr-hot extrusion at 470°C	[19]
Mg-Al	GNPs	GNPs were dispersed in ethanol by ultrasonication and were added drop wise into magnesium and aluminum solution in ethanol. Mechanical agitator was used to disperse the reinforcements into the metal matrix. The mixture was filtered and vacuum dried at 70°C	Ethanol		Cold compaction (600 MPa)-sintering at 630°C for 110 min in Argon-hot extrusion at 350°C	[34]
Pure Al	GNPs	SPEX high energy ball mill	Argon	Methanol	Cold compaction (950 MPa)-sintered under Argon atmosphere at 500°C	[20]
Pure Al	Few Layered Graphene (FLG)	FLG was exfoliated by planetary ball mill in isopropyl alcohol atmosphere then dried at 150°C for 3 hours. The exfoliated FLG was milled with aluminum powder by planetary ball mill for 3 hours in ambient atmosphere. The milled composite powders were milled again by attritor mill for 6 hours in purified argon atmosphere.		Stearic acid	Hot rolling at 500°C	[35]

The dried FLG was milled with aluminum powder by planetary ball mill for 3 hours in ambient atmosphere to disperse FLG into the aluminum matrix. The milled composite powders were milled again by attritor mill for 6 hours in purified argon atmosphere [35].

In the next step, the milled composite powders are consolidated to synthesize bulk samples for investigating their microstructures and properties. The consolidation processes which have been used to synthesize MMNCs reinforced by graphene include hot isostatic press (HIP) [17], hot extrusion [17] [16] [19] [34], hot press [18], cold compaction followed by sintering [20] and hot rolling [35]. These methods were conducted at varying time, temperature and atmosphere. Table 2 summarizes the powder metallurgy methods which have been used in the literature to synthesize MMNCs reinforced by graphene.

2.4. Characterization of MMNCs reinforced by Graphene

There are different methods such as optical microscopy, scanning electron microscopy, transmission electron microscopy, energy dispersive spectroscopy, and X-Ray diffraction, have been used to chemically and physically characterize microstructure of MMNCs.

Since the size of reinforcement in the MMNCs usually in the range of few nanometers, it is almost impossible to investigate the microstructure of these composites by optical microscope. However, optical microscope has been used to investigate the microstructure of MMNCs reinforced by graphene after extrusion [17]. Figure 7 shows the microstructure of pure Al and Al-0.1wt% graphene by optical microscope.

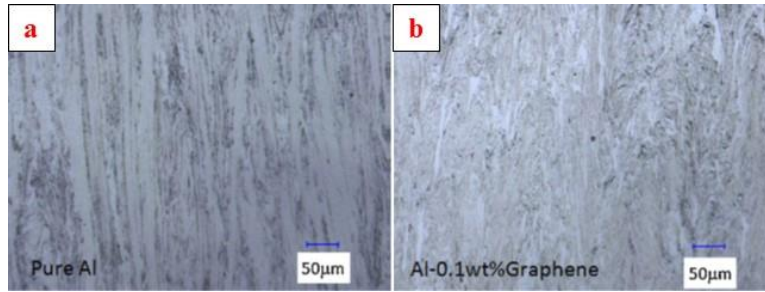


Figure 7. Optical micrographs of extruded pure Al and Al-0.1 wt% graphene [17].

Electron microscopy is a suitable method to investigate the microstructure of the MMNCs reinforced by graphene and shows the distribution of graphene in metal matrices. This method includes Scanning Electron Microscopy (SEM) and Transmission Electron Microscopy (TEM). In most of the literature, SEM and TEM have been used for characterization of these composites. Morphology and number of layers of graphene nanoplatelets and graphene oxide (GO) have been investigated by SEM [19] [34] [20] [35] and TEM [17] [16] [18].

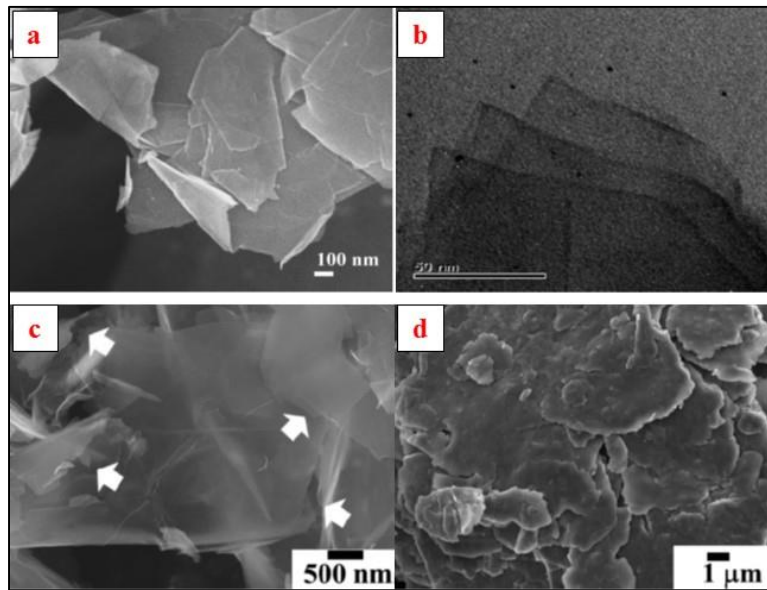


Figure 8. a) Secondary electron FESEM micrograph of the multilayered morphology of graphene nanoplatelets [20], b) TEM image of few-layers graphene [18], c) SEM image of few layered graphene (FLG) attached to Al powder using a planetary mill at 100 RPM (FLG is marked by an arrow) [35], d) SEM image of FLG embedded and dispersed in Al powder using an attrition mill at 500 RPM [35].

The morphology of graphene nanoplatelets are presented in Figure 8 by SEM and TEM. In addition, it is possible to investigate the distribution of graphene nanoplatelets in the metal matrices after powder processing by SEM. The morphology of composite powder after powder processing has been investigated by SEM [35] and TEM [33]. It has been showed that the graphene nanoplatelets attached to the aluminum powder after milling process. Figure 8c and d shows the morphology of FLG attached to the aluminum powder after milling. The graphene nanoplatelets showed by white arrows.

The distribution of graphene nanoplatelets into the metal matrices and agglomeration of graphene nanoplatelets can be investigated on the bulk samples by electron microscopy after consolidation processing.

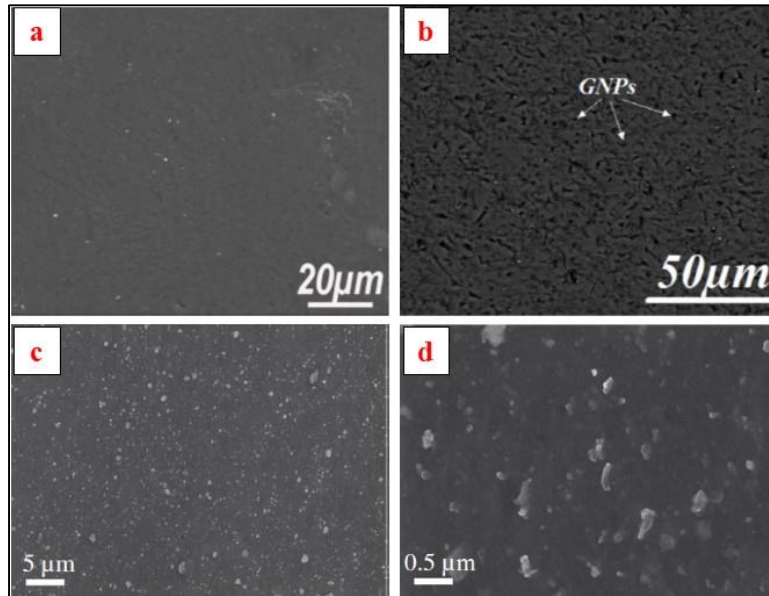


Figure 9. a) SEM surface image of Mg-1.5Al-0.18GNP [34], b) SEM image of Al/0.3wt%GNP composite [19], c) and d) SEM images of Mg matrix composites reinforced by GNP synthesized by ultrasonic processed + solid state stirred at different magnifications [32].

Microstructure of MMNCs reinforced by graphene has been investigated by SEM. Figure 9a and b show the microstructure of bulk samples of Mg-1.5Al-0.18GNP and Al/0.3wt% GNP

by SEM, respectively. These figures do not clearly show the distribution and agglomeration of GNP into the metal matrices. Figure 9c and d show the SEM image of the bulk sample of Mg matrix composites reinforced by GNP synthesized by ultrasonic processed + solid state stirred. The SEM images show the distribution of GNP into the Mg matrix [32].

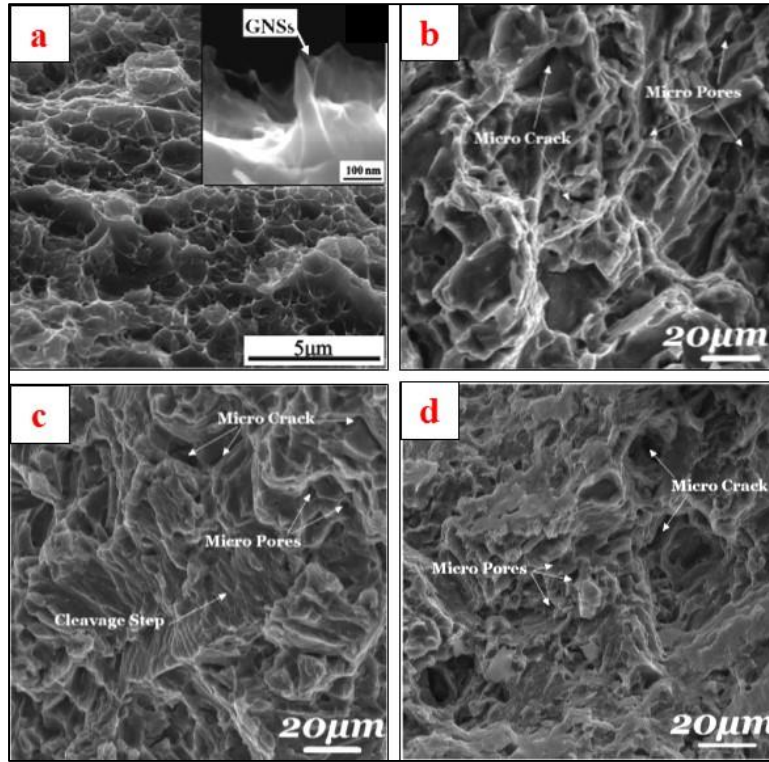


Figure 10. a) Fracture surface of 0.3 wt.% GNP/Al composite; the inset shows the GNS pulled out [16], b) Mg, c) Mg–0.5Al–0.18GNP, and d) Mg–1.5Al–0.18GNP composite [34].

In addition, the fracture surface of the MMNCs reinforced by graphene have been investigated by SEM [33] [16] [18] [19] [34] [20]. Investigating the fracture surface of MMNCs reinforced by graphene using SEM is a good method to show the location and distribution of graphene nanoplatelets in the metal matrices. Figure 10a shows the Fracture surface of 0.3 wt.% GNP/Al composite and also the GNS pulled out from the metal matrices [16]. Figure 10b, c, and d show the SEM images of fractured surfaces of Mg and Mg matrix composites reinforced by GNP. Micro pores, micro cracks and cleavage step are shown in the figures [34].

Transmission Electron Microscope (TEM) is another useful equipment to investigate the microstructure of bulk samples of MMNCs reinforced by GNPs. TEM have been used to show the microstructure of MMNCs reinforced by GNP, the interface between metal matrices and GNP, number of layers of graphene nanoplatelets in the MMNCs and distance between layers of graphene in MMNCs [32] [33] [20] [35].

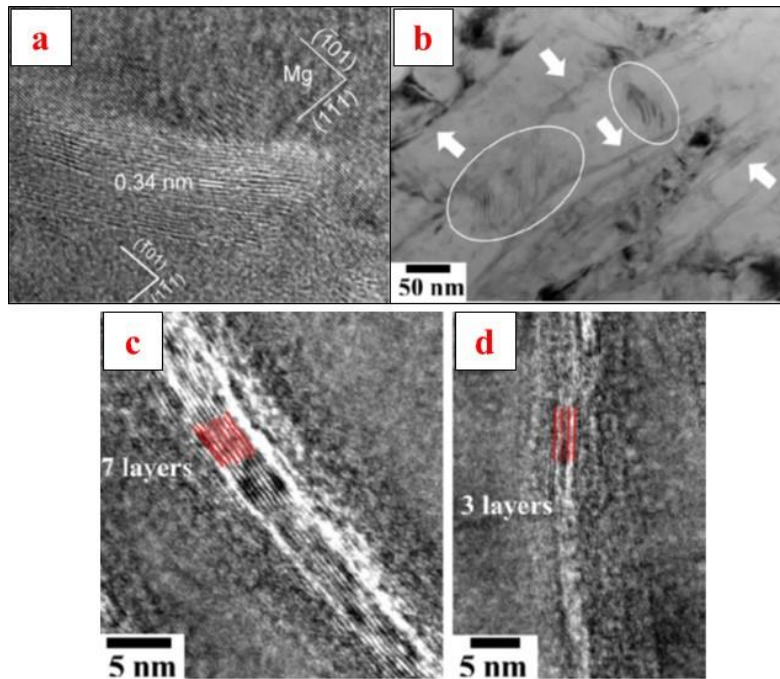


Figure 11. a) TEM image of hot-rolled Al/0.3 vol% composite. White arrows are graphene nanoplatelets and highly deformed regions are shown by circle [35], b) HRTEM image of the graphene nanoplatelet embedded in the magnesium matrix [32], c) and d) TEM image of hot-rolled Al/0.3 vol% composite. Number of layers of FLGs show by red lines [35].

Chen et. al. [32] have shown the microstructure of Mg-GNP by HRTEM in Figure 11a. They have shown the distance between the graphene layers which is 0.34 nm and different planes which are labeled in the Mg matrix. In addition, microstructure of hot-rolled Al/0.3 vol% composite has been showed in Figure 11b. The graphene nanoplatelets are shown by white arrows in the TEM microstructure. Highly deformed regions after deformation in the metal matrices shown by circles in Figure 11b. Number of layers of few layered graphene (FLGs) has also shown in Figure 11c and d [35].

Energy-dispersive X-ray spectroscopy (EDS, EDX, or XEDS), sometimes called energy dispersive X-ray analysis (EDXA) or energy dispersive X-ray microanalysis (EDXMA), is an elemental analysis to characterize the MMNCs samples. EDX have been used to characterize metal matrix composites reinforced by GNP [16] [19] [34]. Figure 12 shows the EDS results of a selected area in the Al matrix composite reinforced by GO. X-Ray map by EDS also has been used to show the elemental analysis of MMNCs reinforced by graphene [19] [34].

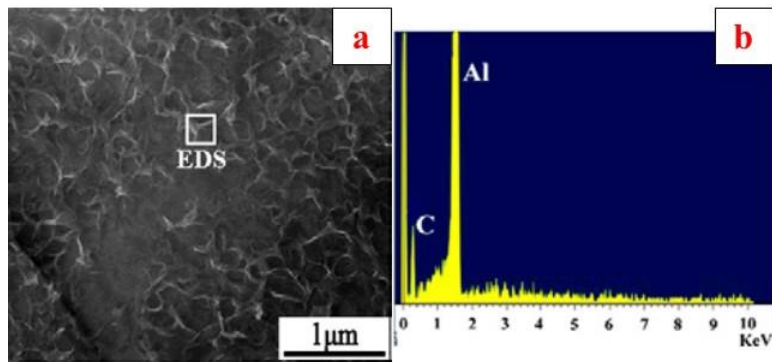


Figure 12. a) SEM image of an Al flake surface with adsorbed GO nanosheets; b) the EDS of selected area in (a) [16].

In the EDS, electron beams hit the sample and X-rays can be generated by each element in the sample which is sufficiently excited by the incoming beam. These X-rays are emitted in any direction in the sample and they may not escape from the sample. The energy of these X-rays depends on the amount of the element in the sample and the atomic number of the element. Based on the Moseley's law the square root of the frequencies of lines in atomic X-ray spectra depends linearly on the atomic number of the emitting atom. In addition, some elements have overlapping peaks in the EDS and it is difficult to distinguish these elements from each other. As a result, X-Ray mapping is not a good and accurate method to analyze samples elementally. Specifically, since the reinforcement in the MMNCs reinforced by GNP is an allotropes of carbon atom and carbon atom has a small atomic number ($Z = 6$), EDS is not a suitable characterization method to analyze these MMNCs reinforced by graphene.

The other characterization method for MMNCs is X-Ray Diffraction. X-Ray diffraction method is a nondestructive technique which gives us information about the crystal structure of materials, crystal size or grain size of metals matrices and chemical composition of materials. X-Ray diffraction method have been used to characterize metal matrix composites reinforced by graphene nanoplatelets [17] [18] [19] [34] [20]. Bartolucci et. al. [17] and Perez-Bustamante et.al. [20] have used X-Ray diffraction to show the formation of aluminum carbide (Al_4C_3) in the MMNCs during the processing. Figure 13a shows the formation of Al_4C_3 in the Al/GNP sample [17]. Rashad et. al. [19] [34] showed existence of GNPs in the metal matrices by X-Ray diffraction. Figure 13b shows XRD results of GNPs, pure Mg and Mg-xAl-0.18GNP composites.

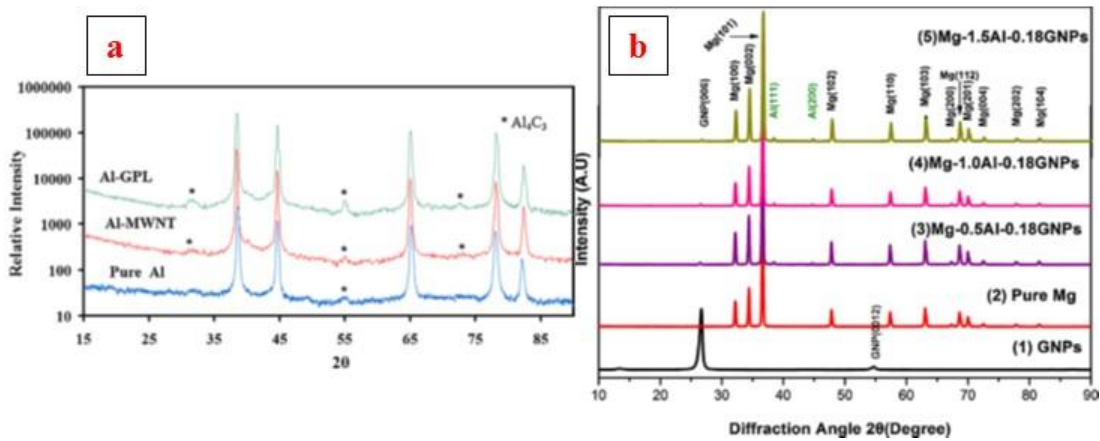


Figure 13. a) X-Ray diffraction of pure aluminum, Al-1.0wt% MWNT composite, and Al-0.1wt% graphene composite after extrusion [17], b) XRD of GNP, pure Mg and Mg-xAl-0.18GNP composites (x=0.5; 1.0; 1.5) [34].

Raman spectroscopy is another characterization method which have been used for graphene nanoplatelets [17] [34], graphene oxide [16] and MMNCs reinforced by GNPs [18] [20] [35]. Raman spectroscopy identifies materials based on molecular vibrations in the material. A monochromatic light source (i.e. laser) emit to the sample and the scattered light from the sample will detect based on change in energy of the light. The majority of the scattered light has the same frequency of the initial source. This light is called as Rayleigh or elastic scattering. Due

to the interactions between the vibrational energy of the molecules in the sample and the initial electromagnetic wave, a very small scattered light will be shifted in the energy level. The Raman spectroscopy result is showed by a graph of Raman intensity versus the wavenumber. A result of Raman spectroscopy of MMNCs reinforced by FLG is showed in Figure 14a. Graphene has three peaks which are called D-band, G-band and 2D-band in the Raman spectroscopy results Figure 14b shows the Raman spectroscopy results of single- and double layer graphene.

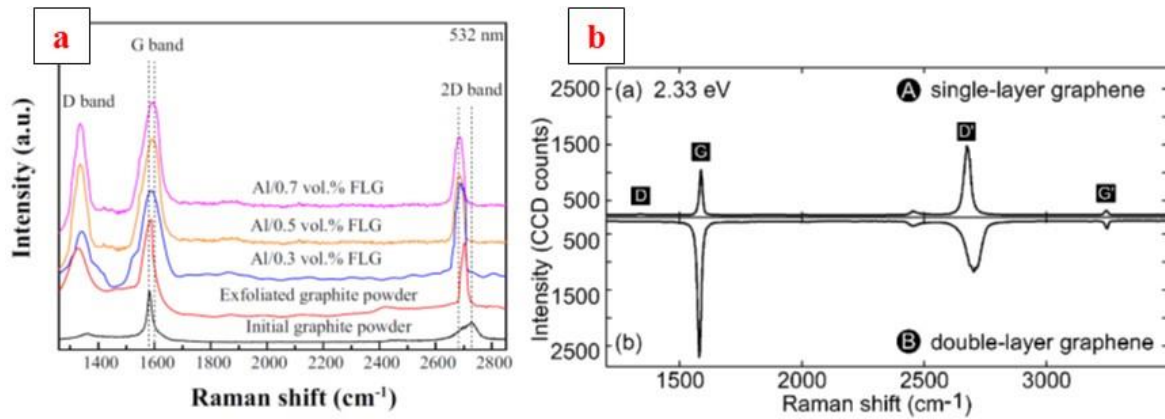


Figure 14. a) Raman spectrum of initial graphite powder, exfoliated graphite powder and hot-rolled Al/FLG composites [35], b) Raman spectra of single- and double-layer graphene [36].

2.5. Properties of MMNCs reinforced by Graphene

As mentioned earlier, graphene has special mechanical and electrical properties and because of these properties, researchers have been used graphene as reinforcement to improve the properties of composite materials. Polymers usually have low electrical conductivity and mechanical properties. By adding Graphene to polymer matrices, the mechanical and electrical properties of Polymer Matrix Composites (PMCs) improves significantly [37, 38]. Most of metals have a good electrical conductivity and improving the electrical properties of metals may be difficult by adding graphene. As a result, researchers usually do not investigate the electrical properties of MMNCs reinforced by graphene. However, mechanical properties of metals

especially light metals such as aluminum and magnesium are improvable. As a result, the main purpose of adding graphene to metal matrices is to improve mechanical properties of MMNCs and investigating the strengthening mechanisms. The mechanical properties of MMNCs reinforced by graphene has been summarized as follow.

2.5.1. Mechanical Properties and Strengthening Mechanisms

Mechanical properties of MMNCs reinforced by graphene have been investigated by hardness measurements [17], tensile test [16], compression test [19] and flexural stress [18]. In addition, a few theoretical works have been done on mechanical properties of MMNCs reinforced by graphene [35].

Figure 15 shows a summary of Vickers hardness measurements of MMNCs reinforced by graphene in the literature [32] [17] [19] [34] [20]. Figure 16 shows the strength of different MMNCs reinforced by graphene [17] [16] [19] [34]. In some studies the Vickers hardness of MMNCs increased with weight fraction of graphene added [17] [34]. Rashad et. al. [34] showed a significant increase in the Vickers hardness of Mg matrix composites reinforced by graphene nanoplatelets. The hardness of pure Mg with Mg matrix composites including 0.5-1.5 wt.% Al and 0.18wt.% GNP were compared. In the case of composites, the matrix is not pure Mg and it is Mg alloy. As a result, this comparison could be wrong and the increase in the hardness of these samples could be because of alloying element and solid solution strengthening [39] not because of graphene nanoplatelets. The same behavior has shown in the strength of these composites in the Figure 16. In some studies the Vickers hardness slightly decreased or increased by adding graphene nanoplatelets into the metal matrices [19] [20]. However, Bartolucci et. al. [17] showed that by adding graphene to the aluminum matrix, the strength of the composite significantly

decreased. This is explained in the context of enhanced aluminum carbide formation with the graphene filler.

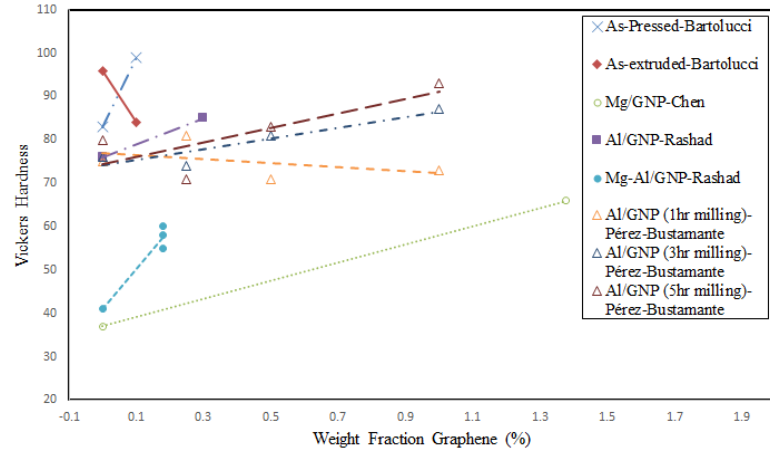


Figure 15. Hardness measurements of MMNCs reinforced by graphene [32] [17] [19] [34] [20].

Figure 16 shows the strength of different MMNCs reinforced by graphene. The results show that by adding graphene nanoplatelets to metal matrices the strength of the composites varies in different manner in different investigations. As a result, the understanding of mechanical behavior of MMNCs reinforced by graphene is not completely clear yet.

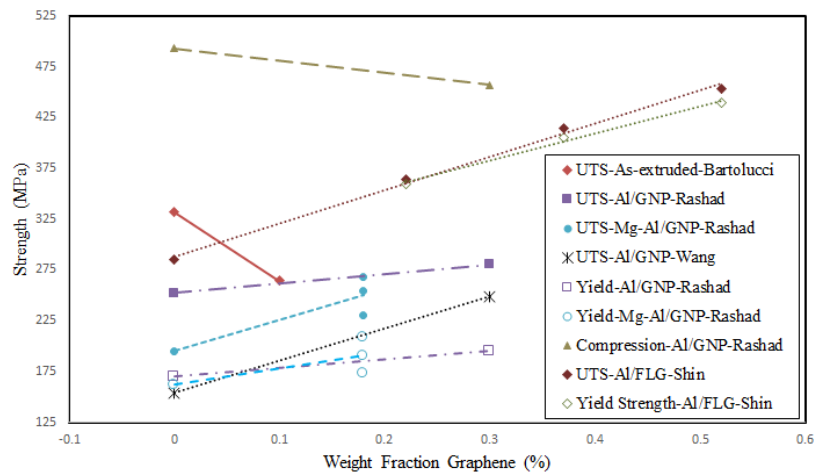


Figure 16. Yield, UTS and Compression strength of MMNCs reinforced by GNP [17] [16] [19] [34] [35].

Figure 17 shows the effect of milling time on flexural strength of Al6061/GNPs nanocomposites. The strength of the Al6061 and Al6061/1wt.%GNPs samples increased by milling time due to the strain hardening during milling. At low milling time (less than 30 min) the strength of the composite samples are almost equal to the strength of the matrix alloy because of inappropriate dispersion and agglomeration of GNPs in the alloy matrix. After 60 minutes of milling, the strength of Al6061/1wt.%GNPs samples considerably increased compare to the Al6061 samples with the same milling time. This is because of good distribution of GNPs in the matrix alloy [18].

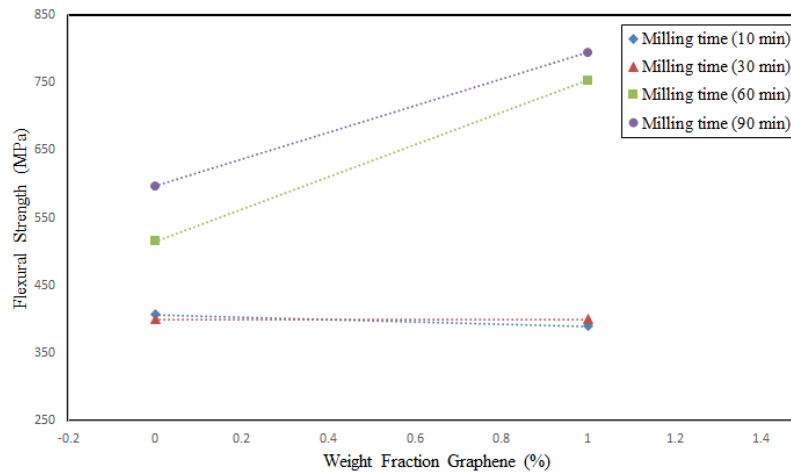


Figure 17. Effect of milling time on Flexural Strength of aluminum matrix composites reinforced by GNPs [18].

Fracture strength of a perfect single layer of graphene is about 125 GPa [26]. Wang et. al. [16] have been used the rule of mixture to estimate the mechanical properties of aluminum matrix composites reinforced by Graphene. By adding 0.3wt.% (about 0.5vol.%) of GNSs to the aluminum matrix, the improvement in tensile strength of the composite should be around 500 MPa. However, this improvement has not been reached in the literature and there are some reasons for that. First of all, it assumes that all of the graphene nanoplatelets are single layer of graphene which are homogenously distributed in the metal matrices. However, in the real world,

the graphene reinforcements in the metal matrices are not single layer. As a result, the fracture strength of multi layers of graphene is not 125 GPa. Secondly, the strength of GNPs in different directions are not the same. The in-plane strength of GNPs is much higher compared to the out-of-plane strength of GNPs. Graphene nanoplatelets are randomly distributed in all directions in the metal matrices. As a result, the out-of-plane GNPs in the metal matrices cannot act as an in-plane GNPs. Moreover, the distribution of GNPs in the metal matrices and bonding between the GNPs and metal matrices has a significant effect on the mechanical properties of these MMNCs. However, the homogenous distribution of GNPs and a perfect bonding between GNPs and metal matrices are not practically achievable. Because of these reasons, the theoretical strength of these MMNCs have not been reached.

There are well-known strengthening mechanisms for metal matrix nanocomposites. These mechanisms are including grain refinement, Orowan looping, solid solution strengthening, precipitation strengthening, load bearing, Coefficient of Thermal Expansion (CTE) mismatch and modulus mismatch strengthening [39]. Different explanation and strengthening mechanisms have been used in the literature to explain the mechanical behavior of MMNCs reinforced by graphene.

During the powder processing of the MMNCs reinforced by GNPs, plastic deformation and strain hardening due to the ball milling (Figure 17) occurs. As a result of the processing method, the grain size of the metal matrices decreased. Due to the smaller grain size, grain refinement strengthening which shows by Hall-Petch equation [16] [18] [35] [39] is one of the main strengthening mechanisms in the MMNCs reinforced by GNPs.

In addition, because of the strain hardening, dislocation density increased in the composite samples. Increasing the dislocation densities in the sample also causes strengthening of the MMNCs reinforced by GNPs [32] [19] [34]. Moreover, CTE mismatch between the metal matrices and GNPs can cause to increase the dislocation density and increasing the strength of the composite samples. However, the existence of the CTE mismatch strengthening in MMNCs with very small size reinforcements is in doubt [40] [41]. Since the size of the GNPs in one direction is very small, it could be possible that the CTE mismatch does not applicable to MMNCs reinforced by GNPs. It has been shown that the thickness of flaky shape metal matrices are thousand times larger than the GNPs thickness and a very small portion of the metal matrices was affected by the GNPs. In this study, the same grain size and amount of dislocation density was reported for Al/GNPs and unreinforced Al samples. These results suggest that there is no CTE mismatch strengthening in this MMNCs reinforced by GNPs [16]. As a result, the CTE mismatch strengthening in the MMNCs reinforced by GNPs depends on the size and geometry of the metal matrices and reinforcements.

The other possible strengthening mechanism for MMNCs reinforced by GNPs is Orowan looping. Rashad et. al. [19] [34] have claimed that one of the strengthening mechanism in the MMNCs reinforced by GNPs is Orowan looping. The Orowan mechanism requires that unshearable particles be located within the grains. As a result, the size of grains and reinforcements are very important to get the Orowan strengthening in the MMNCs. Graphene is a two dimensional material. In one dimension, the size of graphene is in the order of micron. Since the size of GNPs in one dimension is bigger than the size of grains in the metal matrix, it is almost impossible to get the Orowan strengthening in these MMNCs.

Since GNPs is a two dimensional material, load bearing or load transfer strengthening mechanism could be one of the main strengthening mechanism in MMNCs reinforced by GNPs [32] [16] [19] [34] [35]. The load which is applied to the MMNCs may transfer to the reinforcements from the metal matrices through shear stresses along the interface between matrix and reinforcements. The interfacial area (S) and reinforcement's cross-sectional area (A) play an important role in the load transfer strengthening mechanism. There are different models to show the mechanical properties of MMCs. These models are presented in Table 3 and Figure 18.

Table 3. Different theoretical models for prediction of MMCs strength.

Model	Equation	Reference
Short fiber	$\sigma_c = \sigma_f V_f \left(\frac{l}{2l_c} \right) + \sigma_m (1 - V_f)$ ¹	[42]
Developed Shear-lag	$\sigma_c = \frac{V_f \sigma_m}{2d}$	[43]
Developed Halpin-Tsai	$\sigma_c = \frac{1+\xi\eta V_f}{1-\eta V_f} \sigma_m$ ²	[44]
Piggott	$\sigma_c = \frac{\sigma_m \frac{2L}{t} V_p}{4} + V_m \sigma_m$ ³	[45]
Shin	$\sigma_c = V_r \left(\frac{S}{A} \right) \left(\frac{\tau_m}{2} \right) + \sigma_m V_m$ ⁴	[35]
¹ $l < l_c$ ² To consider dispersion of the reinforcement $(2(l/d)e^{(-40V_f-1.0)})$, the value of ζ has to be optimized. η depends on (σ_f/σ_m) . ³ V_p and L are the volume fraction and the long axis of the platelet, respectively. ⁴ S and A are the interfacial area and fiber cross-sectional area, respectively.		

Figure 18 shows the prediction of yield strength of composite materials based on different models as a function of graphene volume fraction. In addition, it presents the experimental results of aluminum/GNPs samples.

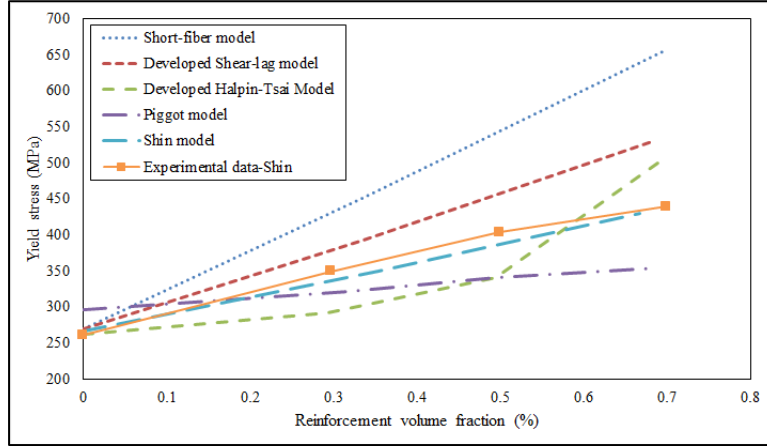


Figure 18. Theoretical prediction of yield strength of composite materials based on different models and an experimental result [35] [42] [43] [44] [45].

The short fiber and shear-lag model are based on the strengthening by general discontinues fiber. In the modified shear-lag model [43], the orientation of the fibers is considered. The Halpin-Tsai model considers the rule of mixtures for discontinuous reinforcement and gives a semi-empirical description of short-fiber reinforced composites [44]. The Piggott model modifies the discontinuous fiber model and is specified for two dimensional reinforcements like GNPs [45]. The Shin model considers the interface between matrix and reinforcement with a new term (S/A) [35]. The results show that the model which developed by Shin et. al. [35] has a good fit with their models.

In some cases, formation of aluminum carbide (Al_4C_3) has been reported during processing of MMNCs reinforced by GNPs [17] [16] [18]. Formation of aluminum carbide has negative effect on mechanical properties of the aluminum matrix nanocomposites. One of the reasons that the strength of aluminum matrix nanocomposites reinforced by GNPs is lower than the theoretical strength is because of formation of aluminum carbide [17] [16]. However, Bastwros et. al. [18] claimed that formation of aluminum carbide during the processing of aluminum

matrix nanocomposites reinforced by GNPs is one of the strengthening mechanism in the composites.

2.5.2. Tribological Properties

The tribological properties of MMNCs reinforced by GNPs is expected to be improved. A few studies have been published to investigate the tribological properties of these composites. Recent investigations have shown that graphene reinforced metal matrix nanocomposites can act as a self-lubricating material [46] [47] [48]. Al/graphene nanocomposites at different weight percentage (0.5, 3 and 5 wt.%) have synthesized by using powder metallurgy technique. The effect of weight percentage of graphene on tribological properties of self-lubricating nanocomposites was studied. The self-lubricating composite reinforced by 3 wt. % graphene has shown the best tribological properties under dry wear test conditions. In addition, It has been reported that the wear regime has been changed from sever wear regime to mild wear regime by adding graphene to the metal matrices [47]. Moreover, copper matrix composites reinforced by micron- and nano-size graphite have synthesized by powder metallurgy method. The tribological properties of these composites have been investigated. The wear resistance of the copper matrix composites reinforced by nano graphite has been improved compare to copper and copper reinforced by micron graphite [46].

2.6. Cryomilling

As explained earlier, there are different types of milling like planetary ball mill, attritor mill, Spex high energy ball mill and cryomill. Each one of these milling has different mechanisms and energies. As a result, the result grain size from each mills are different. Recently, cryomill is one of the most common methods of producing high strength materials and composites.

The cryomilling technique was developed at Exxon Research and Engineering Company for the first time [49]. They have used cryomill for an yttriated iron alloy and showed that mechanical alloying of this alloy at cryogenic temperature allowed them to produce the finest particle sizes and grain sizes in a shorter time compare to the mechanical alloying of the same alloy at room temperature in air or Ar atmosphere [49].

In 1989 cryomilling was used to produce aluminum matrix composite reinforced by Al_2O_3 for the first time [50]. The purpose of the research was to develop dispersion strengthened composites. The cryomilling equipment which is used to produce the composite shows in Figure 19. The cryomilling apparatus is a 10 l Szegvari attritor mill that is modified to allow continuous flow of liquid nitrogen into the mill. After the milling process the powder collect for the next processing steps. The next processing step is degassing to remove volatile contaminations including water vapor or residual PCA. In the degassing step powders pour into an Al can with a hollow stems and valves for hot vacuum degassing. Then, the can is sealed at the stem preserve the vacuum. The degassed powder is consolidated usually into two steps. The primary consolidation step is usually HIPing or CIPing. The last consolidation process is hot extrusion [51]. This processing method is using by different researchers to produce bimodal materials and MMNCs [52] [53] [54] [55] [56].

During the milling processing nanostructured materials produced. A basic description of the development of nanostructured materials by mechanical milling was introduced by Fecht [57]. Based on this description there are three steps occur during mechanical milling. In the first step grain refinement happens by localized deformation and producing high dislocation density. Next, annihilation and recombination of dislocations takes place and nanometer sub-grains form. Then,

in the last step the sub-grain boundaries transform to randomly oriented high angle grain boundaries [57].

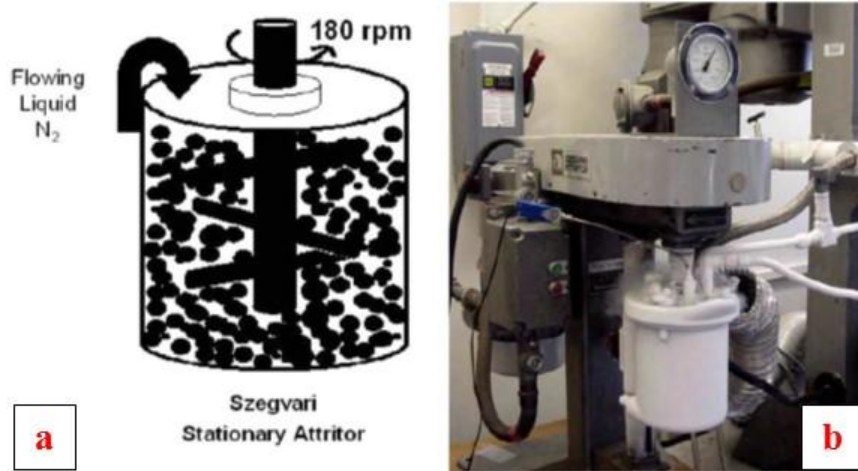


Figure 19. a) Schematic design of a typical cryomilling attritor mill and b) the cryomilling attritor mill which used for producing Al-Al₂O₃ [51].

Figure 20 schematically shows the three steps of grain refinement during milling.

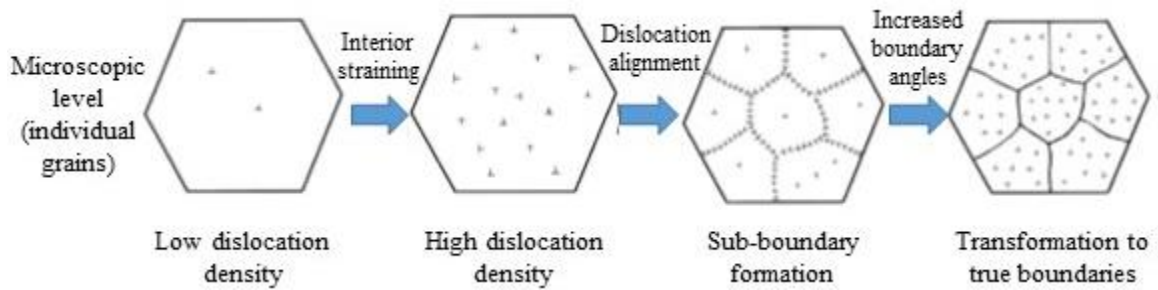


Figure 20. Schematic representation of grain refinement mechanism during ball milling in microscopic level for an individual grain [58].

Figure 21 shows the grain size of different materials after cryomilling or ball milling versus milling time. The results show that by crymilling in a shorter time the grain size of materials reaches to below 40nm. As a result, recently, researchers are using cryomilling to produce MMNCs and bimodal nanostructure materials [58] [59] [60].

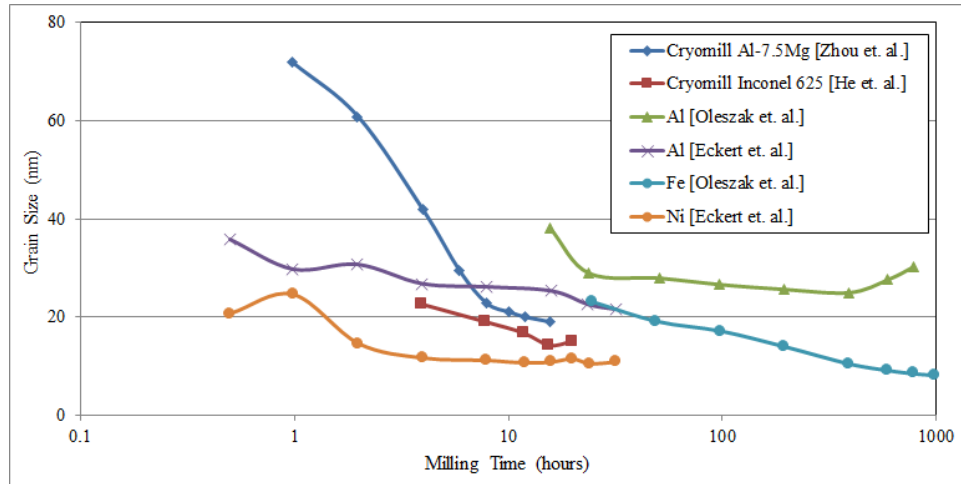


Figure 21. Grain size as a function of milling time for cryomilled and ball milled powders [59] [60] [61] [62].

The tensile properties of MMNCs and bimodal nanostructure materials have investigated by tensile test [52]. The tensile results present in Figure 22. The results show that the tensile strength of Al5083 increased by applying cryomill on the powders.

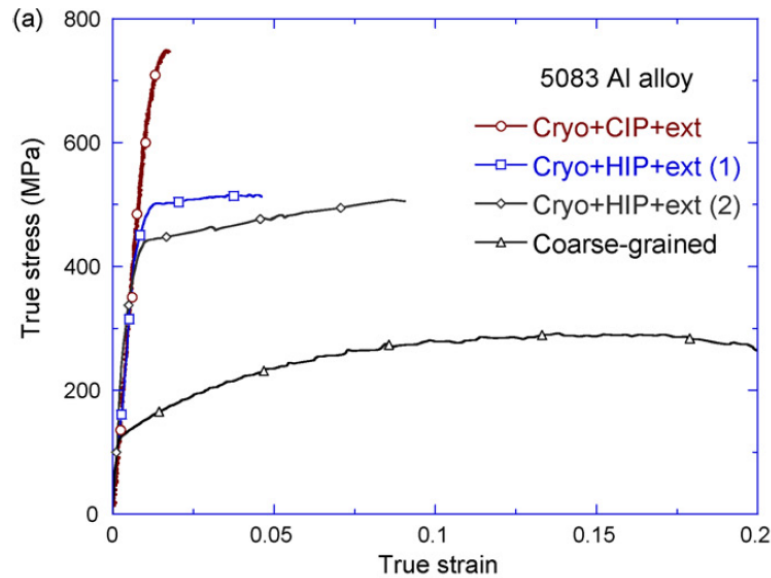


Figure 22. True tensile stress as a function of true strain of cryomilled 5083 Al alloys consolidated with different consolidation methods including CIP + ext, HIP + ext1 [52].

The dominant strengthening mechanism for the samples in Figure 22 is grain refining strengthening. However, after cryomilling the ductility of the samples significantly decreases

compare to the un-cryomilled sample. The consolidation process also has a significant effect on the tensile properties of the samples. The tensile strength of sample consolidated by CIP and extrusion is much higher compare to the samples consolidated by HIP and extrusion. Since the temperature during HIPing is very high, grain growth occurs during HIPing. As a result, the average grain size of samples after HIPing is bigger compare to that of after CIPing. Then, the tensile strength decreases based on the Hall-Petch equation.

2.7. Predicting Mechanical Properties of MMCs and MMNCs

There are different methods in the literature to predict properties of MMNCs. The basic model to predict the properties of MMNCs is the rule of mixture. The rule of mixture is as follow:

$$P_c = (V_m \times P_m) + (V_f \times P_f)$$

where P_c , P_m and P_f are the property of composite, matrix and filler (reinforcement) respectively. V_m and V_f are the volume fraction of matrix and filler (reinforcement) respectively. However, this basic equation is not very applicable for all of the composites. There are some other methods which are the modification of the rule of mixture to predict the properties of composites in a better way. In the following, different equations which are using to predict different properties of composites are discussed.

2.7.1. *Young's Modulus*

The young's modulus is a direct measure of microscopic interatomic resistance to stretching. Based on the interatomic bonding, different materials have different young's modulus. Various theoretical models in the literature exist to predict the modulus of the composites as a function of matrix, filler and interface properties. These models are including

Iso-stress model, Iso-strain model, Mori-Tanaka model and Halpin-Tsai model to predict young's modulus of the composites [61]. Halpin-Tsai model can be used for MMCs reinforced by graphene.

$$E_c = E_m \left(\frac{1 + \xi \eta V_f}{1 - \eta V_f} \right)$$

where

$$\eta = \frac{\frac{E_f}{E_m} - 1}{\frac{E_f}{E_m} + \xi}$$

where E_m , E_f and E_c are the elastic modulus of the matrix, filler and composite, respectively, and V_f is the filler volume fraction. The Halpin-Tsai equation is very useful method to predict the young's modulus of composites reinforced by short fiber and particles. ξ is a shape factor which is equal to $2w/t$ where w is filler length and t is filler thickness.

The Halpin-Tsai equation is modified to use for graphene reinforced composites by Koratkar [61]. The modified equation is as follow:

$$E_c = \frac{3}{8} E_M \frac{1 + \xi \eta_L V_{eff\ fib}}{1 - \eta_L V_{eff\ fib}} + \frac{5}{8} E_M \frac{1 + \eta_W V_{eff\ fib}}{1 - \eta_W V_{eff\ fib}}$$

where

$$\eta_L = \frac{(E_{eff\ fib}/E_M) - 1}{(E_{eff\ fib}/E_M) + \xi}$$

and

$$\eta_W = \frac{(E_{eff\ fib}/E_M) - 1}{(E_{eff\ fib}/E_M) + 2}$$

where E_c is the young's modulus of the nanocomposite, $V_{eff\ fib}$ is effective filler volume fraction; $E_{eff\ fib}$ and E_M are the effective filler and matrix moduli. $E_{eff\ fib}$ can be assumed to be similar to the

graphene nanoplatelets modulus (1.01 TPa). The parameter ζ is the geometry factor of effective filler which is as follow based on Halpin-Thomas:

$$\xi = 2 \left(\frac{(W + L)/2}{t} \right)$$

where L, W and t are the average length, width and thickness of the graphene nanoplatelets. The size of the graphene that we have used is 5 μm in diameter and 6 nm in thickness. Then, we assume that W and L for the graphene nanoplatelets are 5 μm and t is 6 nm. The ζ is equal to 1666.67 based on the above equation and assumptions. By using the Halpin-Tsai equation which explained earlier and assuming $E_{\text{eff fib}}=1010$ GPa and $E_M=69$ GPa, the young's modulus of aluminum matrix composites reinforced by 0.1wt% (=0.123Vol%) graphene nanoplatelets is equal to 160.44 GPa. This predicts about 130% improves in the young's modulus of aluminum by adding 0.1wt% graphene nanoplatelets.

Ferguson et. al. [62] modified the rule of mixture to calculate the young's modulus of MMCs reinforced by particles with different degree of bonding of matrix and reinforcements. The following equation shows their modified rule of mixture to calculate young's modulus:

$$Y_c = Y_m + (Y_r - Y_m)f_r F_{\text{sphere}} \left(F_{f_r} + F_{\Delta v} - F_{\text{bond}_Y-SA} F_{\text{bond}_Y\text{-concentration}} \right) \text{ with } F_{\Delta v} \cong 0$$

where

$$F_{f_r} = 1 + 2f_r$$

and

$$F_{\text{bond}_Y-SA} = \frac{1}{6}(1 - f_{\text{Bond}})$$

and

$$F_{\text{bond}_Y\text{-concentration}} = 1 + 4\pi(1 - f_{\text{Bond}})$$

where Y_c , Y_r and Y_m are young's modulus of composite, reinforcement and matrix, respectively. f_r is particle volume fraction, F_{sphere} is shape factor of reinforcement, F_{fr} second-order effects of reinforcement concentration, $F_{\Delta\nu}$ the Poisson's ratio effect, $F_{\text{bond Y-SA}}$ degree of bonding for surface area effect and $F_{\text{bond-Y-concentration}}$ degree of bonding for concentration effect. $F_{\text{sphere}}=1/3$ for the spherical particles [62].

Figure 23 shows the estimate of Young's Modulus of aluminum matrix composites reinforced by different volume fraction of alumina particles at different degrees of matrix-reinforcement bonding from $f_{\text{Bond}} = 0$ which is not bonded to $f_{\text{Bond}} = 1$ which is perfectly bonded. To calculate the Young's Modulus from the above equation the Young's Modulus of pure aluminum is $Y_m = 69$ GPa and the Young's Modulus of alumina is $Y_r = 408.99$ [63]. The percentage of change in Young's Modulus of the composites versus particle volume fraction presents in Figure 24.

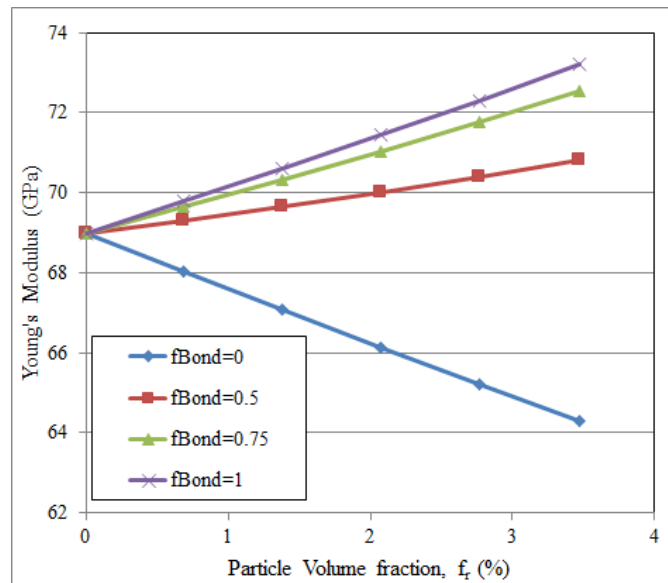


Figure 23. Prediction of young's Modulus of composites versus particles volume fraction at different degrees of bonding.

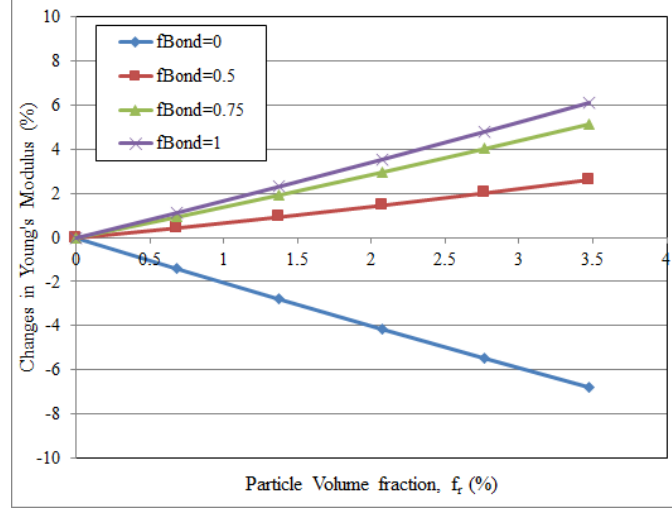


Figure 24. Percentage of change in Young's Modulus of the compsoites versus particle volume fraction.

2.7.2. Yield strength

As explained earlier, there are different strengthening mechanisms in the MMCs and MMNCs. All of these mechanisms can contribute in the MMCs and MMNCs. However, this contribution is not a simple arithmetic equation [64]. Ferguson et. al. [64] have proposed an analytical yield strength prediction model combining arithmetic and quadratic addition approaches. Their prediction model is based on the consideration of two types of yielding mechanisms; stress-activated and energy-activated. In their model the well-known mechanisms including grain refinement, Orowan looping, solid solution strengthening, precipitation strengthening, CTE mismatch and modulus mismatch strengthening are considered. The proposed superposition model is as follow [64]:

$$\sigma_y = \sigma_{el\,solvent} + \Delta\sigma_{el\,solute} + \Delta\sigma_{el\,ppt-coh} + \Delta\sigma_{el\,lsf} + \sqrt{\Delta\sigma_{HP}^2 + \Delta\sigma_{Oro}^2}$$

where σ_y is the yield strength of dispersion strengthened alloys or MMNCs, $\sigma_{el\,solvent}$ is yield strength of solvent (i.e., matrix materials) without alloying elements or precipitates or reinforcements, $\Delta\sigma_{el\,solute}$ is an increase in yield strength due to solute elements dissolved into the

pure matrix materials, $\Delta\sigma_{el\ ppt-coh}$ is an increase in yield strength due to coherent precipitation hardening, $\Delta\sigma_{el\ \perp sf}$ is an increase in yield strength due to dislocation density, $\Delta\sigma_{HP}$ is an increase in yield strength due to grain boundaries as described by Hall-Petch and $\Delta\sigma_{Oro}$ is an increase in yield strength due to Orowan strengthening [64].

For the pure aluminum matrix composites reinforced by graphene nanoplatelets produced by powder metallurgy method some parameters in the above equation are not applicable. Since the matrix is pure aluminum and there are no elements dissolve in the matrix, then, $\Delta\sigma_{el\ solute}$ is not applicable for this composite. $\Delta\sigma_{el\ ppt-coh}$ is not applicable as well since there is no coherent precipitation hardening in the composite. As mentioned earlier, in the Orowan strengthening mechanism the precipitates or particles should be inside of the grains. However, in the aluminum matrix composites reinforced by graphene nanoplatelets produced by powder metallurgy usually the grain size of the matrix is less than 200 nm (Figure 21) and the diameter of the graphene nanoplatelets is in micron size. Then, there is no graphene nanoplatelet inside of the matrix grains and the $\Delta\sigma_{Oro}$ is not applicable for the composite. As a result, the only strengthening mechanisms which can contribute in the aluminum matrix composites reinforced by graphene nanoplatelets produced by powder metallurgy are dislocation density and Hall-Petch.

Ferguson et. al. [62] have introduced a model to predict the yield strength of MMCs reinforced by particles. The model is as follow:

$$\sigma_{y_c} = \sigma_{y_m} + \left(1 + F_{bond_{\sigma y-SA}} F_{bond_{\sigma y-weak}}\right) f_r \sqrt{2(\Delta E^*_{f_r^2}/V)Y_c}$$

where

$$F_{bond_{\sigma y-SA}} = \frac{1}{6}(1 - f_{Bond})$$

and

$$F_{bond_{\sigma y-weak}} = 2 - \left(\frac{5}{3}\right) 4\pi(1 - f_{Bond})$$

where σ_{yc} is yield strength of composite, σ_{ym} is yield strength of matrix, $\Delta E_{fr2}^*/V$ is a constant representing the change in “absorbable” elastic energy/volume with the square of f_r which is equal to 0.6 MJ m^{-3} [62] and Y_c is the Young’s Modulus of the composites which calculated in the previous section. Following equation is used to calculate σ_{ym} [65].

$$\sigma_{y_{pure\ Al}} = 10 \text{ MPa} + \frac{0.065 \text{ MPa m}^{1/2}}{\sqrt{D}}$$

To calculate the yield strength of the matrix (σ_{ym}) from the previous equation, we assume that the grain size of the composite samples is the same as the grain size of the milled pure aluminum. The estimate yield strength of the aluminum matrix composites reinforced by alumina particles versus volume fraction of the reinforcement presents in Figure 25. The percentage of change in yield strength of the composites versus particle volume fraction presents in Figure 26.

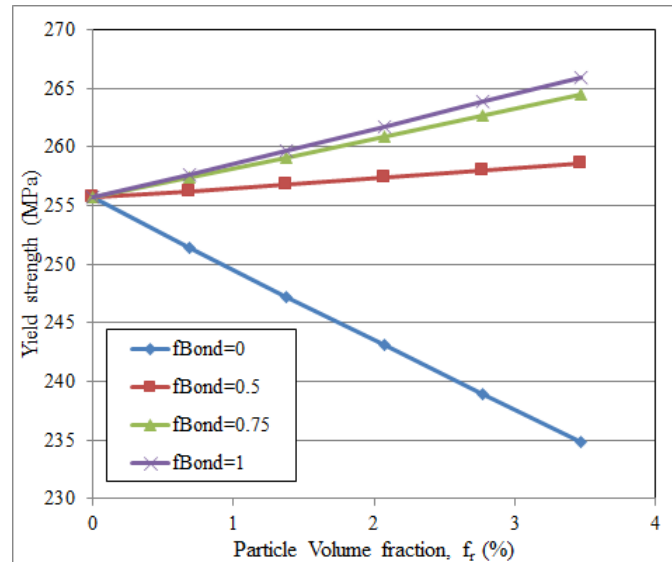


Figure 25. Prediction of yield strength of the composites versus particle volume fraction.

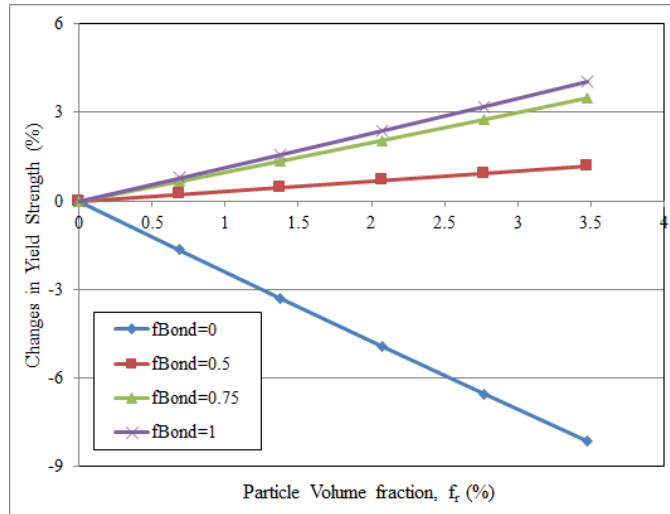


Figure 26. Percentage of change in Yield Strength of the composites versus particle volume fraction.

Chapter 3.

Experimental Procedure

3. Experimental Procedure

The primary materials used in this investigation were a) 99% pure Al powder (Acros Organics, Waltham, MA) with an average particle size of 75 μm , b) $\text{Al}_2\text{O}_{3\text{np}}$ powder (Nanophase, Romeoville, IL) with an average particle size of 47 nm, and c) graphene nanoplatelets (GNP) M5 (XG Sciences, Lansing, MI) with average thickness of approximately 6 nm and average platelet diameter of $\sim 5 \mu\text{m}$. Three different scanning electron microscopes (SEM) (Hitachi S-4800 Ultra High Resolution Cold Cathode Field Emission Scanning Electron Microscope (FE-SEM), JEOL JSM-6460 LV, and TopCon SM-300 Scanning Electron Microscope) were used for characterization of the samples. Figure 28, Figure 29, and Figure 30 shows the SEM micrographs of as-received 99% pure Al powder (subsequently herein referred to as “pure Al”), $\text{Al}_2\text{O}_{3\text{np}}$, and GNPs, at different magnifications, respectively. To produce NC MMNCs, the reinforcements with various wt% (GNPs (0.1, 0.5, and 1 wt%) and $\text{Al}_2\text{O}_{3\text{np}}$ (1, 3, and 5 wt%)) were dispersed in 99.5% anhydrous ethanol by ultrasonication. It is important to indicate that the GNP amount is restricted to 1 wt.% in the aluminum matrix. This is because larger amount of graphene in the aluminum matrix results in poor mechanical properties. Efforts were also made to synthesize samples with GNP amount up to 5 wt.% in the aluminum matrix as a criterion for choosing optimum GNP amount in the aluminum matrix. It was found that the amount of graphene in the aluminum matrix is substantial, a good distribution of reinforcement in the matrix did not occur. Furthermore, the mechanical properties of GNPs sample above 1 wt.% were decreased significantly with increasing GNP. This is because of agglomeration and unsuitable distribution of reinforcement into the aluminum matrix. It is expected that no significant chemical reaction would occur in the room temperature drying process, as no process control agent was used in our work. The Al powder and the reinforcement slurry were added to a Szegvari attritor mill equipped with an alumina reservoir

and milled for 6 hours at 500 rpm using a ball-to-powder weight ratio of 15:1 (5 mm diameter zirconia balls). The procedure used to synthesize nanocrystalline (NC) GNP and Al_2O_3 -reinforced MMNC powders is schematically illustrated in Figure 27.

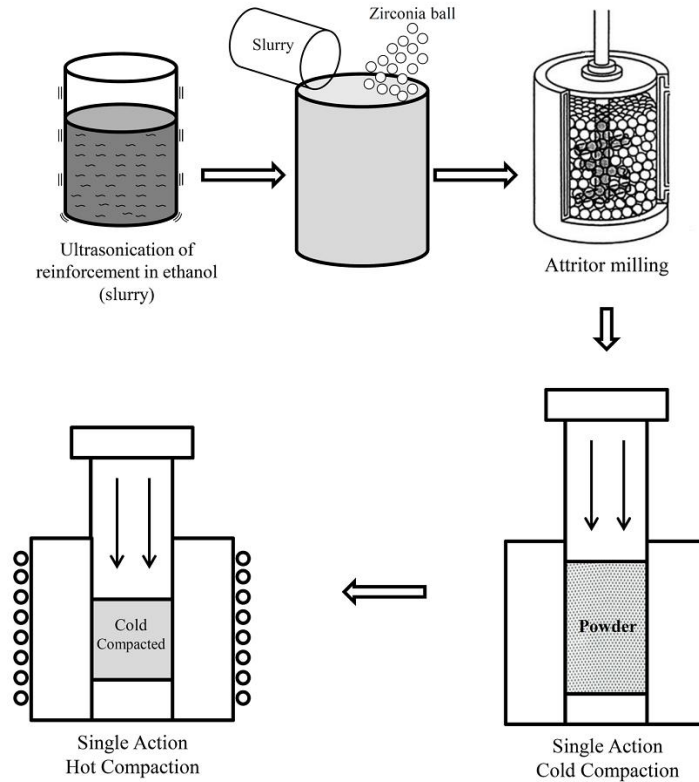


Figure 27. Schematic illustrations to show the attritor milling powder processing technique at room temperature.

Unreinforced pure Al was also produced by the same method to compare with the properties of the composite samples. The milled composite powders were dried at 135°C for 1 hour to remove the ethanol. It is important to note that the initial particle size of aluminum powder was found to be 75 micron. However, after 6 hours of milling, the size and morphology of the aluminum powders changed significantly. In the literature [2], it has been demonstrated that the particle size of powders decrease by milling process. In addition, the morphology of the aluminum powders after milling by attritor mill changed to flaky shape. The graphene nanoplatelets distribute uniformly between flaky shape aluminum powders in matrices. By

adding less than 1wt.% graphene to the aluminum matrix, a good distribution of graphene in the metal matrix can be achieved. The morphology and size of the powders after 6 hours of milling was investigated by SEM. Figure 32 shows the SEM micrographs of flaky shapes Al-1wt.%GNP powders after 6 hours of milling. The dried powders were consolidated by single action cold compaction in a steel mold with 200 MPa at room temperature followed by single action hot compaction in a steel mold with 500 MPa at 525°C in air for 5 minutes such that a 25.4 mm diameter cylinder with a height of 10 mm was produced. Archimedes' method was used to measure the density of the consolidated samples. In this method, the mass of the samples was measured in air; then, the mass of the samples was measured while the sample is suspended in the liquid which is distilled water in this experiment. The following formula was used to measure the density of the samples.

$$\rho = \left(\frac{A}{A - B} \times (\rho_0 - \rho_l) \right) + \rho_l$$

where A is mass of solid in air, B is mass of solid while suspended in the liquid, ρ_0 is the density of the liquid (distilled water) and ρ_l is the air density which is equal to 0.0012 g/cm³. Through density measurement and microstructural evaluation of Fe-2%Cu-0.5%C, Kong et al. [66] showed that, above a certain consolidation pressure, the density of the powder processed samples does not change significantly. Indeed, in previous works, we have shown that a 500 MPa hot compaction pressure used in this work is sufficient to consolidate ball milled Al-Al₂O₃ and Al-GNPs powders [67, 68, 69]. Selected hot compacted samples were annealed at 535°C with measurements of hardness and grain size at 3, 6, 9, 17 and 24 hours. Crystallite size was determined in the powders, hot compacted, and annealed samples using the Scherrer equation [70] from X-ray diffraction (XRD) data gathered by a D8 Bruker diffractometer with Cu K α 1

radiation ($\lambda = 0.15406$ nm) (scanning from $2\theta = 10^\circ$ to $2\theta = 120^\circ$, step size of 0.02° , counting time of 0.3s per step). The Scherrer equation is as follow:

$$t = \frac{K\lambda}{\beta \cos \theta}$$

where t is the mean size of the ordered (crystalline) domains or grain size, K is a dimensionless shape factor, with a value close to unity. The shape factor has a typical value of about 0.9. λ is the X-ray wavelength which is equal to 0.15406 nm in the case of Cu $K\alpha_1$. β is the line broadening at half the maximum intensity (FWHM), after subtracting the instrumental line broadening which is 0.05 for the “D8 Bruker diffractometer” used in this study, in radians. Finally, θ is the Bragg angle in radians. TEM specimens of selected samples were prepared using in-situ lift-out technique by an FEI Strata 400 Dual Beam FIB/SEM. The sample was imaged in FEI Tecnai TF-20 FEG/TEM operated at 200kV. The TEM results were used to investigate the structure of the samples and measure grain sizes. To investigate the mechanical properties of the samples, Hardness Rockwell F, nanoindentation, and compression tests were conducted on the samples. For hardness measurements, five independent Rockwell F Hardness (HR_F) measurements were averaged for each sample at each stage of processing. The Rockwell hardness scale was chosen because it is capable of capturing the representative indentation behavior from a relatively large area of the MMNC sample surfaces. Nanoindentation tests were also conducted on selected samples to measure the Young’s Modulus and hardness of the samples. Nine measurements were averaged for the nanoindentation results. Compression test was conducted on the cylindrical shape bulk samples. The dimension of the samples for the compression test were 8 mm in diameter and 8 mm in length. The aspect ratio of the compression test samples was constant for all samples and it was equal to one. The strain rate was constant

and equal to 1×10^{-3} /s in all compression tests. We have used a stationary grip on the bottom and a self-leveling platen on the top. The compression tests were continued until failure. To investigate the tribological behavior of the samples, pin-on-disk tests under dry condition were conducted. In the tests, cylindrical pins with dimension of 6 mm in diameter and 8 mm in height were utilized from the hot compacted samples. The counterpart disk material was made of stainless steel 440C with dimension of 55 mm in diameter and 10 mm in thickness. The pin-on-disk experiment was conducted for different normal loads (5, 10 and 15 N) and sliding speeds (50, 100 and 150 rpm) at a constant sliding distance of 1.13 km. The coefficient of friction (COF) and volume loss (wear rates) were measured during the wear tests. The worn surfaces of the samples were investigated using Optical Microscope (OM) and Scanning Electron Microscope (SEM). The debris obtained after the wear test were investigated using Scanning Electron Microscope (SEM) and Energy Dispersive Spectroscopy (EDS).

Chapter 4.

Results and Discussion

4. Results and Discussion

4.1.Characterization

The as received powders were investigated by SEM. Figure 28 shows the SEM micrograph of as received aluminum powder at two different magnifications. These images indicate that the average particle size of the as received aluminum powder is about 75 μ m, and the particles are rounded but not spherical.

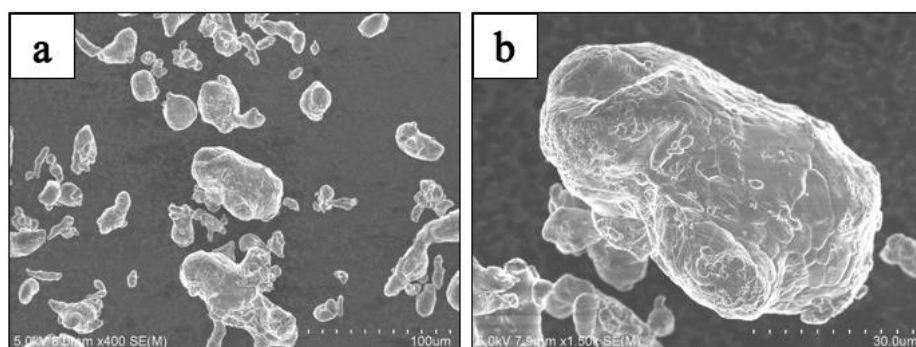


Figure 28. SEM micrograph of aluminum powders at different magnifications a) 400X and b) 1500X.

Figure 29 shows the SEM micrograph of as received alumina nanoparticles at two different magnifications. This figure shows that the average particle size of alumina particles is around 47nm, and the particles are spherical and often agglomerated.

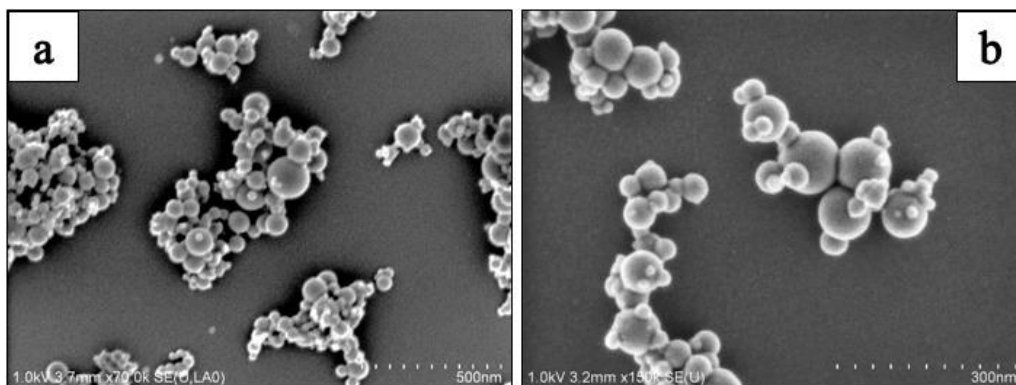


Figure 29. SEM micrograph of alumina nanoparticles at different magnifications a) 70000X, b) 150000X.

Figure 30 shows the SEM micrograph of as received graphene nanoplatelets at four different magnifications. The figures show the nanoplatelet shape of graphene, with the average thickness of approximately 6nm and average diameter of 5 μ m.

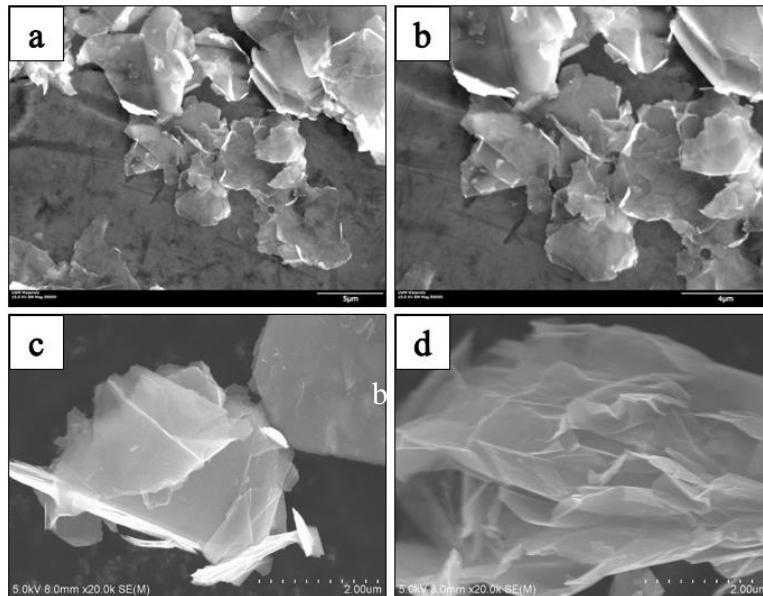


Figure 30. SEM micrograph of Graphene nanoplatelets at different magnifications a) 3000X, b) 5000X, c) 20000X and d) 20000X.

The relative density of the bulk samples after consolidation processing was measured by Archimedes method.

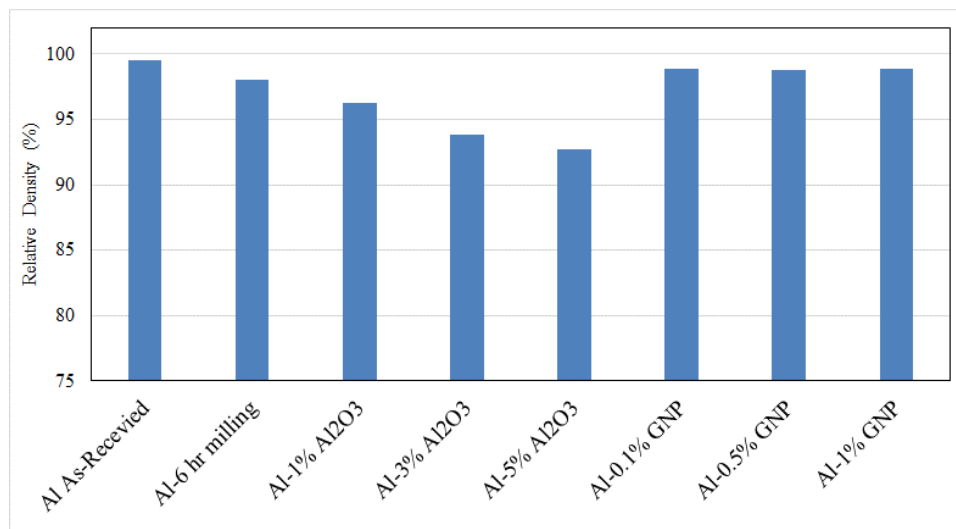


Figure 31. Relative density measurements of different samples from Archimedes method.

Figure 31 shows the relative density of the as-received pure aluminum, milled pure aluminum and aluminum matrix composites reinforced by alumina and graphene nanoplatelets. The morphology of as-received pure aluminum powder is rounded (Figure 28). Due to the plastic deformation during ball milling, the morphology of the powders changed to flake shape [68]. The morphology of the milled aluminum powder is shown in Figure 32.

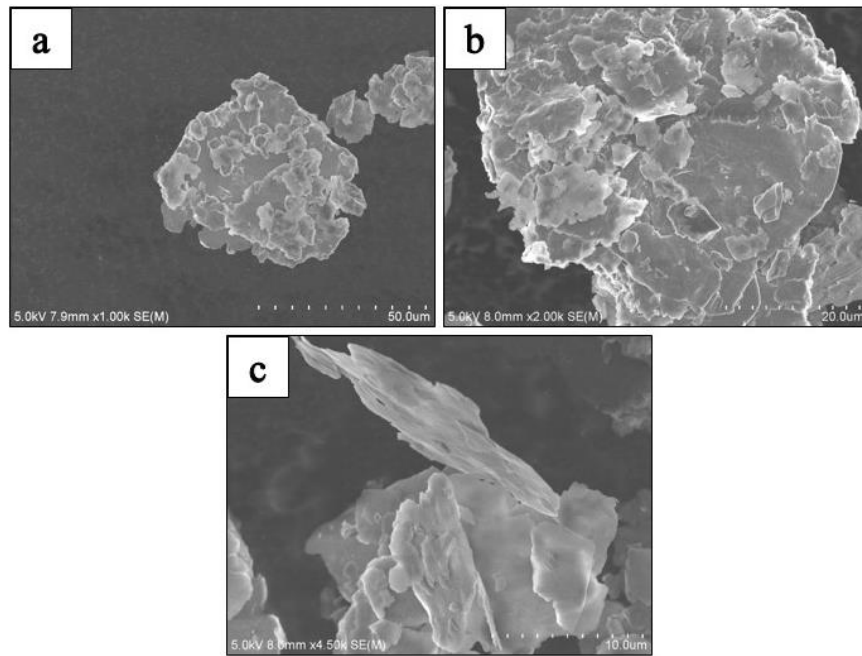


Figure 32. SEM morphology of milled powders. a) Pure aluminum at 1000X, b) pure aluminum at 2000X, and c) aluminum-1%GNP at 4500X after 6 hours of milling.

Since the as-received pure aluminum has a round shape, during consolidation process, the powders can move easily compared to the flake shape powders. As a result, the compressibility of the as-received pure aluminum is better compared to the other powders, and the relative density of the as-received pure aluminum is above 99%. However, after milling the morphology of the powders were flaky and the compressibility of the milled powders was lower compared to the un-milled powders. As a result, the relative density of the milled pure aluminum is lower compared to the as-received powder after consolidation. Adding reinforcements to the

pure aluminum matrix changed the compressibility behavior of milled powders. By adding graphene nanoplatelets to the aluminum matrix, the relative density of the composites slightly increased compared to the milled pure aluminum powders. It has been shown that graphene nanoplatelets can act as a solid lubricant [68]. As a result, graphene nanoplatelets can help flakey shape aluminum powders to move against each other during compaction and improve the compressibility behavior. However, adding alumina nanoparticles to the pure aluminum matrix has negative effects on the relative density. As we can see from Figure 32, the relative densities of aluminum matrix composites reinforced by alumina nanoparticles are between 87%-94%, and these are much smaller compared to other samples including pure aluminum or aluminum-graphene.

The XRD results for as received powders, milled powders, milled composite powders and consolidated bulk samples is show in the following figures. Figure 33 to Figure 35 show the XRD results for the powders. In all of the XRD spectrums, there are 8 peaks for aluminum. The 2θ measurement for these spectrums are approximately 38.4° , 44.6° , 65.0° , 78.2° , 82.4° , 99.0° , 111.9° and 116.5° . In addition to these Al peaks, there is a small carbon peak originated from GNP at 2θ value of 26.4° in Figure 35 [67].

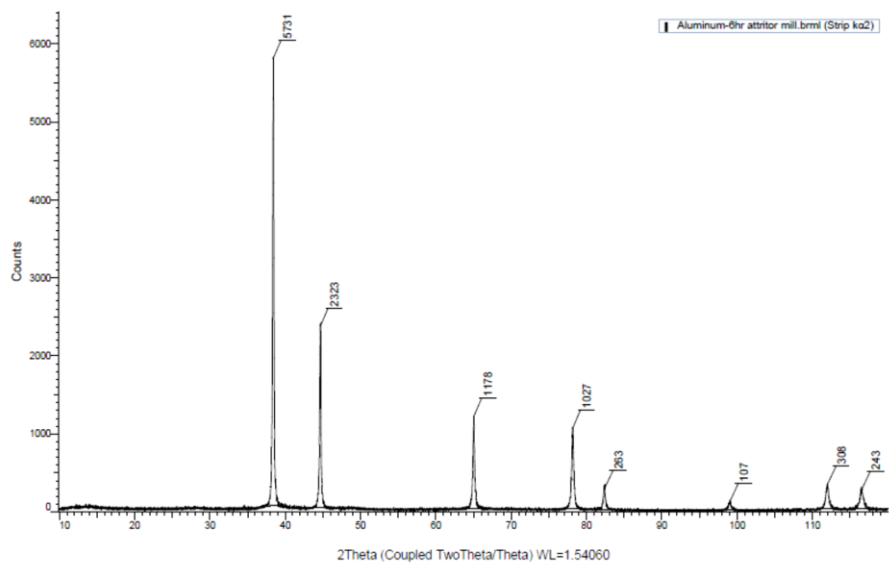


Figure 33. XRD spectrum of aluminum powder after 6 hours of ball milling.

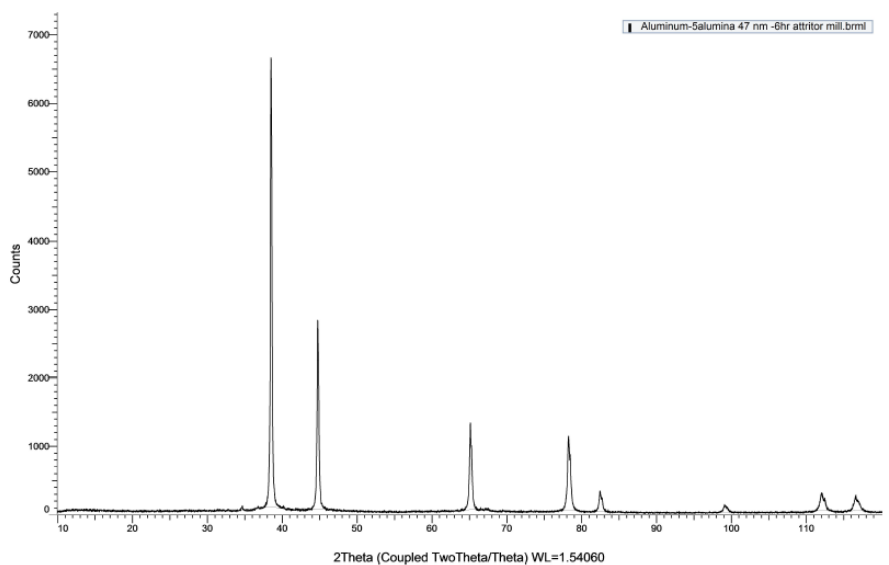


Figure 34. XRD spectrum of Al-5%Al₂O₃ with average particle size of 47nm composite powders milled for 6hr.

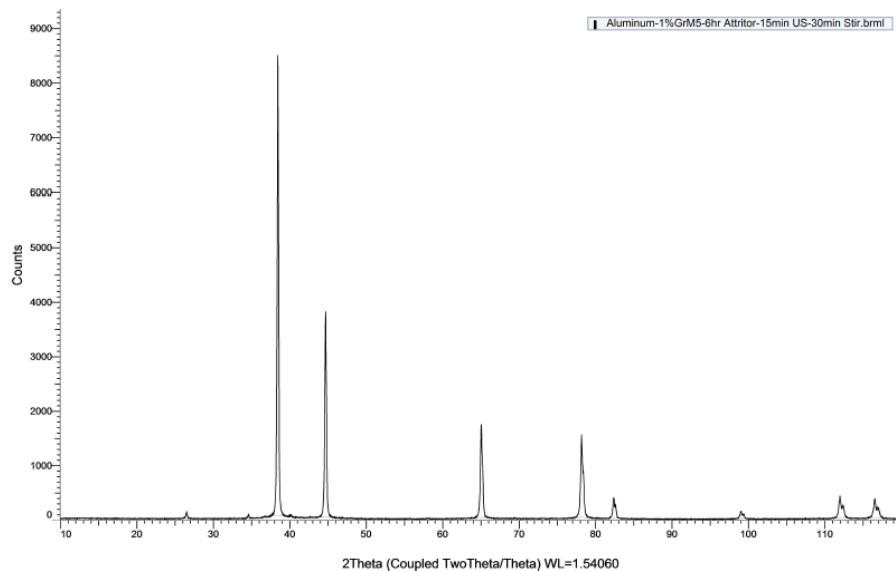


Figure 35. XRD spectrum of Al-1%graphene nanoplatelets composite powders milled for 6hr.

Figure 36 to Figure 38 presented the XRD results on the bulk samples after consolidation processing.

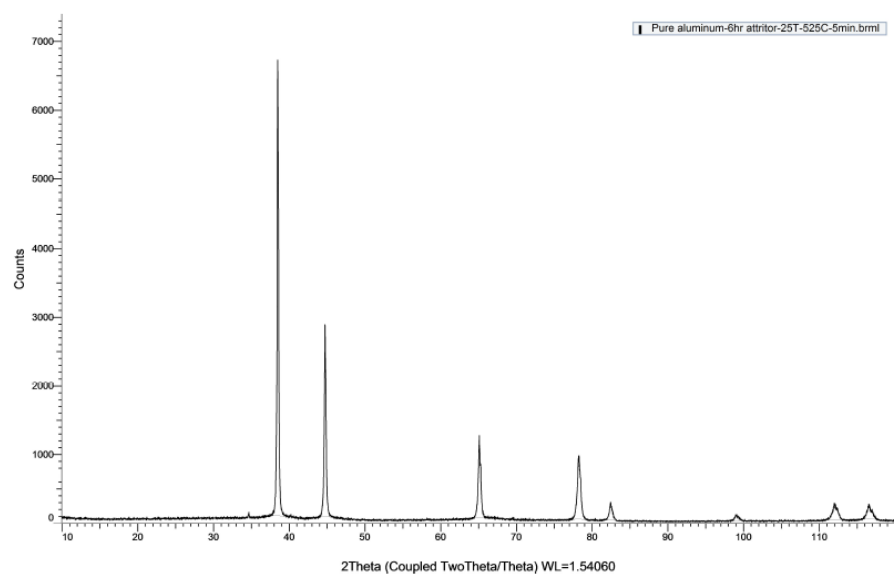


Figure 36. XRD spectrum of hot compacted pure aluminum sample.

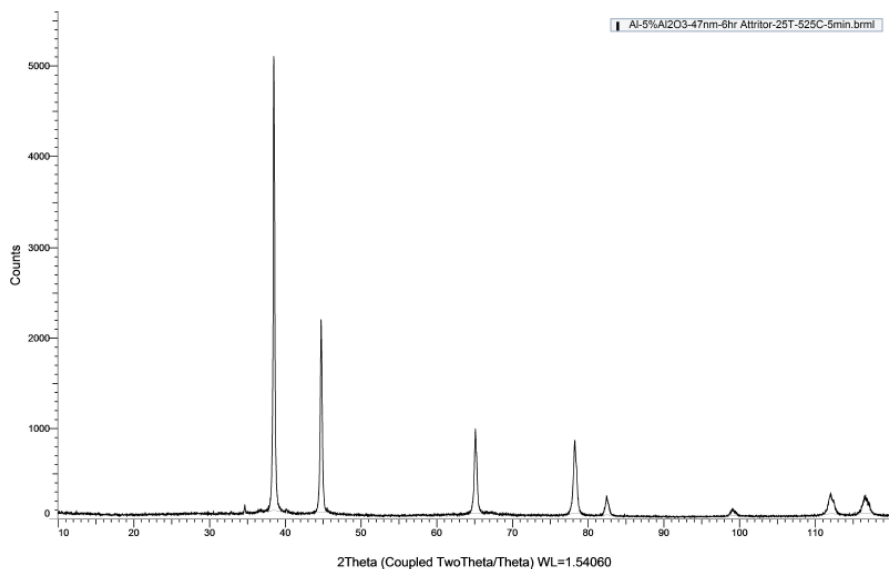


Figure 37. XRD spectrum of hot compacted Al-5%Al₂O₃ composite sample.

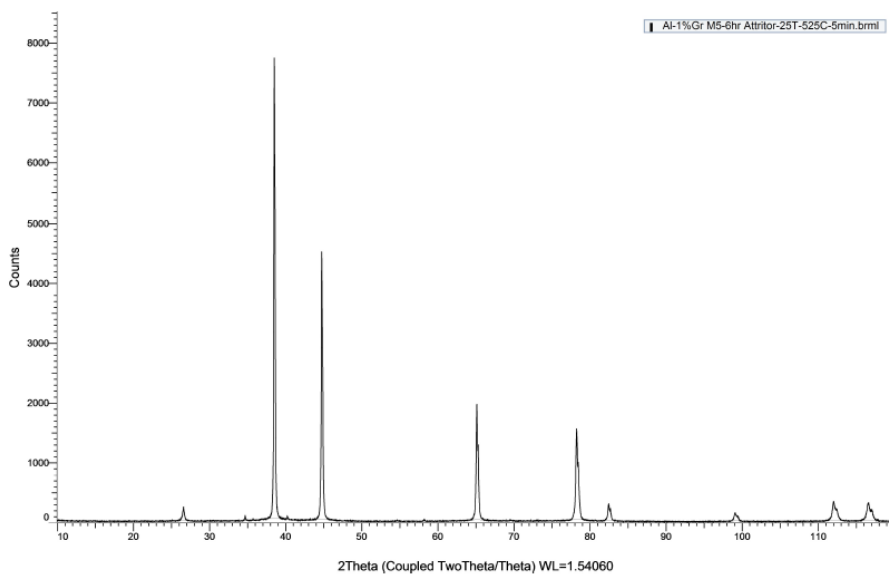


Figure 38. XRD spectrum of hot compacted Al-1% graphene nanoplatelets composite sample.

The XRD spectrum of the bulk samples are the same as the XRD spectrum of powders samples. These results prove that during consolidation processing, including single action cold compaction followed by single action hot compaction, there is no detectable reaction leading to the formation of new phases. The XRD analysis was also conducted on selected samples after 24 hours of heat treatment at 535°C.

Figure 39 shows the XRD patterns of pure Al (black, bottom) and Al-matrix composites reinforced by 1 wt% GNP before (blue, middle), and after (red, top), heat treatment. The XRD pattern of the pure Al shows the three typical peaks for Al at 2θ of 38.4° , 44.7° and 65.1° . The XRD pattern for the hot consolidated Al-1 wt% GNP shows the three peaks of Al at the same 2θ values of pure Al. In addition to these Al peaks, there is a small carbon peak originated from GNP at 2θ value of 26.2° . This peak corresponds to (002) reflection of graphene with inter planar distance of 0.339 nm (Figure 40) [71]. The XRD pattern measurement was also conducted on the Al-1 wt% GNP sample after 24 hours of heat treatment at 535°C to examine the effect of heat treatment on formation of any new phases in the composite sample.

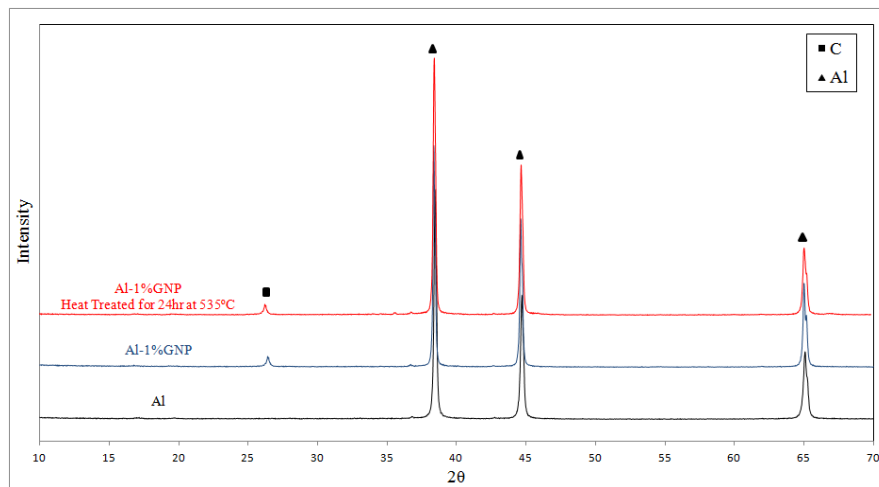


Figure 39. XRD patterns of pure Al (black) and Al-matrix composites reinforced by 1 wt.% GNP before (blue) and after (red) heat treatment.

As seen in the Figure 39, the XRD peak positions for the Al-1 wt% GNP sample after heat treatment are identical to the XRD result of the Al-1 wt% GNP before heat treatment, which indicates that no phase transformation or carbide formation have occurred in the Al-1 wt% GNP sample during heat treatment. The current findings in our study are clearly different from the XRD results reported in the previous study [17] exhibit peaks at $2\theta = 31.8$, 55.0 , and 72.5° indicating the formation of aluminum carbide in Al-0.1 wt% graphene composites.

It is worth mentioning that the materials chosen for the milling media and the reservoir are highly wear-resistant and, therefore, the possibility of contamination is very low. As seen in XRD results, the chemical analysis was unable to identify the presence of measurable contamination from milling media in the specimens produced in this study.

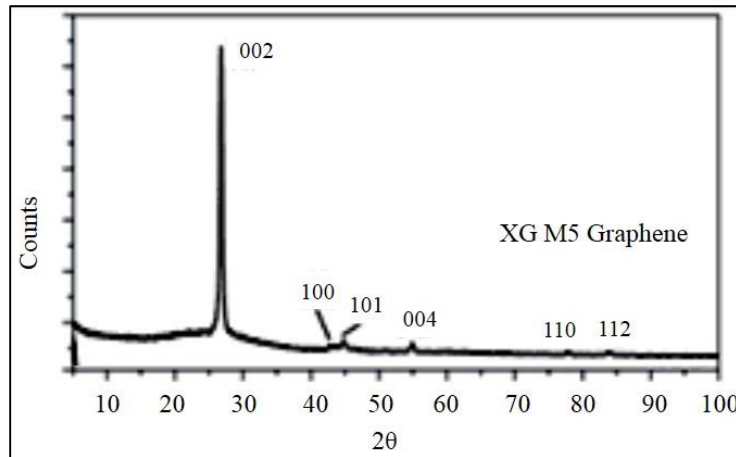


Figure 40. XRD results of as received GNPs [71].

The microstructure of the samples has been investigated by SEM, EDS and TEM to show the presence of reinforcements embedded in the matrices and distribution of the reinforcements.

Figure 41 presents the SEM images of (fractured) cross-sections of (a) pure Al, (b) 1 wt% GNP, (c) and (d) 5 wt% Al_2O_3 specimens synthesized in this study to show the distribution of the reinforcements (GNPs and Al_2O_3) in the Al matrix. The general shape of the Al matrix grains shows an elongated structure resulting from the ball milling and the compaction processes. Figure 41a portrays the fracture surface of the pure Al sample and clearly depicts such elongated Al grains without any impurities and reinforcements. As one can see from Figure 41b, c and d, the existence of reinforcements is clear for Al- Al_2O_3 and Al-GNP samples. The GNPs (Figure 30) sit in between elongated Al grains (Figure 41b), and examples of the Al_2O_3 nano particles

(Figure 29) with spherical morphology also appear between the flake shaped Al matrix grains (Figure 41c and d).

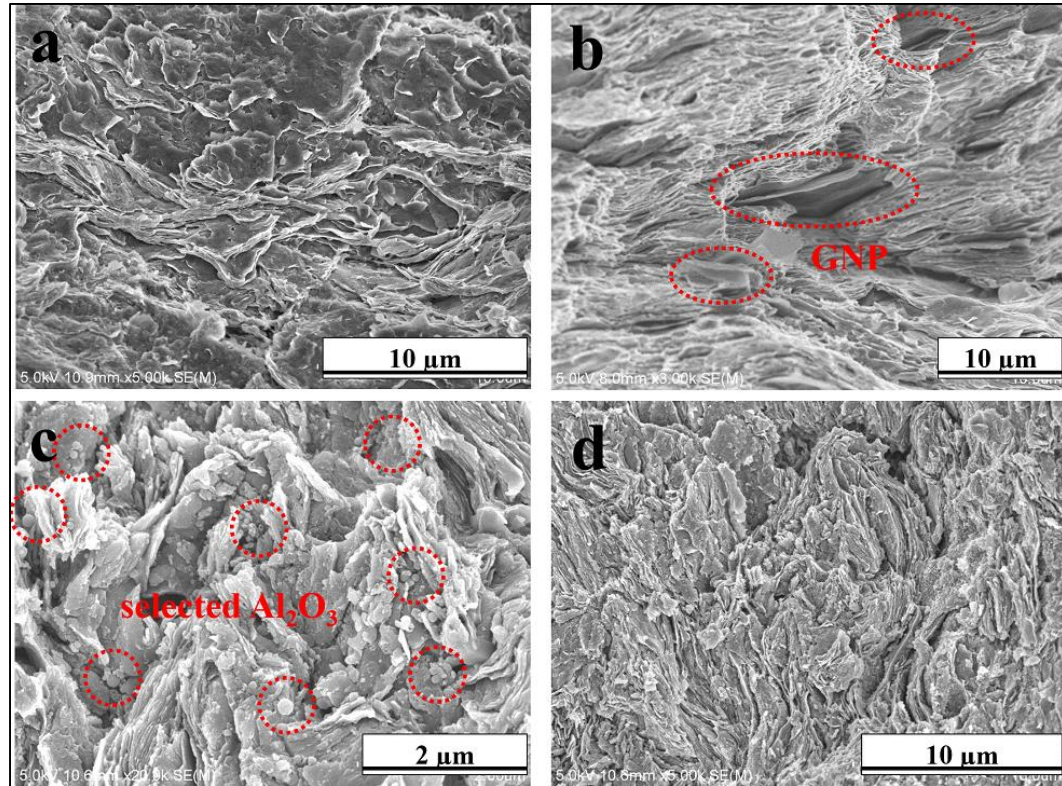


Figure 41. SEM micrographs of the fractured sections from (a) pure Al, (b) Al-1 wt.% GNP, and (c) and (d) Al-5 wt.% Al_2O_3 samples with different magnifications.

In Figure 42, we show an example of an SEM image of the fracture surface of the Al-1 wt% GNP sample and corresponding EDS dot maps of C (red) and Al (blue) elements. It is clear that some GNPs are positioned between Al matrix grains.

Figure 43 shows the EDS intensity plots from the Al-5 wt% Al_2O_3 and Al-1 wt% GNP specimens indicating presence of Al, O, and C elements. Further, the fractured surfaces of the composite samples clearly show that the reinforcements are well-embedded in the metal-matrix. Based on low magnification SEM images, it was found that the GNP and Al_2O_3 reinforcements are homogeneously dispersed throughout the Al matrix (e.g., Figure 41d).

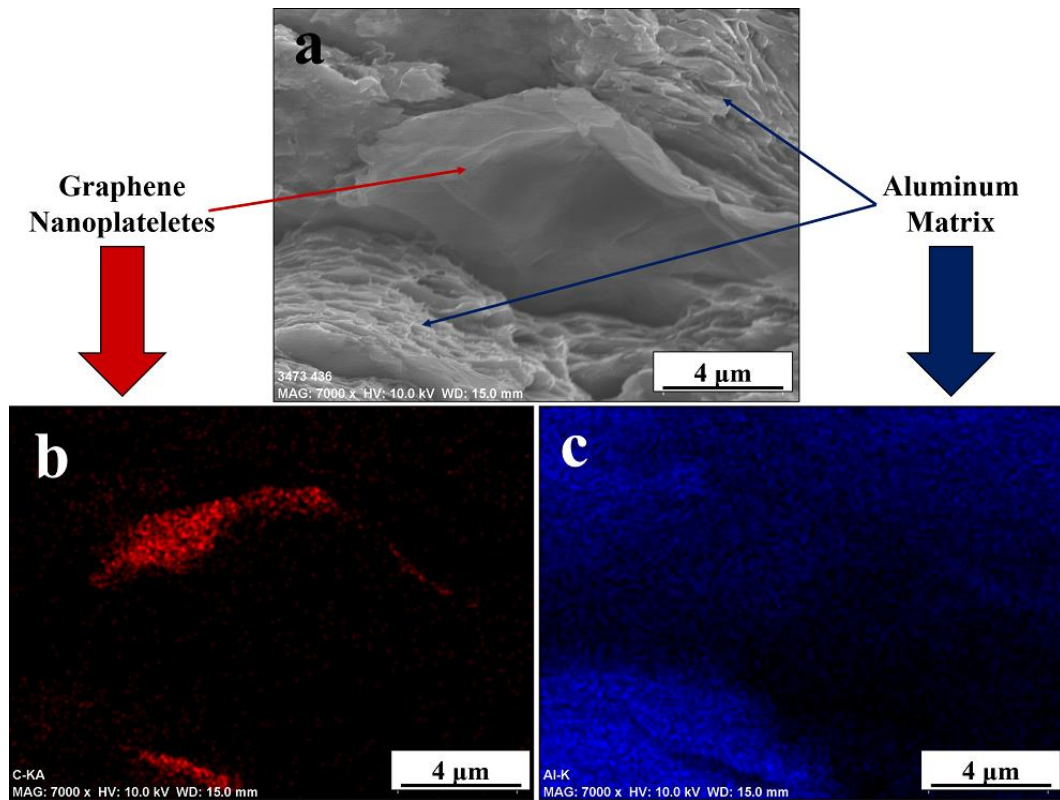


Figure 42. (a) SEM micrograph of the fractured Al-1%GNP specimen and the corresponding EDS dot maps of (b) C (red) and (c) Al (blue) elements.

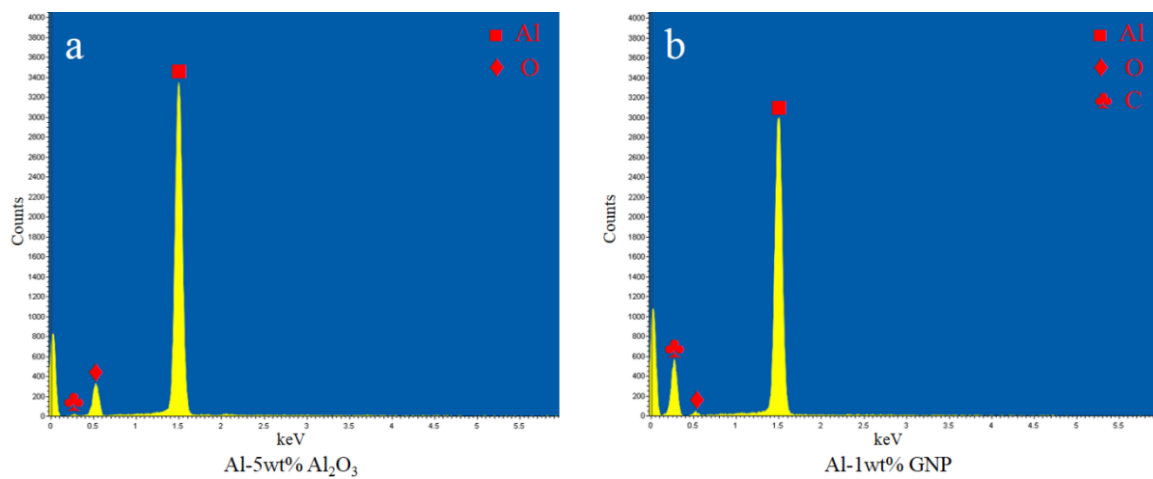


Figure 43. EDS intensity plots from the fractured sections of (a) Al-5 wt.% Al₂O₃ and (b) Al-1 wt.% GNP.

Figure 44a and b present the TEM microstructures of pure aluminum samples at different magnifications. These figures show that the pure aluminum sample has a layered microstructure. Figure 44c shows the oxygen enriched area in the pure aluminum samples. It shows that oxide layers were formed on the surface of aluminum particles. Aluminum powders were heavily deformed during ball milling and consolidation processing. Dislocations were generated during the powder metallurgy processing in the powders. The dislocation structure of pure aluminum sample is presented in Figure 44d.

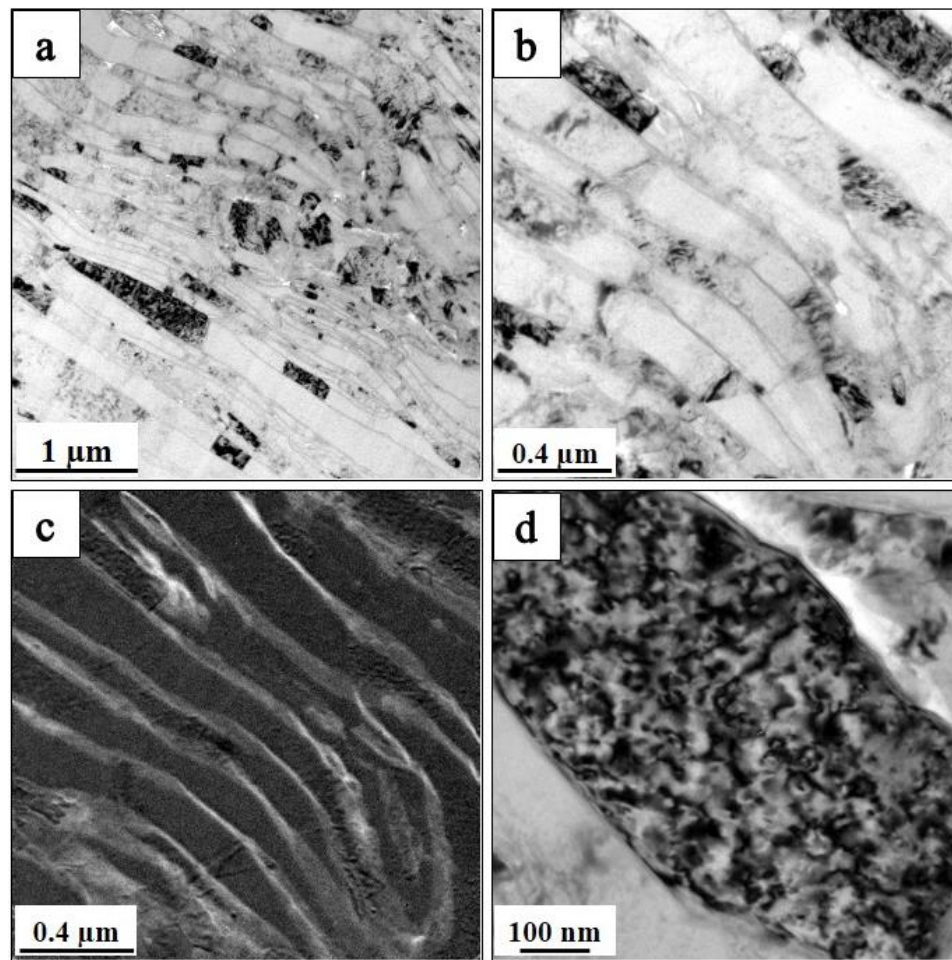


Figure 44. TEM images of pure aluminum sample to show a) and b) microstructures at different magnifications, c) oxygen enriched locations, and d) dislocation structure.

Figure 45a and b present the TEM microstructures of Al-5%Al₂O₃ samples at different magnifications. These figures show that the Al-5%Al₂O₃ samples have also layered

microstructures. The Dislocation structure of Al-5%Al₂O₃ is presented in Figure 45c (bright field) and Figure 45d (dark field).

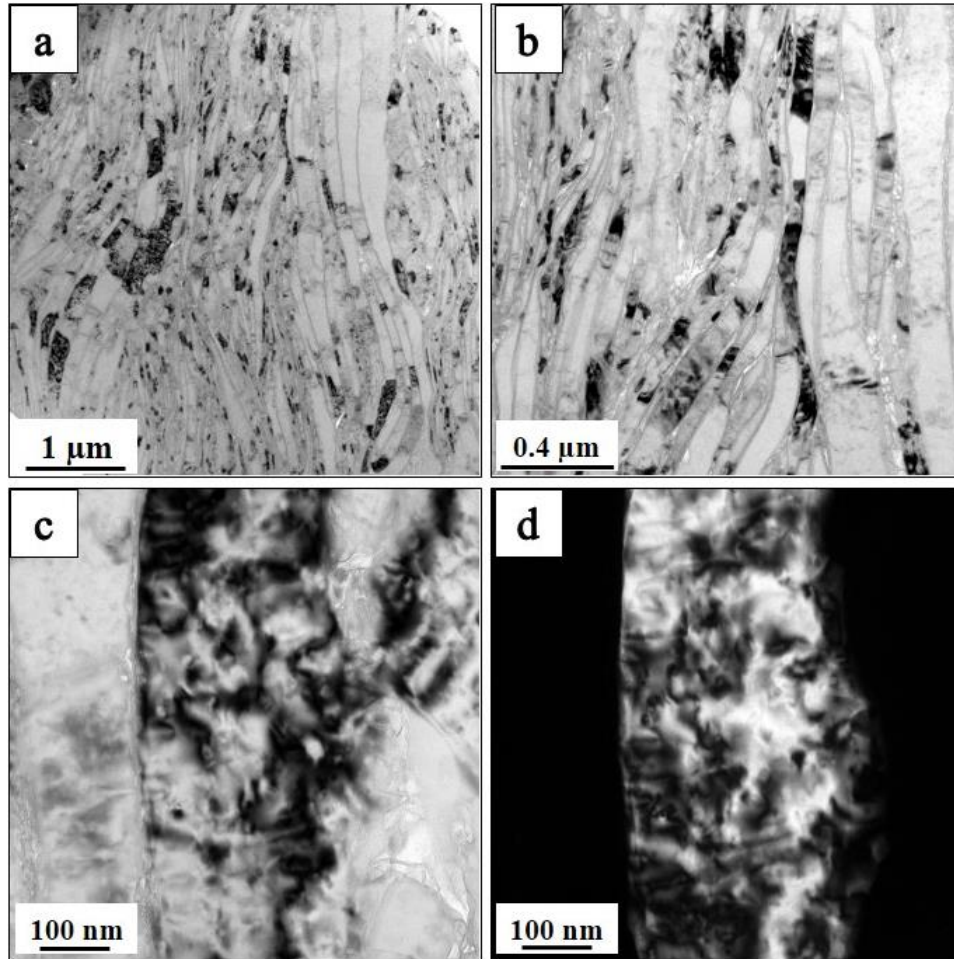


Figure 45. TEM images of Al-5%Al₂O₃ sample to show a) and b) layered microstructures at different magnifications, c) dislocation structures in bright field and d) dislocation structures in dark field.

Figure 46 a and b show the layered microstructures of Al-5%Al₂O₃ samples at two different magnifications. Alumina nano particles are shown by red arrows in the Figure 46a and b. The average particle size of alumina is about 50 nm as shown. In addition, these figures show that the alumina nano particles are located in between aluminum grains instead of within the grains. The EDS results on the aluminum matrix and alumina nano particles have been shown in

Figure 46c and d, respectively. These results show the presence of alumina nano particles embedded in the aluminum matrix.

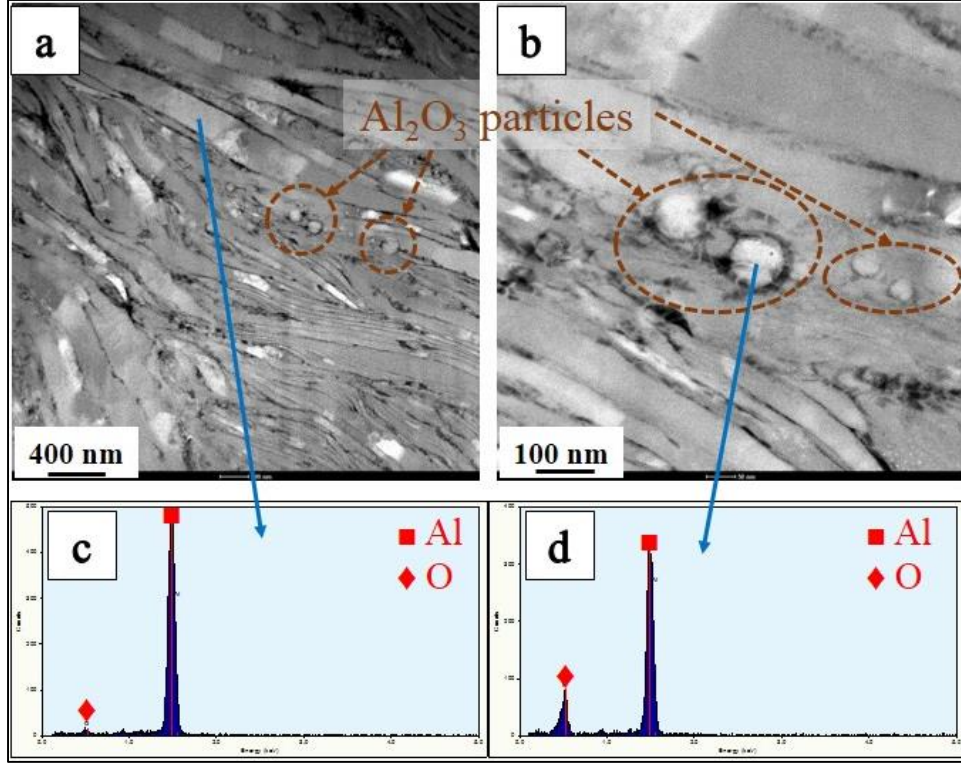


Figure 46. TEM images of Al-5%Al₂O₃ sample to show a) and b) alumina nanoparticles in the layered microstructures at different magnifications, c) and d) the EDS results on the aluminum matrix and alumina nanoparticles respectively.

Figure 47 shows the TEM micrographs to elucidate the layered structures and grain sizes of Al-1 wt% GNP samples at increasing magnifications. Here, some of the GNPs and Al matrix grains are indicated using red and blue arrows, respectively, in high magnification images, i.e., Figure 47c and d. The thickness of GNP is about 6 nm (Figure 47d) which is similar to the initial thickness of as received GNPs.

Selected area diffraction (SAD) was conducted on the Al-1%GNP sample and the results are presented in Figure 48. The working area which the SAD method covered was about 200 nm. The figures illustrate that the SAD covers the area which has more than one grain. In addition,

the thickness of GNPs is about 6 nm as shown earlier. As a result, identifying graphene nanoplatelets by the SAD method is complicated.

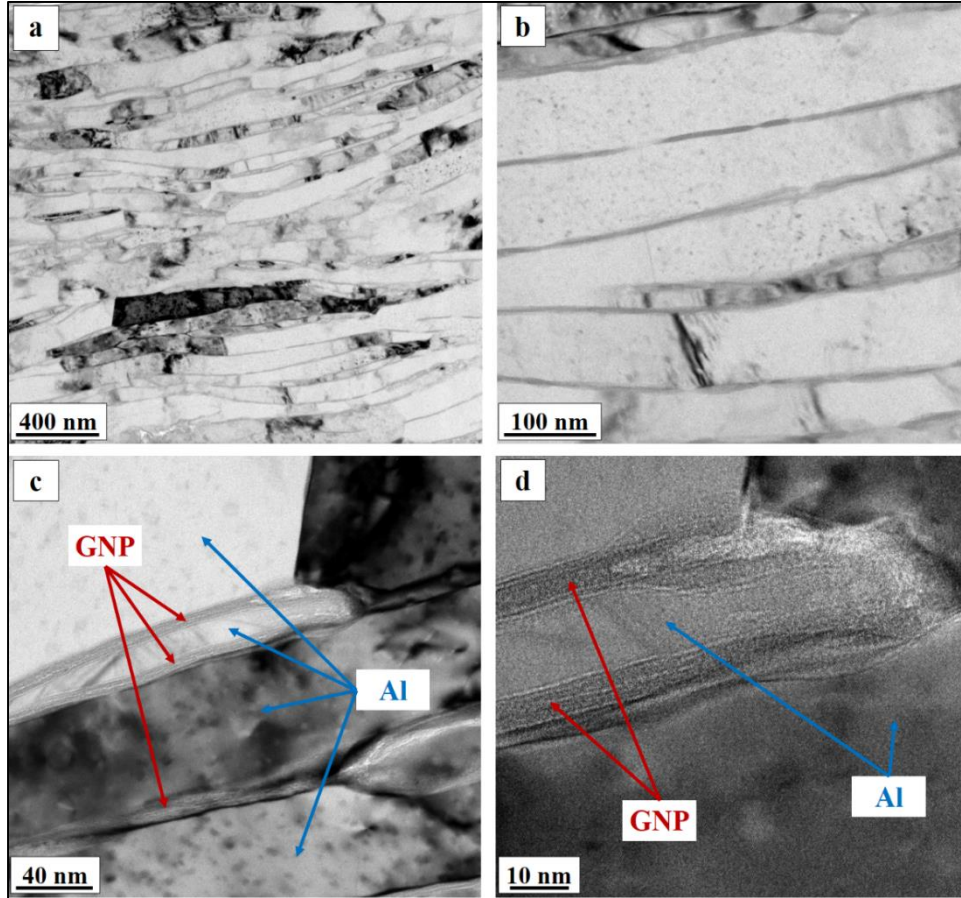


Figure 47. TEM images to show the microstructures and grain size distributions of Al-1%GNP samples with increasing magnifications. Embedded GNPs and Al matrix are indicated using red and blue arrows, respectively, in (c) and (d).

Al-5%GNP has been synthesized to investigate the microstructure and show graphene nanoplatelets in the sample. The amount of graphene is much more in this sample compared to the Al-1%GNP sample. Figure 49 shows the microstructure of AL-5%GNP samples. As a result of increasing the amount of graphene in the sample to 5%, the distribution is less uniform, and some clustering and agglomeration is visible in the sample. The clusters of graphene nanoplatelets in the Al-5%GNP have been shown with a blue arrow in Figure 49b. In addition, single layers of graphene have been shown with the two arrows in Figure 49b.

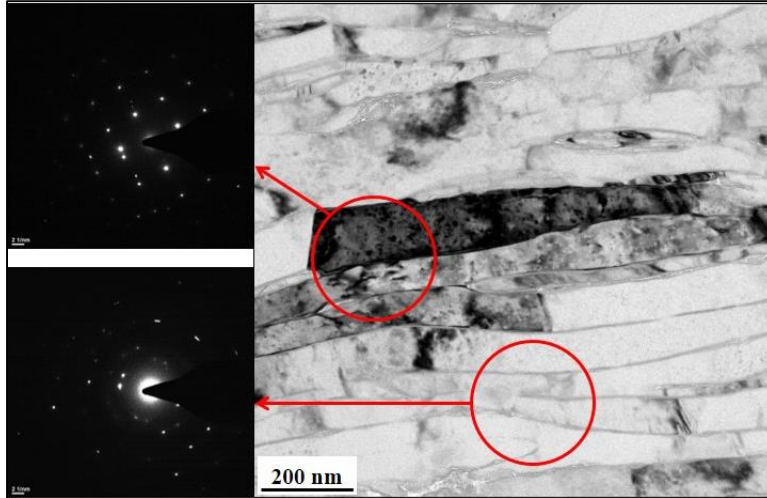


Figure 48. Selected Area Diffraction Pattern (SAD) on Al-1%GNP sample.

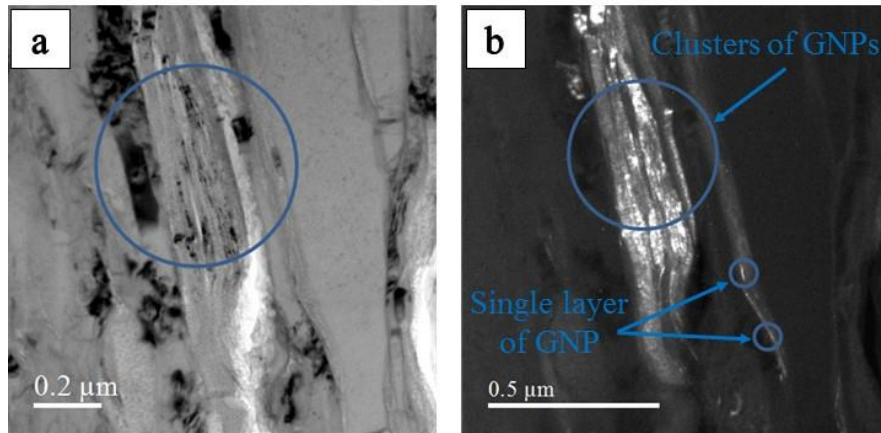


Figure 49. a) and b) TEM images of Al-5%GNP at different magnifications.

The distance between layers in the GNPs embedded in the aluminum were measured by the TEM images. Figure 50 shows that the distance between layers of graphene in the Al-5%GNPs sample which is equal to 0.34 nm. The same results have been reported by Chen et. al [32].

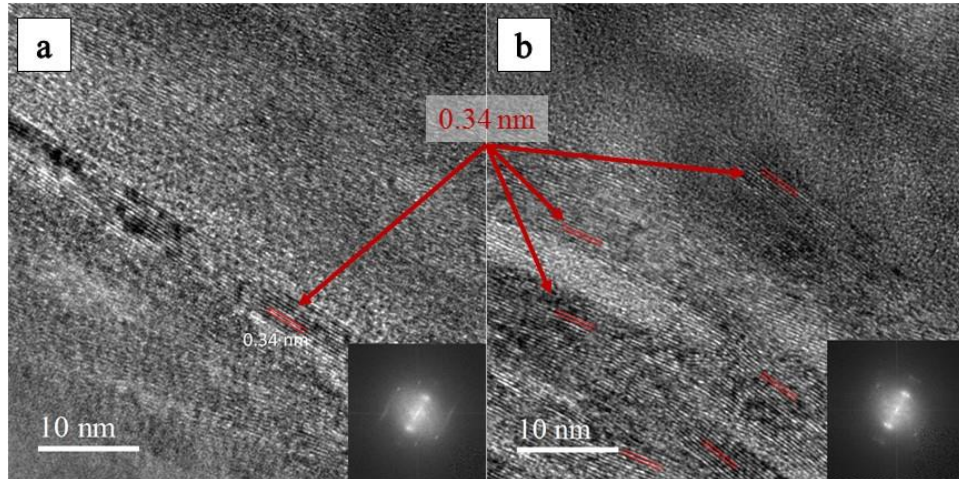


Figure 50. The distance between layers of graphene in Al-5%GNPs sample.

4.2. Grain Size Measurements

The crystallite size of the samples was measured from the Scherrer equation by using the XRD spectrums. Table 4 and Figure 51 shows the information and also the crystallite size of the powder and bulk of pure aluminum, aluminum matrix composites reinforced by graphene nanoplatelets and aluminum matrix composites reinforced by alumina nano particles. The grain sizes were indirectly extracted using the XRD data of specimens in the direction perpendicular to the consolidation direction in conjunction with the Scherrer equation.

Table 4. Crystallite size measurements of pure aluminum, aluminum matrix composites reinforced by graphene nanoplatelets and aluminum matrix composites reinforced by nano alumina particles using Scherrer equation.

Matrix		Pure Al									
Reinforcement	Material	-		Al ₂ O ₃					Graphene nanoplatelets		
	Weight (%)	0		1	2	3	4	5	0.1	0.5	1
	Size (nm)	0		47 nm					Thickness 6 nm Diameter 5 μm		
Milling Time (hour)		0	6	6					6		
Grain Size (nm)	Powder	132	43	42	40	48	44	53	54	44	51
	Bulk	140	69	55	55	63	61	50	75	68	74

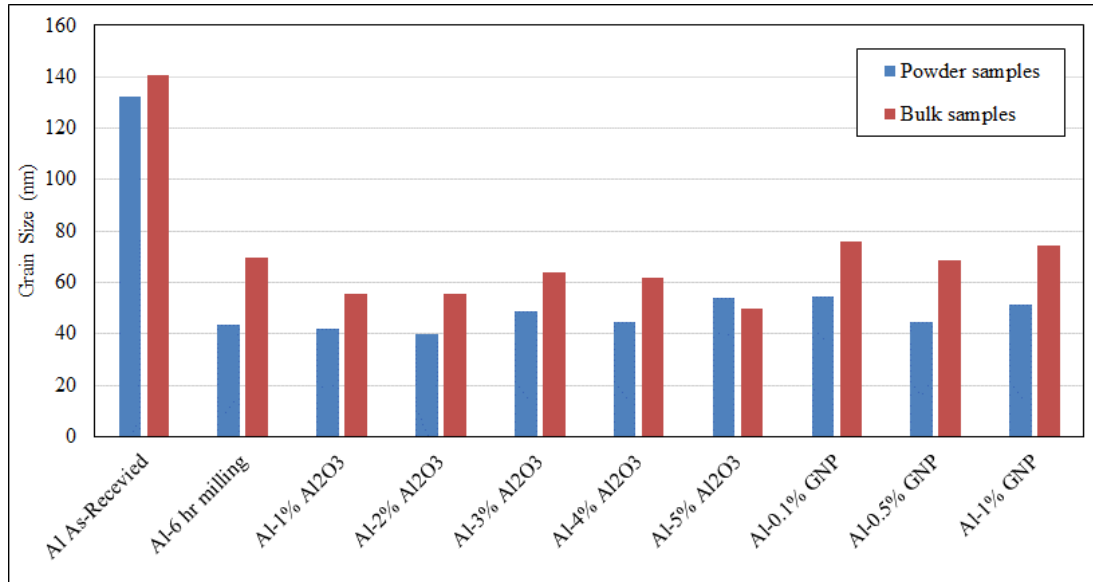


Figure 51. Crystallite size measurements of pure aluminum, aluminum matrix composites reinforced by graphene nanoplatelets and aluminum matrix composites reinforced by nano alumina particles using Scherrer equation.

The results show that grain refinement occurs by the powder metallurgy processing and the grain size of the as-received pure aluminum was decreased from about 132 nm to about 43 nm after 6 hours of ball milling. Additionally, the weight fraction, size, shape and types of reinforcements do not have a significant effect on the average grain size of the powders. Figure 52 shows the same results. $\Delta D_{\text{milling}}$ is equal to $D_{\text{As-Received}} - D_{\text{milling}}$ after milling of the powders. The results show that $\Delta D_{\text{milling}}$ for all of the samples was between 77 to 92 nm. It means that during a given time of milling the average grain size of the pure aluminum powders decreases to almost the same size and it is independent of type, size, morphology, and weight fraction of the reinforcements. Moreover, the results show that there is a small grain growth during consolidation processing in all samples. The grain size after hot compaction for all samples ranged from ~50 to 75 nm. It has been reported that after cryomilling, the milled powder is nanosize (about 25 nm), but requires a high temperature/high vacuum degassing step to remove

the PCA following by a consolidation processing such as HIP. After processing, the grain size of the bulk samples is around 100 nm [72].

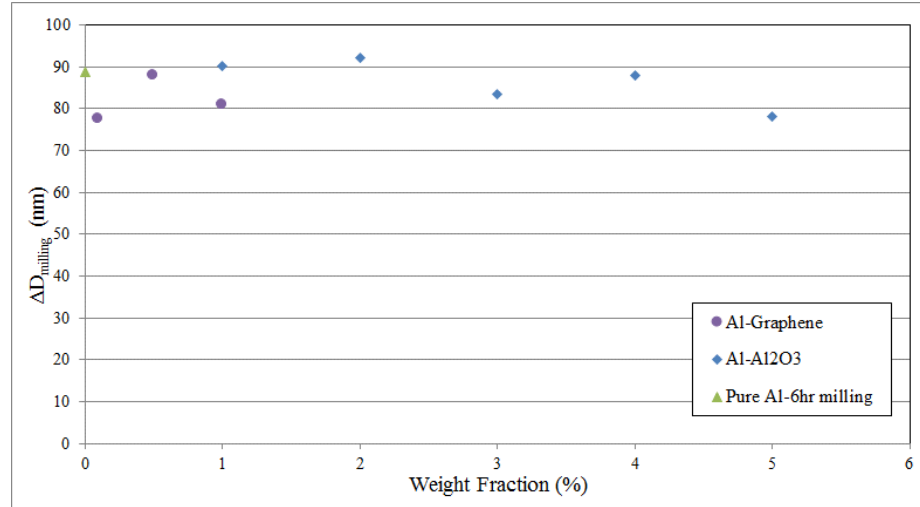


Figure 52. $\Delta D_{\text{milling}}$ ($D_{\text{As-Received}} - D_{\text{milling}}$) versus weight fraction of the milled powders.

The range of grain sizes after consolidation processing in this study are smaller compare to the grain sizes which were reported by other researchers [72]. These crystallite sizes were further confirmed by investigating the microstructures and the grain size measurements of the selected samples by TEM [67].

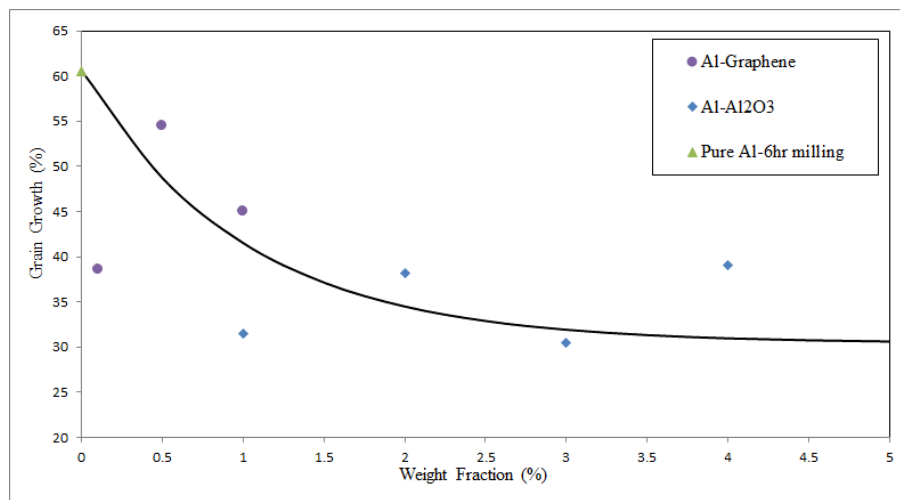


Figure 53. Percentage of grain growth after single action hot compaction for pure aluminum and composite samples.

Grain growth of the samples were calculated for pure aluminum and aluminum matrix composite samples. The results are presented in Figure 53. As we can see from the graph, the grain growth decreases by increasing the amount of reinforcements.

For the milled pure aluminum, the percentage of grain growth is about 60%. In the composite samples the reinforcement acts as a barrier for grain growth during single action hot compaction. The reinforcements pin the grain boundaries and do not allow the grains to grow. The results show that the alumina particles pin the grain boundaries more than the graphene nanoplatelets. This could be due to the morphology of the reinforcements. Alumina particles have a round shape and a very small average size of about 47 nm. Therefore, these particles can easily sit on the grain boundaries and pin the grain boundaries. However, graphene nanoplatelets have a flake shape with thickness of around 6 nm and diameter of 5 μm . They cannot pin the grain boundaries as well as alumina nano particles.

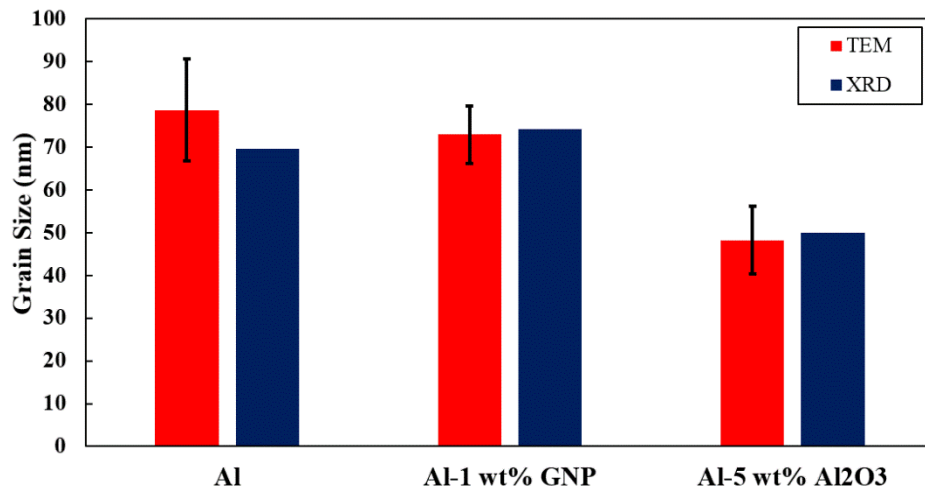


Figure 54. Average grain sizes of pure Al, Al-1 wt.% GNP, and Al-5 wt.% Al₂O₃ characterized using XRD and TEM analyses.

Figure 54 shows the average grain sizes of selected samples, i.e., pure Al, Al-1 wt% GNP, and Al-5 wt% Al₂O₃, obtained from the XRD and TEM experiments. For the TEM grain

size analysis, at least ~200 grains were used to calculate the average grain size. The error bars in the figure denote the standard deviations in the measured grain sizes from TEM images.

As shown in Figure 54, the crystallite sizes determined from the XRD results match closely with the grain sizes measured from TEM images in the direction perpendicular to the consolidation direction, which confirms the accuracy of the average grain sizes determined from XRD for each specimen as listed in Table 4. In general, the GNP-reinforced samples showed larger grain sizes than the unreinforced (i.e., pure) Al, and it was found that the Al-Al₂O₃ MMNCs possessed the smallest grain sizes.

4.3. Mechanical Properties

4.3.1. Hardness Measurements

Table 5 shows the hardness Rockwell F (HRF) measurements for pure Al and Al-matrix composites reinforced by Al₂O₃ nanoparticles and GNPs. Table 5 concludes that annealing heat treatments produced no significant grain growth or coarsening in any of the materials - a result that is consistent with the results of other studies [80].

It is assumed that annealing would eliminate any residual stress and excess dislocations formed during the compaction stages, and this is often accompanied by grain growth. However, the reinforcements can pin the grain boundaries and eliminate subsequent grain growth during the annealing process. The room temperature milling in ethanol/low temperature drying/single action compaction processing route produces consolidated specimens with grain sizes in the similar range as obtained by the cryomilling/high temperature-high vacuum/extrusion route. This consequently shows that the room temperature milling process adopted in the present study has the potential to be usefully applied to synthesize Al materials with nano sized grains.

Table 5. HRF measurements and standard deviation for pure aluminum and composite samples.

Reinforcement Particle, RP	RP Concentration, f_{RP} (wt%)	HR _F					
		Annealing time, t (hours)					
		0	3	6	9	17	24
None	0.0	92.48 ±0.45	87.28 ±0.80	85.24 ±0.45	82.74 ±0.56	80.70 ±0.42	78.96 ±0.91
Al ₂ O ₃	1.0	96.40 ±0.74	91.32 ±0.89	89.76 ±0.52	88.76 ±0.43	86.42 ±0.52	86.12 ±0.52
	3.0	94.72 ±0.26	83.48 ±0.49	81.50 ±0.46	81.02 ±0.90	79.48 ±0.70	80.46 ±0.82
	5.0	101.00 ±0.33	91.24 ±0.37	89.34 ±0.71	88.88 ±0.08	88.76 ±0.60	89.34 ±1.73
GNP	0.1	86.44 ±1.24	--	--	--	--	--
	0.5	87.10 ±1.02	87.48 ±0.44	87.40 ±0.91	87.04 ±0.70	86.38 ±1.39	85.92 ±0.88
	1.0	86.08 ±0.58	--	--	--	--	--

In addition to the Hardness Rockwell F measurements, nano indentation was also

conducted on selected samples to investigate the mechanical properties of the samples. Figure 55 presents the results of Young's Modulus from the nano indenter test. As we can see, the modulus of the pure aluminum sample does not change when compared to the modulus of the as-received aluminum sample. Therefore, the modulus does not change by the powder processing. By adding reinforcements such as Al₂O₃ (with the elastic Modulus about 300 GPa) and GNPs (with the elastic Modulus about 0.5-1 TPa) to the aluminum matrix, the modulus of the composite samples slightly increased compared to the pure aluminum sample.

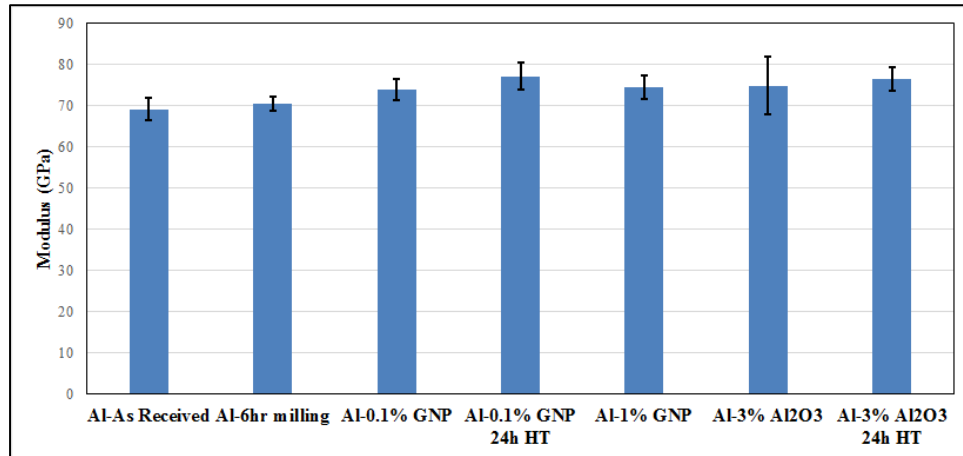


Figure 55. Young's Modulus measurements by nano indenter for selected samples.

Figure 56 shows the hardness measurements from the nano indenter test. After 6 hours of milling the hardness of pure aluminum significantly increased compared to the as-received pure aluminum sample due to the grain refinement and generation of dislocations [67]. The hardness of the Al/GNP samples decreased compared to the milled pure aluminum sample. After 24 hours of heat treatment, the hardness of the Al/GNP sample was almost constant. By adding the Al₂O₃ nano particles to the aluminum matrix, the hardness increased significantly. However, the hardness of this sample dropped from 2.5 GPa to about 1.6 GPa after 24 hours of heat treatment at 525°C.

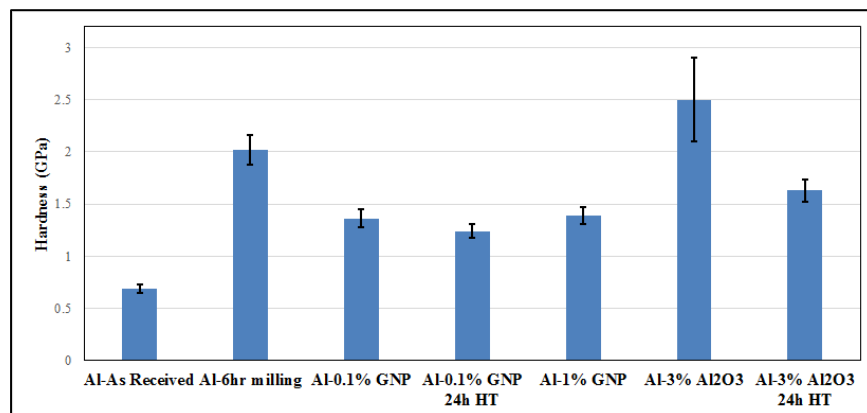


Figure 56. Hardness measurements by nano indenter for selected samples.

The hardness results from the nano indenter test and HRF were compared in Figure 57 for selected samples. Moreover, the trend of the hardness for the as-received aluminum, milled aluminum, and Al/GNP samples are the same.

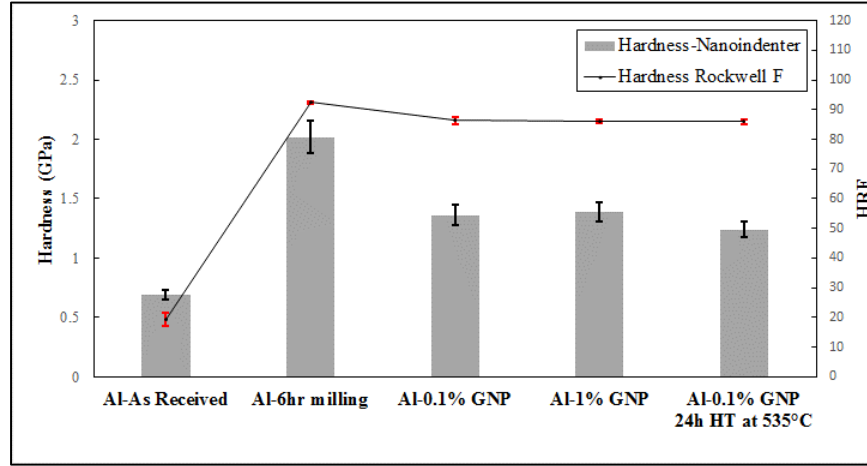


Figure 57. Hardness results from nano indenter test and Hardness Rockwell F measurements for selected samples.

The hardness results presented in Table 5 were shown in Figure 58a. Figure 58 shows the variations of a) HR_F with annealing time for NC pure Al and NC MMNC samples and b) time constant, τ , with Al_2O_3 concentration, $f_{Al_2O_3}$, which will be described later. The symbols are measured data and the solid lines represent the trend lines. With regard to material strength as a function of annealing time (Figure 58a), it shows that there is a significant difference in behavior between the GNP reinforced materials and the other materials; it is seen that GNPs increase the HR_F values much more effectively in the longer annealing time compared with Al_2O_3 . Annealing has relatively little effect on the hardness of the GNP reinforced materials, whereas there is a time-dependent drop in hardness for the pure NC Al and the Al- Al_2O_3 NC MMNCs. For the nanocrystalline Al_2O_3 reinforced nanocomposites, the average HR_F , as a function of time can be reasonably described by an exponential decay function of the form

$$HR_F = HR_{F_{FA}} + (HR_{F_{HC}} - HR_{F_{FA}}) \exp(-t / \tau), \text{ where } HR_{F_{HC}} \text{ is the hardness of the hot compacted}$$

sample, HR_{FA} is the hardness of the fully annealed sample, t is the annealing time, and τ is the time constant, respectively. From Figure 58b, it seems that τ is a function of $f_{Al_2O_3}$, and that it can also be described by an exponential decay function of the form $\tau = \tau_{pure\ Al} + (\tau_{max} - \tau_{pure\ Al}) \exp(-f_{Al_2O_3} / f_{Al_2O_3}^*)$, where τ_{max} is the value of the time constant that is asymptotically approached for high $f_{Al_2O_3}$, $\tau_{pure\ Al}$ is the time constant for unreinforced Al, and $f_{Al_2O_3}^*$ is the critical Al_2O_3 concentration, respectively.

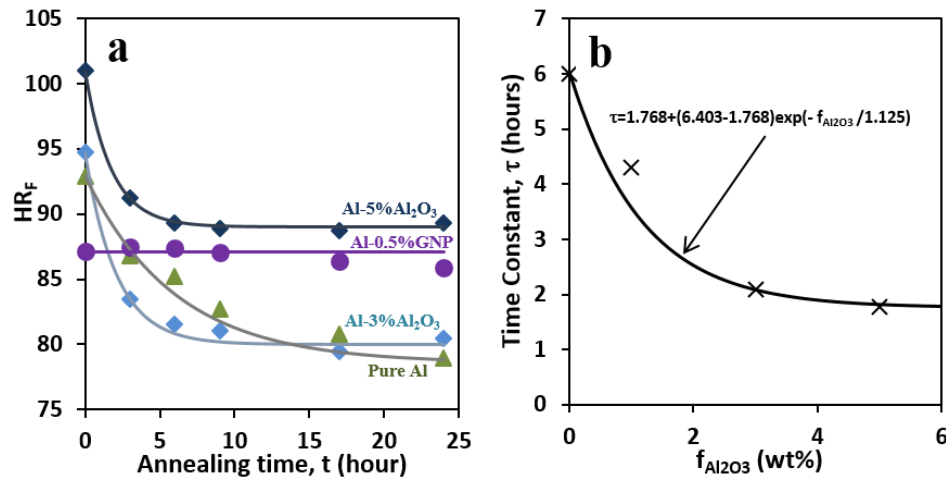


Figure 58. Variation of (a) HR_F with annealing time for NC pure aluminum and NC MMNC samples and (b) time constant, τ , with Al_2O_3 concentration.

4.3.2. Compression Test Results

Compression test results for Al matrix composites reinforced by nano alumina particles present in Figure 59. As we can see, by adding nanoparticles to the matrix the ultimate compression strength of the aluminum increased. In Al-3% Al_2O_{3np} , the strength decreased compare to the Al-1% Al_2O_{3np} and Al-5% Al_2O_{3np} .

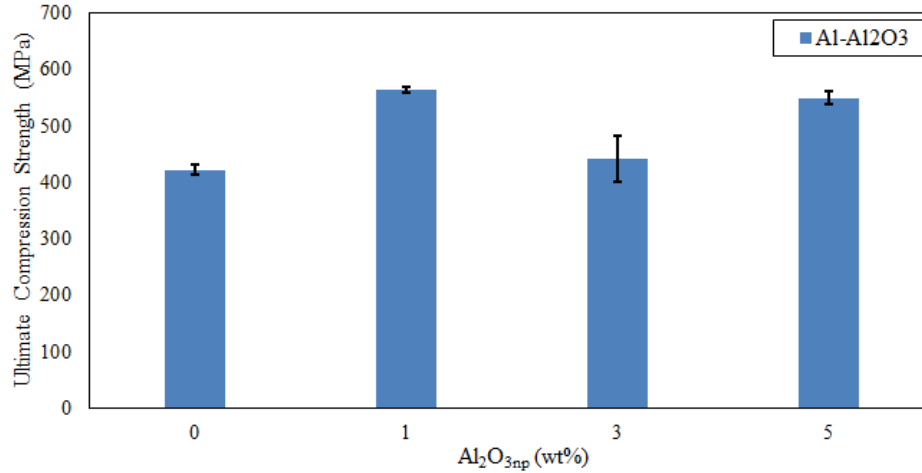


Figure 59. Ultimate compression strength (UCS) results of Al-Al₂O₃ samples.

The grain size of the matrix plays an important role on the strength of these composites. By comparing the grain size of Al-Al₂O_{3np} in Table 4, Figure 51 and Figure 54, we can see that the biggest grain size is for Al-3%Al₂O_{3np} among the Al-Al₂O_{3np} samples. In addition to the grain size, agglomeration and poor distribution of nanoparticles can affect negatively on compression strength of the samples.

Figure 60 shows the ultimate compression results of Al-GNPs samples. Adding 0.1% GNPs to the aluminum matrix increased the strength. However by adding more amount of GNP the compression strength of the composite samples decreased and the strength of Al-0.5%GNP and Al-1%GNPs are almost equal to the aluminum sample. The strength of the Al-5%GNPs drops significantly and it is less than the strength of pure aluminum. Distribution of flake shaped graphene in the aluminum matrix is more challenging compare to the alumina nanoparticles. The agglomeration of GNPs in the aluminum matrix is more possible and we have shown the agglomeration of GNPs in the Al-5%GNPs by TEM. Figure 61 clearly shows the agglomeration of GNPs in the Al-5%GNPs.

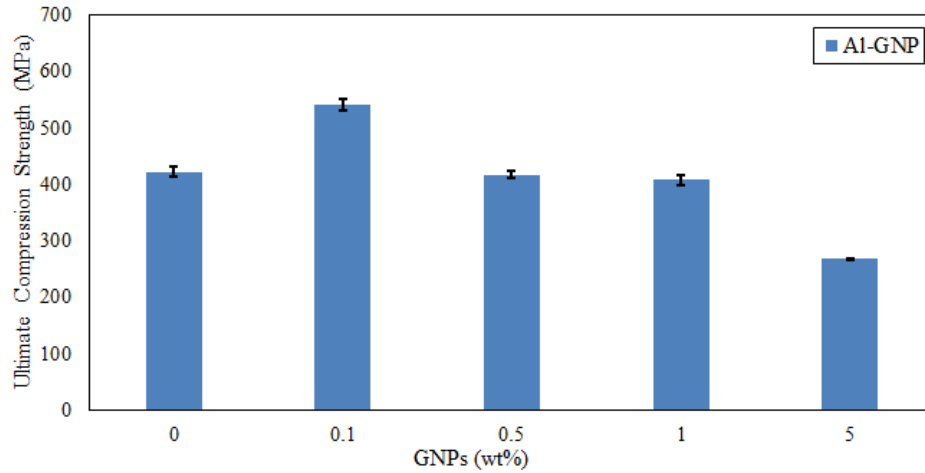


Figure 60. Ultimate compression strength (UCS) results of Al-GNPs samples.

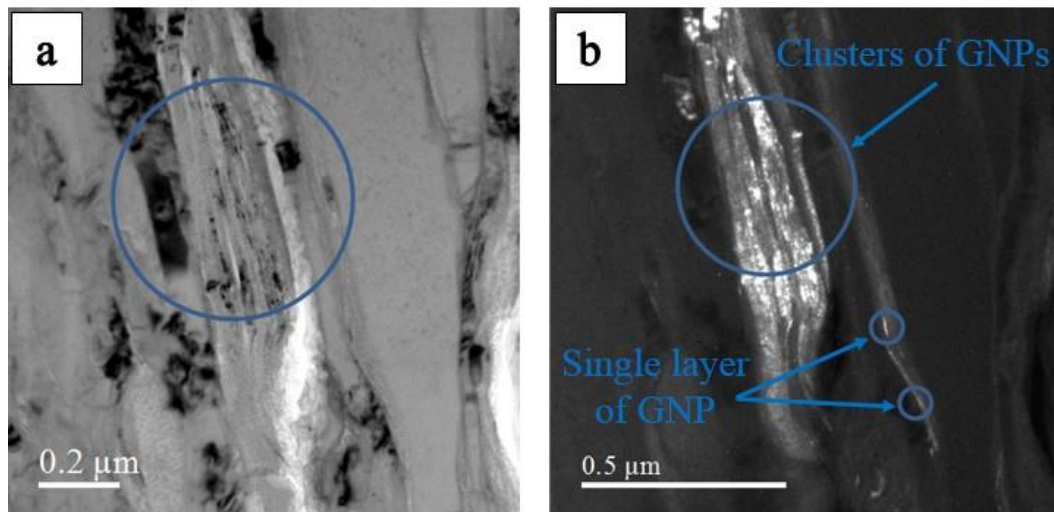


Figure 61. TEM results of clustered GNPs in the Al-5%GNPs.

In addition to the agglomeration and poor distribution of GNPs in the matrix, other issues such as poor bonding may effect on the strength of Al-GNPs samples.

4.4. Strengthening Mechanisms

The possible strengthening mechanisms for the synthesized nano composites reinforced with ceramic nano particles and/or GNPs were examined, as there still are uncertainties with this regard. Although there are some differing approaches to predict the strength of nano composites

[39, 73, 74, 75, 19, 62]. In determining the contribution (if any) of each of the various possible strengthening mechanisms, we consider the generalized model, that can be described by the following Equation (1). Note that the previous analytical prediction models for the strength increase in nano composites generally take the form of Equation (1) [39, 73, 74, 75, 19, 62].

$$\sigma_y = \sigma_{solvent} + \sum_i \Delta\sigma_i + \sqrt{\sum_j \Delta\sigma_j^2} \quad (1)$$

In Equation (1), $\Delta\sigma_i$ and $\Delta\sigma_j$ denote some unspecified individual strengthening mechanisms that must be superpositioned in arithmetic and quadratic manners, respectively. In Equation (1), it is thought that some strengthening mechanisms will add arithmetically and other will add quadratically. By considering the concepts of stress-activated and energy-activated strengthening mechanisms, the following strengthening expression has been developed [39].

$$\sigma_y = \sigma_{solvent} + \Delta\sigma_{solute} + \Delta\sigma_{ppt-coh} + \Delta\sigma_{\rho_{\perp}} + \sqrt{\Delta\sigma_{HP}^2 + \Delta\sigma_{Oro}^2} \quad (2)$$

where σ_y is the yield strength of dispersion strengthened alloys or MMNCs, $\sigma_{solvent}$ is the yield strength of the solvent (intrinsic strength of pure Al), $\Delta\sigma_{solute}$ is the increase in yield strength due to solute elements dissolved into the pure matrix materials, $\Delta\sigma_{ppt-coh}$ is the increase in yield strength due to coherent precipitation hardening, $\Delta\sigma_{\rho_{\perp}}$ is an increase in yield strength due to dislocation density, $\Delta\sigma_{HP}$ is the increase in yield strength due to grain boundaries as described by the Hall-Petch relation, and $\Delta\sigma_{Oro}$ is the increase in yield strength due to Orowan strengthening, respectively. In Equation (2), it is suggested that the strength increases from the solutes, the coherent precipitation, and the dislocations are added arithmetically, and the strength increases from the Orowan and Hall-Petch mechanisms are added quadratically. The predictions using

Equation (2) have been tested against experimental data for several types of materials strengthened by solid solutions, coherent precipitates, and incoherent precipitates over a range of grain sizes, and it was demonstrated that the prediction results were in general agreement with experimental measurements [39].

In the materials produced for this study, the reinforcements are either the same size or larger than the metallic grains and therefore must be located at grain boundaries. Since the Orowan mechanism requires that unshearable particles be located within the grains, there can be no Orowan contribution to strength in these materials ($\Delta\sigma_{Oro} = 0$). In the Al-Al₂O₃ NC MMNCs, there is no effect of alloying elements, given that there is no reaction between the matrix and the reinforcement ($\Delta\sigma_{solute} = \Delta\sigma_{ppt-coh} = 0$). Consolidated samples, since they have been both hot and cold worked, would be expected to have a higher dislocation density than the fully annealed samples. Therefore, considering $\Delta\sigma_{Oro} = 0$, $\Delta\sigma_{solute} = 0$, $\Delta\sigma_{ppt-coh} = 0$, and the Hall-Petch strengthening ($\Delta\sigma_{HP} = K_{HP} / \sqrt{D}$) [76], the yield stress of these hot compacted samples, σ_{yAl/Al_2O_3HC} , can be reduced to Equation (3) from Equation (2).

$$\sigma_{yAl/Al_2O_3HC} = \sigma_{solvent} + \Delta\sigma_{\rho_L} + \sqrt{\Delta\sigma_{HP}^2} = \sigma_{solvent} + \Delta\sigma_{\rho_L} + K_{HP} / \sqrt{D} \quad (3)$$

However, in the fully annealed samples, the dislocation density has been reduced to a minimum ($\Delta\sigma_{\rho_L} \cong 0$), then Equation (3) can be further reduced to Equation (4).

$$\sigma_{yAl/Al_2O_3FA} = \sigma_{solvent} + K_{HP} / \sqrt{D} \quad (4)$$

Since HR_F and σ_y can be considered to be analogous, the trend lines of a plot of HR_F vs. $1/\sqrt{D}$ for the hot compacted and fully annealed samples would show the characteristics of

Equations (3) and (4); the slope and the y-intercept values of these trend lines will indicate K_{HP} and $(\sigma_{solvent} + \Delta\sigma_{\rho\perp})$ for Equation (3) or $\sigma_{solvent}$ for Equation (4), respectively. If grain boundary sliding is the active mechanism, then these equations will not adequately describe the behavior and the hardness should decrease with decreasing grain size (i.e., inverse Hall-Petch strengthening). Therefore, it is feasible to characterize the strengthening mechanisms of these materials by analyzing the HR_F vs. $1/\sqrt{D}$ plots. Here, we note that, in the current research, the hardness data were used as an indicator of the strength of composites taking into consideration that the strength and hardness would correlate with each other. One can consider the strengthening mechanism in the present study as the hardening mechanism.

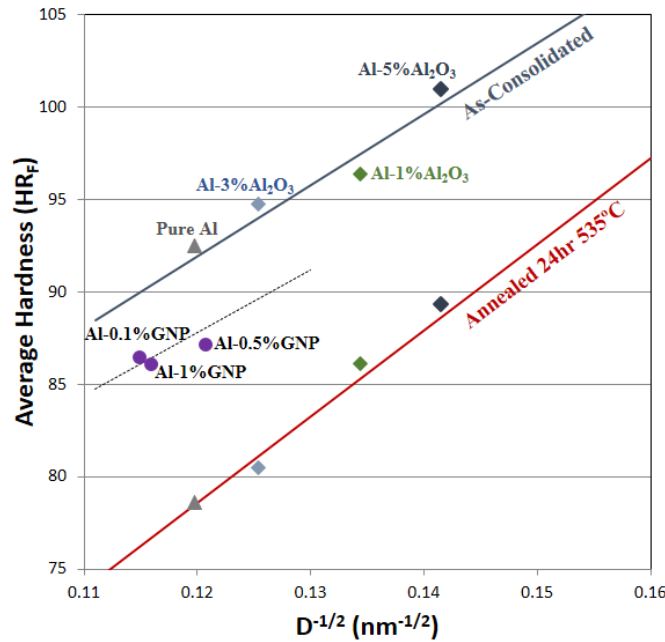


Figure 62. Variation of HR_F with inverse square root of grain size for NC pure aluminum and NC MMNCs after consolidation and after annealing heat treatments. The average hardness vs. inverse square root of grain size measurements for the Annealed Al-GNP specimens were unchanged as shown in Table 5 and thus are not included in this figure.

Figure 62 shows the variations of HR_F with inverse square root of grain size ($1/\sqrt{D}$) for NC pure Al and NC MMNCs after consolidation and after annealing heat treatments. The symbols

in the figure represent the experimentally measured hardness and the lines show the trends. The figure clearly shows that nearly parallel trends can describe the hot compacted (i.e., blue lines) and fully annealed (i.e., red lines) samples, which indicates that grain boundary sliding did not occur even though the grain sizes are considerably less than 110 nm for these samples. The higher y-intercept value of as-consolidated samples is attributed to the higher density of dislocations in these specimens ($\Delta\sigma_{\rho_d}$). In addition, given that there is no correlation between increases in strength and $f_{Al_2O_3}$, it is obvious that grain boundary strengthening is the predominant strengthening mechanism in Al-Al₂O₃ NC MMNCs. This result presents that the increased strength of Al₂O₃ particle reinforced nano composites in this study, if any, comes indirectly from the reduced grain size of the composites, not directly from the embedded particle themselves [67].

As shown in Figure 62, the Al-GNP NC MMNC hardness data (purple symbols) can be also described by a line with a similar slope to the hot compacted Al-Al₂O₃ NC MMNCs. Table 5 presents the measured HR_F values for each specimen and it is immediately evident that the Al-GNP samples had a lower hardness at the same grain size than the pure Al and the hot-compacted Al-Al₂O₃. This is presumably derived from the fact that the dislocation density in the Al-GNP specimens will be less than what is found in the Al-Al₂O₃ MMNCs. This would corroborate the findings of Wang et al. [16] who observed that, due to the relatively small thickness of the GNPs (~ 6 nm) in comparison to the thickness of the Al matrix grains (~50 to 70 nm on average), only a small percentage of the Al matrix will be affected by the presence of the GNPs, leading to lower dislocation densities overall in these materials. However, the HR_F measurements from the fully annealed samples clearly show the benefits of incorporating GNPs when the dislocations are relieved. The trend line of Al-GNP NC MMNC hardness data show a higher y-intercept value compared with the hardness of fully annealed Al-Al₂O₃ samples, which indicates that there is an

additional strengthening mechanism other than the Hall-Petch type strengthening (in addition to Equation (4)). The additional possible strengthening mechanisms in Al-GNP samples are solid solution strengthening, CTE mismatch strengthening, and load transfer strengthening. Van Horn [77] have shown that small amount of impurities in aluminum can lead to increase in strength due to solid solution strengthening. Since there is neither measurable grain growth nor softening with annealing time in the GNP reinforced material, and there is no correlation between strength and GNP concentration, the most likely mechanism is solute strengthening. The solute may be the result of impurities in the graphene, and it is unaffected by differing GNP concentrations. Identification on the types and the amounts of these probable elemental impurities in the Al/GNP composite material have not been possible in this study. In addition, CTE mismatch could be another strengthening mechanism for Al/GNP composite materials. The coefficient of thermal expansion (CTE) of aluminum and graphene at room temperature are (24×10^{-6}) and $(-8.0 \pm 0.7) \times 10^{-6} \text{ K}^{-1}$, respectively [78]. The large difference in CTE of aluminum and graphene can cause the increase in strength due to the CTE mismatch strengthening. With this, Equation (5) is proposed to describe the behavior of the Al-GNP NC MMNCs, which incorporates the solid solution, CTE mismatch and the grain boundary strengthening. Therefore, it is thought that the strengthening of nano composites reinforced by GNPs synthesized in the present work primarily controlled by the indirect impact of grain boundary pinning from GNPs, not by the Orowan mechanism as claimed by Reshad et al. [19]. The porosity of composites can also influence the mechanical properties and the concurrent application of Eq. (1), however, given that the sample hardness as a function of grain size is well described by the Hall-Petch relation, it can be inferred that the porosity has negligible influence on the measured properties of composites synthesized in this study.

$$\sigma_{yAl/GNP} = \sigma_{solvent} + \Delta\sigma_{solute} + \Delta\sigma_{p\perp} + K_{HP}/\sqrt{D} \quad (5)$$

Maung et al. [79] have produced Al-diamantane MMNCs by trap-extrusion with equiaxed grains. Plots of the conventional Hall-Petch and dislocation-accommodated boundary sliding equations against yield stress versus $1/\sqrt{D}$ graph showed a critical grain size (110 nm) below which a transition occurs from conventional Hall-Petch behavior to inverse Hall-Petch behavior. Accordingly, for grain sizes larger than 110 nm the conventional Hall-Petch equation governs the strength of the composite samples, whereas for grain sizes smaller than 110 nm the inverse Hall-Petch relation is the dominant mechanism. This transition from conventional Hall-Petch behavior to the inverse behavior was accompanied by an increase in measured ductility, which seems to corroborate the expectation that increased strength is accompanied by a decrease in ductility [80]. Although the ductility variation was not investigated in this work, and the grain morphology in this work was not equiaxed as reported in [79], there was no evidence for grain boundary sliding in either Al-Al₂O₃ or Al-GNP NC MMNCs. Therefore, it is thought that the inverse Hall-Petch behavior claimed in Al-diamantane [79] may be a result of the incorporation of diamantane and not an intrinsic behavior of pure Al. It should be noted that the strength of the Al-diamantane material decreases with increasing diamantane concentration. A recent computational/analytical model that describes load transfer strengthening in metal-matrix composites predicts that if poor bonding results between matrix and reinforcement, the yield stress will decrease with increasing reinforcement concentration [62]. The Al-diamantine NC MMNCs seem to act in a similar manner, and it is therefore likely that poor bonding, rather than grain boundary sliding, results in the reported decrease in strength.

4.5. Tribological properties

Tribological properties of selected samples were investigated by pin-on-disc wear test. Figure 63 shows the variation of coefficient of friction (COF) with normal load for pure aluminum, Al-

0.1 wt.% GNP and Al-1 wt.% GNP at constant sliding speed of 100 rpm. The results indicate that the COF decreases with increasing normal loads in all cases and follows the same decreasing trend. Furthermore, the rate of decrease in COF with normal load is significant at higher normal loads when compared to lower normal loads. The results show that the COF does not change significantly by adding 0.1 wt.% of GNP to the aluminum matrix because of insufficient amount of solid lubricant available at the contact surface. However, higher weight percentage of GNP (1 wt.%) decreased the COF of the composite sample significantly in comparison with other samples.

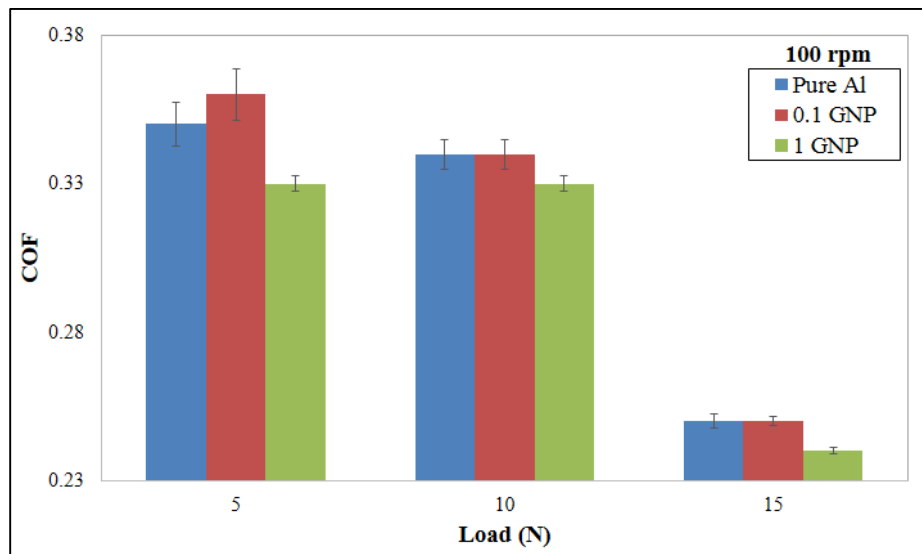


Figure 63. Variation of COF with normal load at sliding speed of 100 rpm for pure Al, Al-0.1wt.% GNP and Al-1wt.% GNP.

The variation of wear rate (weight loss) with normal load for pure aluminum, Al-0.1 wt.% GNP and Al-1 wt.% GNP at constant speed of 100 rpm is presented in Figure 64.

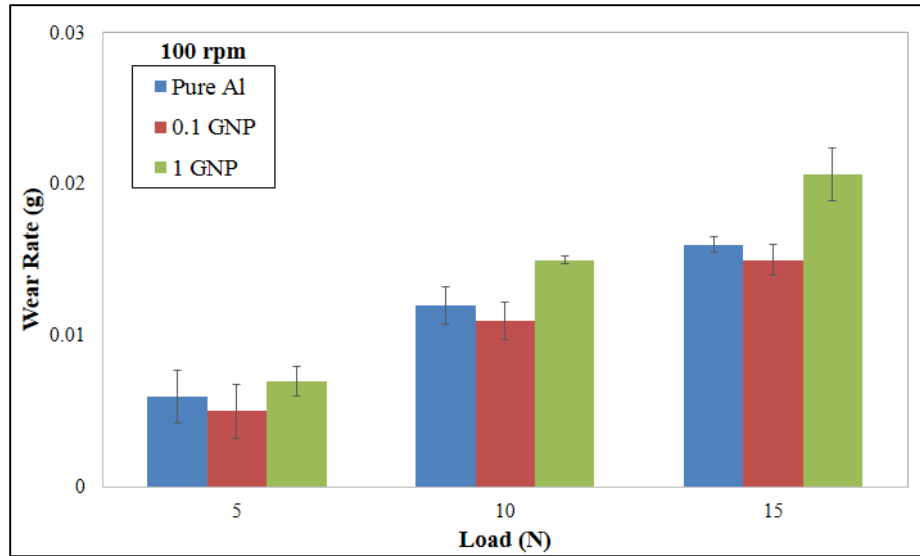


Figure 64. Variation of wear rate with normal load (N) at sliding speed of 100 rpm for pure Al, Al-0.1wt.% GNP and Al-1wt.% GNP.

As shown in the figure, the wear rate of the samples increased with increasing normal load. Also, the wear rate of Al-1wt.% GNP is more than the pure aluminum. As indicated earlier in Table 5, Al-1wt.% GNP has the lowest hardness ($86.08 \pm 0.58 \text{ HR}_F$) while the pure aluminum has the highest hardness ($92.48 \pm 0.45 \text{ HR}_F$). The hardness of the material plays an important role to explain the wear behavior of materials. Generally, the softer materials have higher wear rates compared to the harder materials [81, 82]. Further, in the literature, it is well known that there is an inverse relation between wear rate and hardness of the materials. For this reason, Al-1wt.% GNP shows the highest wear rate compared to pure aluminum sample. The reduction in hardness is believed to decrease in the load bearing capacity of the Al-1wt%GNP and consequently increased their wear rate. As regards to the variation of wear rate with normal load, in the literature, the well know Archard equation [83] demonstrated that the wear rate is directly proportional to the applied normal load. From the above discussions, it is clear that the current results are in accordance with the results presented in the literature on the variation of wear rate with normal load and hardness of the materials. As the Al-1wt%GNP has better coefficient of friction when

compared to other samples, further investigations are concentrated on this self-lubricating nanocomposites.

The worn surfaces of the pure aluminum and Al-1wt.% GNPs samples were analyzed by using optical microscope and the micrographs are presented in Figure 65. Figure 65(a) presents the optical micrograph of pure aluminum sample. The plowing marks that are formed during dry sliding conditions can be clearly seen in the figure. Figure 65(b) shows the optical micrograph of Al-1wt.% GNP sample. The formation of carbon film (black) on the worn surface of Al-1wt.% GNP sample is clearly seen. The decrease in the COF of Al-1wt.% GNPs in Figure 63 is because of formation of the carbon film on the worn surface of the sample. Formation of the carbon film causes to decrease the direct contact between the aluminum matrix and the steel disk; as a result, the COF friction of Al-1wt% GNP decreased when compared to other samples.

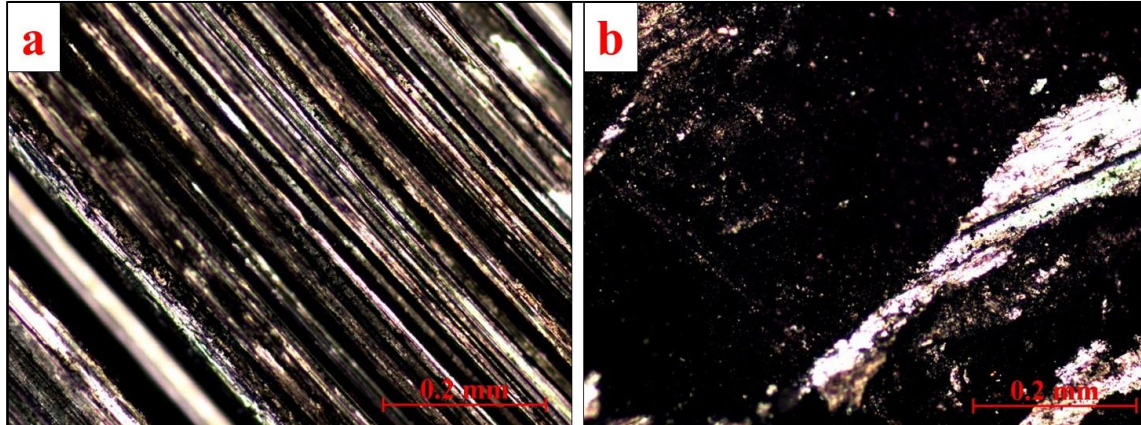


Figure 65. Optical micrographs of worn surfaces of (a) pure aluminum and (b) Al- 1wt.% GNPs.

To investigate the effect of sliding speed on the COF of Al-1wt.% GNP, experiments were conducted at various sliding speeds (50, 100 and 150 rpm) using normal loads of 5, 10 and 15 N. The variation of COF with sliding speed at different normal loads for Al-1 wt.% GNP is presented in Figure 66.

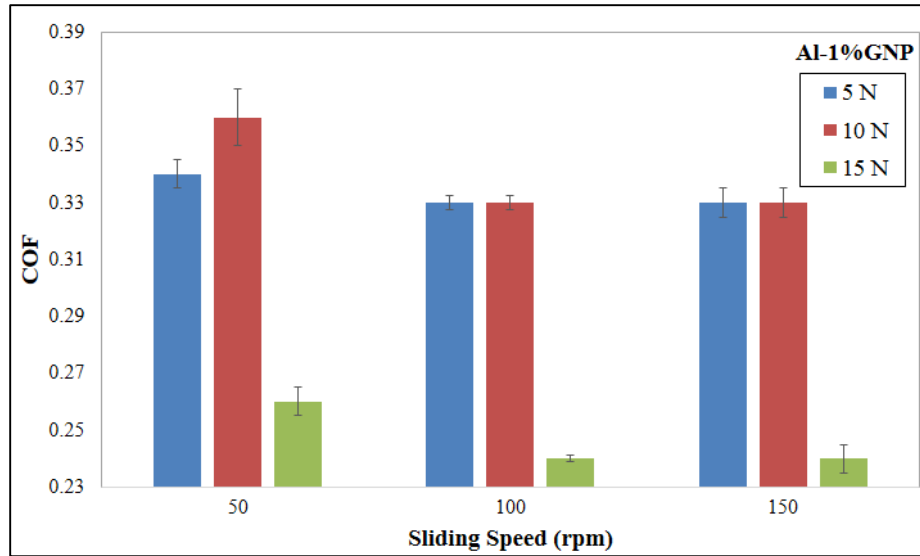


Figure 66. Variation of COF with sliding speed at different normal loads for Al-1wt.%GNP.

The COF of Al-1wt.% GNP slightly decreases with increasing sliding speeds at different normal loads. It can be seen that the influence of sliding speed on coefficient of friction is significant only at lower sliding speeds. Further, the influence of sliding speed on the coefficient of friction is less significant when compared to the effect of normal load on the coefficient of friction. At higher normal loads, more graphene is projecting out from the pin surface due to plowing between pin and disk. Consequently, the direct contact between surfaces of the sample and disc is decreased by the graphene layer and this ultimately decreased the COF. Figure 67 shows the variation of wear rate with sliding speed for Al-1wt.% GNP composite. The wear rate of Al-1wt.% GNP is much higher at 15 N load when compared to 5 and 10 N loads (Figure 64). This higher amount of wear rate has a direct influence on the COF. As the amount of graphene nanoplatelets between the contacting surfaces increases, the COF decreases owing to lubricating tendency of the graphene nanoplatelets available at the sliding interface (Figure 63).

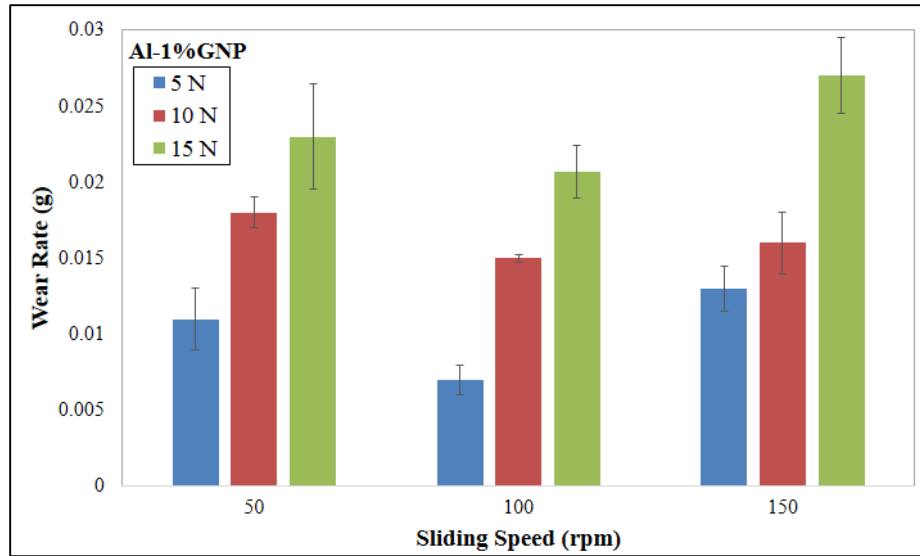


Figure 67. Variation of wear rate with sliding speed at different normal loads for Al- 1wt.% GNP.

It can be seen that the wear rate of Al-1wt.% GNP increases with increasing normal load from 5 to 15 N (Figure 67). Increasing normal load causes to increase the amount of plastic deformation on the surface and hence increase the real area of contact at the surface during the wear test [81]. As stated in the Archard equation [83], the wear rate is directly proportional to the applied normal load. The current results are in accordance with the results presented in the literature on the variation of wear rate with normal load. It can be seen in Figure 67 that the wear rate first decreases slightly and then increases with increasing the sliding speed. Although, the exact reason for this variation is unknown, it can be believed that there could be a transition from sever wear to mild wear and then back to severe wear as the sliding speed is increased. More research need to be made in this direction to understand this variation and exact reason; however, similar trends were also reported by Kozma [84] and Al-Samarai et. al [85].

The worn surfaces of the Al-1wt.%GNP samples after the wear experiments were investigated using SEM. Figure 68 shows the SEM micrographs of the worn surfaces of the Al-1wt.% GNP samples at 100X magnification at various normal loads and sliding speeds.

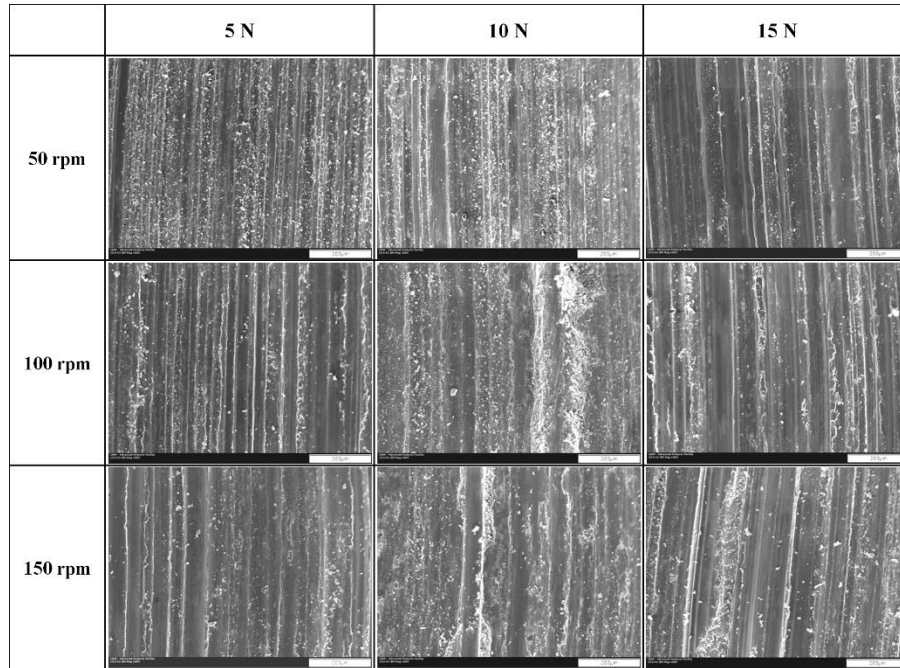


Figure 68. SEM micrograph of Al-1 Wt.% GNP at different loads and sliding speeds at magnification of 100X. (The sliding direction is from bottom to top in the SEM images).

The worn surfaces have parallel grooves in the direction of sliding with varying groove width and depth that depends on the normal load and sliding speed. These types of grooves which show on the worn surfaces in Figure 68 is due to abrasive wear during sliding conditions. More specifically, the wear mechanism in the Al-1wt.% GNP is abrasive wear even at low loads. In this current sliding situation, the contribution of adhesion could be significantly less when compared to abrasion. When self-lubrication or lubrication action is effective at the interface, basically the low sliding speed experiments represent that the tests were conducted under boundary lubricated regime [86]. At this situation, the adhesion is minimized (if not eliminated) due to the presence of lubrication effect and thus the contribution of abrasive wear mode is the key factor [86, 87].

The shallow depth and narrow width of the groove were observed on the surface of the sample during the wear test at 5 N and 50 rpm. The deepest depth and broadest width were observed on the worn surface of the sample during the wear test at 15 N and 150 rpm. For a given

normal load, the groove width and depth increased with increasing sliding speed; as a result, the highest sliding speed recorded extensive damage on the worn surfaces compared to the lowest sliding speed. Similarly, for a given sliding speed, the groove width and depth increased with increasing normal load. At higher normal loads, the damage on the worn surfaces was more considerable when compared to the lower normal loads. From the above discussions, it can be inferred that the abrasive wear of Al-1wt.% GNP increases with increasing normal loads at a constant sliding speed. In a similar manner, the abrasive wear of Al-1wt.% GNP increases with increasing sliding speeds at a constant normal load.

Figure 69 shows the SEM micrographs of the worn surfaces of pure aluminum and aluminum matrix composite reinforced by graphene nanoplatelets samples after the wear test at normal load of 5 N and sliding speed of 100 rpm.

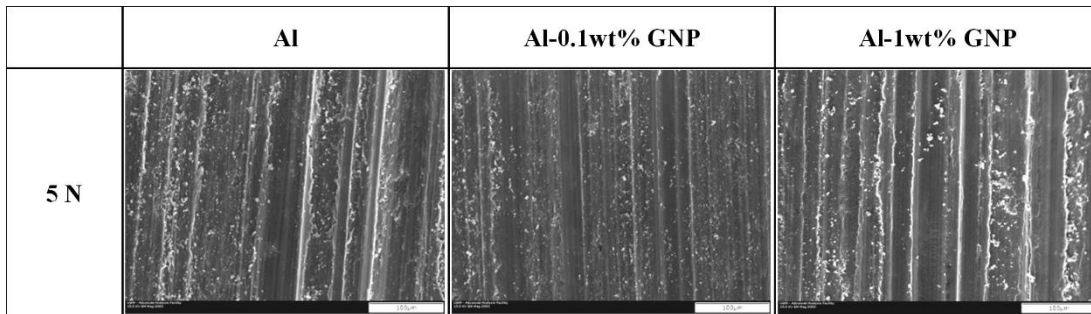


Figure 69. SEM micrographs of the worn surfaces of different samples at speed of 100 rpm and load of 5 N at magnification of 200X.

The SEM micrographs show that the Al-1wt.% GNP reinforced composite had the significant amount of damage on the worn surface and the grooves produced on the worn surface of this composite sample were the deepest when compared to the worn surfaces of aluminum sample. In addition, the SEM micrographs revealed that the worn surface of the Al-0.1wt.% GNP has the least damage compared to aluminum and Al-1wt.% GNP samples. These SEM results on surface damage correlate well with the wear data obtained in the pin-on-disk tests where the data

points in Figure 64 at normal load of 5 N showed that the wear rate is highest for Al-1wt.% GNP (hence sever damage on the pin surface as shown in Figure 69) and the wear rate is lowest for Al-0.1wt.% GNP (hence, mild damage on the pin surface as shown in Figure 69). The debris obtained after the wear test has been investigated by SEM and EDS (Figure 70).

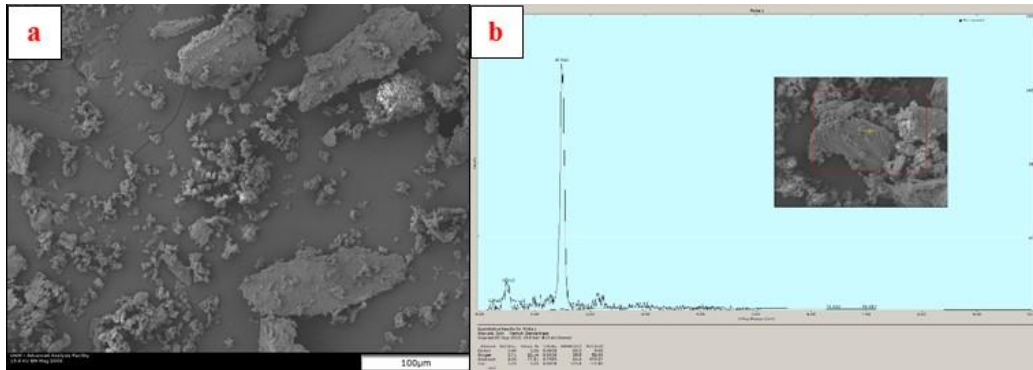


Figure 70. (a) SEM micrographs and (b) EDS results of wear debris of Al-1 Wt.% GNP sample.

Figure 70a shows the SEM micrographs of Al-1wt.% GNP at 200X magnification. The size of the debris varied in a broad range from submicron size to more than 100 microns. During the wear test the temperature at the interface of the pin and disk increases. The fresh surface of aluminum would be exposed during sliding and become active and the development of high temperature at the interface during sliding leads to formation of aluminum oxide in the wear test. The EDS result (Figure 70b) confirms the formation of oxide during wear test (Al = 77.51 atomic% and Oxygen = 22.14 atomic%).

From the above analysis, it can be seen that the Al-1wt.% GNP recorded the highest wear rate and the lowest coefficient of friction during sliding. Higher wear rate leads to higher amount of graphene particles released between the contacting surfaces during sliding. These graphene particles act as solid lubricants at the interface and enhance the lubricating effect. For this reason, the Al-1wt.% GNP composite recorded the lowest coefficient of friction. Thus, it can be inferred

that the Al-1wt.% GNP composite can be considered as a promising self-lubricating composite materials as this materials showed similar frictional and wear response as that of other self-lubricating composite materials [88].

4.6. Diametrically loaded cylinder for the study of NS MMNCs using Digital Image Correlation (DIC)

Accurately measuring the mechanical properties can be challenging, especially in small specimens typically produced when developing new materials in small quantities. For example, during the development composite materials by powder metallurgy processing, specimen sizes in the range of 10 to 25 mm are typically obtained, that are later consolidated, which make it difficult to obtain large specimens for use in tension or compression tests. The standard specimens also do not consider the multiaxial stress states that are typically present during the application of these materials to actual components and structures. Thus, it would be beneficial in the materials development process if small specimens can be used to characterize the mechanical elastic and plastic properties.

The size of the cylindrical shape samples after consolidation processing in this study is about 25 mm in diameter and 10 mm in length. As a result, developing a method to measure mechanical properties of the composite materials from the small size samples will be very helpful. We propose a hybrid method involving diametrical compression of a disk specimen together with the digital image correlation method (DIC) to study the mechanical behavior of metal matrix composites and nano-composites. DIC is an imaging method by which full-field displacements and then strains can be measured on the surface without the use of strain gages or extensometers [89]. In the 3D –DIC implementation of this method, the deformation of the samples during the mechanical test is captured by two charge-coupled device (CCD) cameras. The DIC method has

been used to characterize a variety of materials, in particular composite materials, allowing researchers to determine their deformation behavior. For example, the effect of surface scratches on the failure of laminated carbon-fiber/Epoxy composites under tensile loads have been successfully investigated by this method [90]. It has also been used to study the elastic and failure behavior of quasi-isotropic triaxially braided composites [91]. To the knowledge of the author, there has been no published studies on the use of DIC and the diametrical disk test method to analyze the mechanical behavior of MMCs and MMNCs.

4.6.1. Preliminary study

We have done some preliminary test on cylindrical specimens of unreinforced pure aluminum and aluminum reinforced with either Al_2O_3 nanoparticles or graphene nanoplatelets (GNP) were synthesized using a room temperature ethanol milling procedure. A hybrid test method using the diametrical compression disk specimen with Digital Image Correlation (DIC) is used to investigate the mechanical behavior and measure the full-field displacement in the in-plane and out-of-plane directions. Using this information and analytical methods for the diametrical disk under compression, we then extract information about the elastic and plastic behavior and correlate the results to the microstructure and failure modes in these composite cylinders.

4.6.2. Theory

Analytical solution of diametrically loaded cylinder

The analytical solution for an isotropic cylindrical disk subjected to a compressive line load (Figure 71) has been previously studied [92, 93]. The distribution of the stresses away from the contact points are given by the following relations and has previously been used to determine

the elastic modulus of rock specimens [94]. The stresses in the x-y coordinate system for an arbitrary point in the disk are:

$$\sigma_x = \frac{2P}{\pi t} \left(\frac{\cos\theta_1 \sin^2\theta_1}{r_1} + \frac{\cos\theta_2 \sin^2\theta_2}{r_2} \right) - \frac{2P}{\pi D t} \quad \text{equation (1)}$$

$$\sigma_y = \frac{2P}{\pi t} \left(\frac{\cos^3\theta_1}{r_1} + \frac{\cos^3\theta_2}{r_2} \right) - \frac{2P}{\pi D t} \quad \text{equation (2)}$$

$$\tau_{xy} = \frac{2P}{\pi t} \left(\frac{\cos^2\theta_1 \sin\theta_1}{r_1} + \frac{\cos^2\theta_2 \sin\theta_2}{r_2} \right) \quad \text{equation (3)}$$

where P is the compression load, t is the thickness of the cylinder, θ_1 and θ_2 are the angles as indicated in Figure 1, and D is the diameter of the cylinder ($D=2R$).

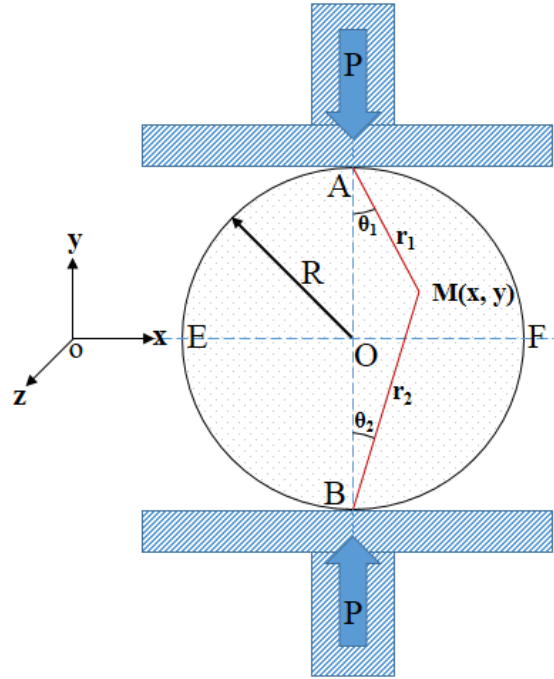


Figure 71. A cylinder shape sample subjected to compression load P.

From the triangle ABM in Figure 1, the following relations are obtained:

$$r_2^2 = r_1^2 + D^2 - 2r_1 D \cos\theta_1 \quad \text{equation (4)}$$

$$\cos\theta_2 = \frac{D^2 + r_2^2 - r_1^2}{2r_2 D} = \frac{D - r_1 \cos\theta_1}{r_2} \quad \text{equation (5)}$$

$$\sin\theta_2 = \sqrt{1 - \cos^2\theta_2} = \frac{r_1 \sin\theta_1}{r_2} \quad \text{equation (6)}$$

Substituting equations 4, 5, and 6 into equations 1, 2, and 3 we obtain the following equations:

$$\sigma_x = \frac{2P}{\pi t} \left[\frac{\cos\theta_1 \sin^2\theta_1}{r_1} + \frac{(D-r_1\cos\theta_1)r_1^2\sin^2\theta_1}{(r_1^2+D^2-2Dr_1\cos\theta_1)^2} - \frac{1}{D} \right] \quad \text{equation (7)}$$

$$\sigma_y = \frac{2P}{\pi t} \left[\frac{\cos^3\theta_1}{r_1} + \frac{(D-r_1\cos\theta_1)^3}{(r_1^2+D^2-2Dr_1\cos\theta_1)^2} - \frac{1}{D} \right] \quad \text{equation (8)}$$

$$\tau_{xy} = \frac{2P}{\pi t} \left[\frac{\sin\theta_1 \cos^2\theta_1}{r_1} - \frac{(D-r_1\cos\theta_1)^2 r_1 \sin\theta_1}{(r_1^2+D^2-2Dr_1\cos\theta_1)^2} \right] \quad \text{equation (9)}$$

The relationship between the rectangular coordinate (x,y) and the polar coordinate (r₁, θ₁) of point M is as follows:

$$\begin{cases} x = r_1 \sin\theta_1 \\ y = \frac{D}{2} - r_1 \cos\theta_1 \end{cases} \Rightarrow \begin{cases} r_1 = \sqrt{\left(\frac{D}{2}-y\right)^2 + x^2} \\ \cos\theta_1 = \frac{\left(\frac{D}{2}-y\right)}{r_1}, \quad \sin\theta_1 = \frac{x}{r_1} \end{cases} \quad \text{equation (10)}$$

By substituting equations 10 into equations 7, 8, and 9, we have:

$$\sigma_x = \frac{2P}{\pi t} \left[\frac{\left(\left(\frac{D}{2}-y\right)x^2\right)}{\left(\left(\left(\frac{D}{2}-y\right)^2 + x^2\right)^2\right)} + \frac{\left(\left(\frac{D}{2}+y\right)x^2\right)}{\left(\left(\left(\frac{D}{2}+y\right)^2 + x^2\right)^2\right)} - \frac{1}{D} \right] \quad \text{equation (11)}$$

$$\sigma_y = \frac{2P}{\pi t} \left[\frac{\left(\left(\frac{D}{2}-y\right)^3\right)}{\left(\left(\left(\frac{D}{2}-y\right)^2 + x^2\right)^2\right)} + \frac{\left(\left(\frac{D}{2}+y\right)^3\right)}{\left(\left(\left(\frac{D}{2}+y\right)^2 + x^2\right)^2\right)} - \frac{1}{D} \right] \quad \text{equation (12)}$$

$$\tau_{xy} = \frac{2P}{\pi t} \left[\frac{\left(\left(\frac{D}{2}-y\right)^2 x\right)}{\left(\left(\left(\frac{D}{2}-y\right)^2 + x^2\right)^2\right)} - \frac{\left(\left(\frac{D}{2}+y\right)^2 x\right)}{\left(\left(\left(\frac{D}{2}+y\right)^2 + x^2\right)^2\right)} - \frac{1}{D} \right] \quad \text{equation (13)}$$

The modulus can be obtained from the analytical stresses and the measured gage strains from the DIC results. For the tensile modulus (y=0), the stress distribution at the center of the disk must be accounted for since the compressive stress, S_y , exerts tensile strains due to Poisson's effect. Similarly for the compressive modulus (when x=0), the tensile stress exerts an

additional strain (to a lesser level than for tension) that is accounted for in the expressions below.

E_t and E_c are the tensile and compressive moduli respectively and are expressed as follows:

$$E_t = \frac{1}{e_{gx} L} \int_0^L (-S_x + \nu S_y) dx \quad \text{equation (14)}$$

$$E_c = \frac{1}{e_{gy} L} \int_0^L (S_y - \nu S_x) dy \quad \text{equation (15)}$$

Where L is the half-length of the gage length at the center of the disk and ν is the Poisson ratio (assumed at 0.33 for all disks). e_{gx} and e_{gy} are the gage strains in the x and y-directions measured from the DIC over a gage section of length $2L$. The gage length L was approximately 5 mm and evaluated in the center of the disk.

Diametrically loaded cylinder experiments using DIC

The elastic mechanical properties of the cylindrical specimens were determined by the diametrical compression method. The compression load was applied on the side of the cylinder as shown schematically in Figure 72. An electromechanical universal test machine was used for testing the disk shaped specimens. Digital image correlation (DIC) was used to capture the deformations on the flat ends of the cylindrical specimen.

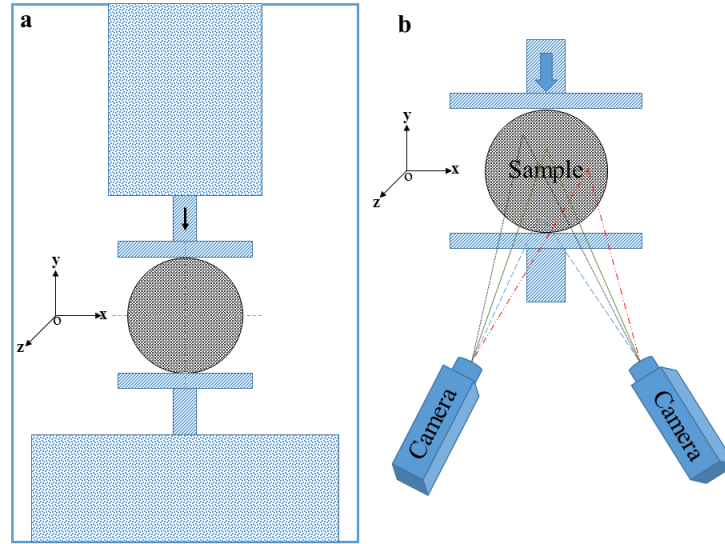


Figure 72. Schematic of diametrically loaded cylinder and location of the cameras.

The optical measurements were performed using a 3D DIC system (Q-400; Dantec Dynamics GmbH, Skovlunde, Denmark and Ulm, Germany). Prior to testing, a white flat spray paint is used to cover the surface of the specimens. This is followed with application of a speckle pattern using black paint to create random small drops. A resolution of 5 megapixels is used for the CCD cameras together with a 35 mm lens on each camera. Figure 72 shows the test specimen in the loading frame with the 2 CCD cameras used for 3D digital image correlation. Prior to testing of the MMNC specimens, a series of calibration steps are performed on a calibration plate. Calibration is used for determination of the imaging parameters (intrinsic and extrinsic) of each of the cameras in addition to the position of the cameras relative to the overall coordinate system. An acceptable calibration was considered if the residuum was less than 0.3 pixels. An output signal from the loading system for the load and displacement is synchronized with the image correlation system so that each frame is correlated to the actual loads applied to the specimen at that point. The deformations were recorded during each test at a frequency of 0.5 Hz. The initial image in the unloaded state was used for the reference for all the subsequent

images. At the post processing stage, a grid size of 12 pixels and a facet size of 17 pixels were used for the evaluation.

4.6.3. Results

Using the inverse methodology, we were able to obtain the modulus of selected samples in both directions to a maximum of error of 9 %. Note the correlation in the displacement field is primarily away from the loading points. Thus, any analysis of the displacement fields for extraction of elastic material properties did not use the results from near the loading points. The modulus results summarized in Table 6. As we can see, the modulus of the composite samples are less compare to the pure aluminum samples. In addition, the results from the DIC method are not close to the modulus of elasticity results from nanoindentation.

Table 6. Summary of modulus from diametrical disk compression test

	Pure Al	Al-5%Al ₂ O ₃	Al-1%GNP	Al-5%GNP
Modulus – Compression GPa (Msi)¹	66.1 (9.583)	61.9 (8.975)	62.9 (9.126)	58.6 (8.506)
Modulus – Tension GPa (Msi)¹	54.4 (7.89)	50.3 (7.302)	52.0 (7.548)	52.6 (7.64)

The DIC results of shear strain for the samples are shown in Figure 73. The shear strains in the elastic region (left column) and before failure (right column) are shown in Figure 73 for a) pure aluminum b) Al-5%Al₂O₃, and c) Al-5%GNP. The behavior of the pure aluminum and the Al-5%Al₂O₃ sample was investigated in more detail by DIC in this study. Figure 74 shows the graph of the stress versus shear strain of pure aluminum and the Al-5% Al₂O₃ samples. Stresses reported in the figures are also normalized with respect to the average stress at the center of the disk. This average stress, S_o is defined here as the load, P , divided by the total cross-sectional area, A , at the center of the disk, or $A = Dt = 403.86 \text{ mm}^2 (0.626 \text{ inch}^2)$, where t is the disk thickness and D is the disk diameter.

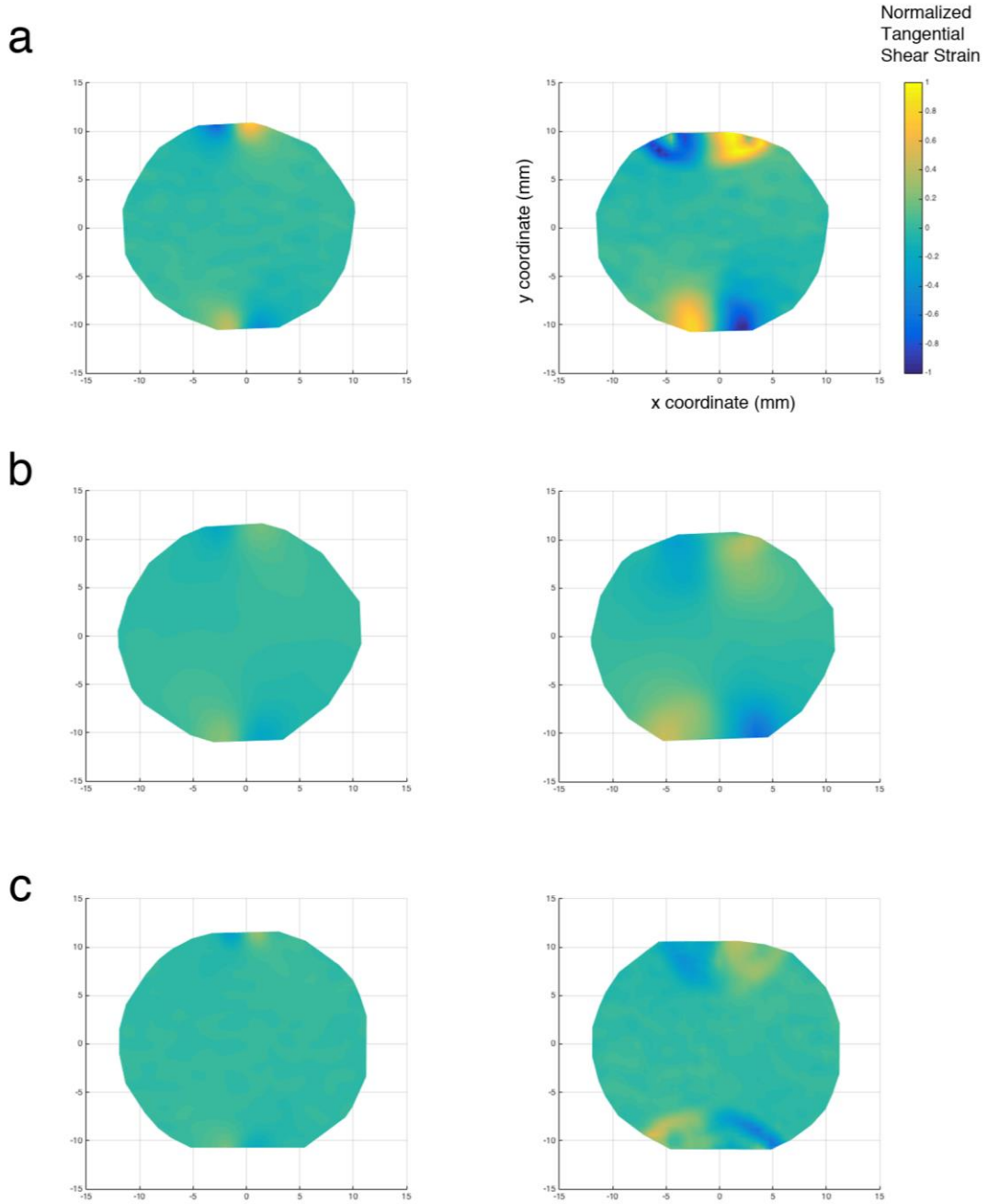


Figure 73. DIC results of shear strain in the elastic region (left column) and before failure (right column) for a) pure aluminum, b) Al-5%Al₂O₃, and c) Al-5%GNP.

The shear strain behavior of these samples followed the same trend of axial strain behavior. The presence of dispersed Al₂O₃ nanoparticles at the grain boundaries can act to pin the aluminum grains and prevent them from shearing. As a result, Al-5%Al₂O₃ shows less shear strain at failure

when compared to the pure aluminum sample. This can be seen in the failure sites near the loading pins in Figure 74. In this figure, a point strain evaluation is taken which accounts for the increased scatter in the measurements.

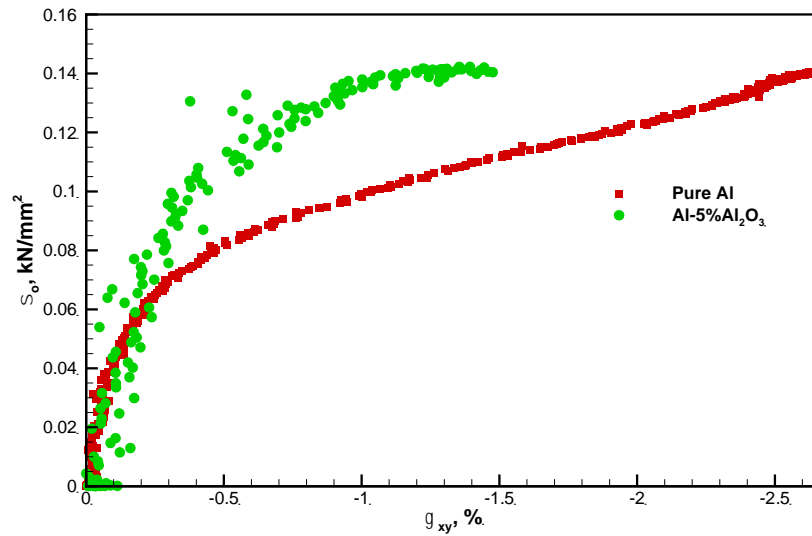


Figure 74. Stress versus shear strain from DIC results for pure aluminum and Al-5%Al₂O₃.

However, the behavior of the pure aluminum and Al-5%Al₂O₃ sample is different in the transverse (z) direction. Figure 7 shows the graph of average stress versus transverse strain from the DIC results for pure aluminum and Al-5%Al₂O₃ samples.

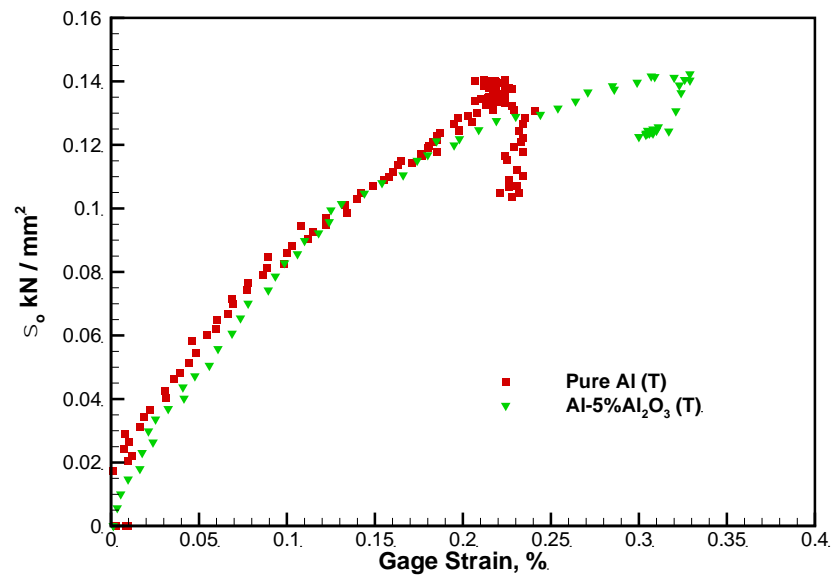


Figure 75. Stress versus transverse strain from DIC results for pure aluminum and Al-5%Al₂O₃.

The graph shows that the transverse strain for the pure aluminum sample is less than that of the Al-5%Al₂O₃ sample. Note that in this figure a gage length of approximately 5mm is used to evaluate the strain. At the maximum values, the drop in the stress is due to failure near the loading zone. The different strains observed may be due to the presence of porosity in the Al-5%Al₂O₃ samples. As noted in, the relative density of the Al-5%Al₂O₃ is only 93.5%, compared to 98.8% for pure Al. This porosity is likely to be concentrated at the regions between the aluminum flakes that were not completely bonded during the consolidation process. This is shown schematically in Figure 76, where the transverse strain is perpendicular to the elongated faces of the aluminum matrix.

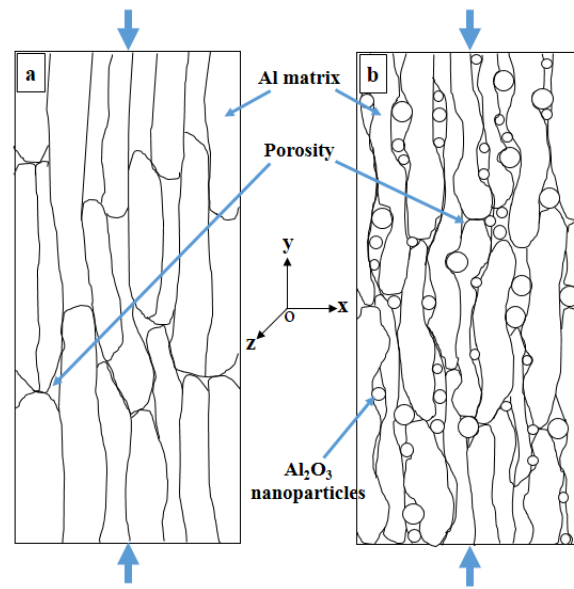


Figure 76. Schematic of microstructure interactions of a) Al and b) Al-5%Al₂O₃.

Compression load in “y” direction causes a tensile strain in “x” direction in all of the samples. Due to the existence of more porosities in the Al-5%Al₂O₃ sample, the aluminum matrix has more space for deformation in “x” direction. As a result, there is more transverse strain in the Al-5%Al₂O₃ sample compare to the pure aluminum due to the lower tensile modulus.

4.6.4. *Limitations*

The current approach of using this method on MMNC is unable to achieve a tensile failure in the center of the specimen. A flat loading surface may help yield the required stresses in the center of the specimen to obtain tensile yield and failure behavior. Also while the disparity is seen in the tensile and compressive moduli obtained, it is important to note that the analytical solution assumes an isotropic medium. Thus, to further develop this method an anisotropic model may be necessary to achieve more accurate assessment of the material's anisotropy. The Poisson ratio may also be obtained using over-deterministic approaches from the full-field data but this was not investigated in this present study.

Chapter 5.

Summary and Conclusions

5. Summary and Conclusions

In this study, powder metallurgy methods were used to produce nano-crystalline pure aluminum and aluminum alloy matrix composites. Two different types of reinforcements including graphene nanoplatelets and alumina particles with different sizes have used. The attritor mill was used for 6 hours to mill the powders at room temperature in the presence of ethanol. The consolidation of the milled powders was conducted in two steps including single action cold compaction and single action hot compaction. The average grain size of the composite powders after milling was measured by using Scherrer equation from the XRD results. The average grain size of the consolidated samples was also measured by the same method as well as the microstructure by TEM. The density of the consolidated samples was measured by Archimedes' method. The mechanical properties of the consolidated samples were measured by hardness Rockwell F, nanoindentation, and compression test method. The possible activation of strengthening mechanisms for $\text{Al}_2\text{O}_{3\text{np}}$ and GNPs reinforced Al nano composites synthesized by the above mentioned method have been investigated. We have considered that the strengthening mechanism can be applied to the hardness (i.e., analogous to the strength) of the synthesized samples. Tribological properties of the selected samples were investigated by pin-on-disk wear test. The results are as follows:

- $\text{Al}_2\text{O}_{3\text{np}}$ and GNP reinforced Al nanocomposites were synthesized using a room temperature milling in ethanol/low temperature drying/single action compaction method, this processing sequence is a much simpler processing route compared with typical cryomilling and subsequent degassing. The consolidated specimens produced grain sizes in the range of (50 nm to 80 nm) those obtainable by the cryomilling/high temperature-high vacuum drying/extrusion route. Annealing at 535°C did not increase the average

grain sizes for Al-Al₂O_{3np} and Al-GNP samples. This attritor milling powder processing technique at room temperature appears to be broadly applicable to the synthesis of nano crystalline materials with enhanced mechanical properties.

- The average grain size of the powders decreased as a result of 6 hours of attritor milling in ethanol atmosphere from about 130 nm to about 50 nm.
- Types of the reinforcements, shape of the reinforcements, size of the reinforcements and concentration of the reinforcements do not have a significant measurable effect on the average grain size of the powders after 6 hours milling.
- After consolidation processing there is grain growth on the samples. This grain growth depends on the types and shape of reinforcement.
- Since the morphology of the powders changes after milling, the compressibility of the powders is different compared to as-received powders. After 6 hours of milling and consolidation processing the relative density of the pure aluminum is lower compared to as-received powders.
- The types of the reinforcement can change the compressibility of the samples. Graphene nanoplatelets can improve the compressibility of the composite powders. The relative density of the composite samples reinforced by graphene is close to 100%.
- The relative densities of the aluminum matrix composites reinforced by alumina nano particles are between 85%-95%.
- After 6 hours of milling the HRF of the pure aluminum samples improve significantly from 20 to about 92.
- In Al-Al₂O₃ NC MMNCs processed in this study, grain boundary strengthening appears to be the predominant strengthening mechanism. The strengthening is primarily accounted

for by the indirect effect of reinforcement grain boundary pinning during processing. Therefore, controlling the grain size would be the major factor for increased strength and hardness of the Al-Al₂O₃ samples.

- Al-GNP samples showed in general higher grain size compared with Al-Al₂O₃ samples. In Al-GNP NC MMNCs, grain boundary strengthening is considered to be the predominant mechanism, while solid solution strengthening from impurities in the GNP and CTE mismatch strengthening may also contribute to the strength. The existence of such impurities is inferred from the increased y-intercept of a Hall-Petch plot, however they were not detectable by either XRD or EDS analysis. Therefore, grain size appears to be the major factor which controls the hardness/strength of the Al nanocomposites reinforced by GNPs.
- The COF decreases from 0.35 to 0.25 for the pure aluminum, and from 0.33 to 0.23 for the Al-1%GNP sample with increasing the normal load at a constant sliding speed.
- Addition of 0.1 wt.% of GNP to the aluminum matrix did not change the COF significantly when compared to the pure aluminum sample. However, increasing amount of GNP to 1wt.% decreased the COF from 0.33 to 0.23 compared to the pure aluminum.
- Among the three materials, namely, aluminum, Al-0.1wt.% GNP composite and Al-1wt.% GNP composite, the Al-1wt.% GNP composite showed the lowest COF.
- The wear rate of the pure aluminum and aluminum matrix nanocomposites reinforced by GNP increased with increasing the normal load.
- Among the three materials, namely, aluminum, Al-0.1wt.% GNP composite and Al-1wt.% GNP composite, the Al-1wt.% GNP composite indicated the highest wear rate.

- The wear rate of Al-1wt.% GNP is higher at higher normal loads when compared to lower normal loads. Due to higher wear rate at higher normal load, more graphene is projected out to the interface. As a result, the COF of the Al-1wt.% GNP is lower at higher normal load.
- The SEM investigation of the worn surfaces had shown that abrasive wear was the main wear mechanism in these composites.
- The lowest coefficient of friction of the Al-1wt.% GNP is attributed to self-lubricating behavior of the composites.
- The diametrical cylinder in compression test coupled with the digital image correlation method can be used to characterize the elastic and failure properties of MMNC materials.
- The inverse approach used to predict stiffness is an effective method to obtain the material elastic properties.

Chapter 6.

References

6. References

- [1] D. Kopeliovich, "<http://www.substech.com/>," [Online].
- [2] C. Suryanarayana, "Mechanical alloying and milling," *Progress in Materials Science*, vol. 46, pp. 1-184, 2001.
- [3] E. Hall, "The Deformation and Ageing of Mild Steel: III Discussion of Results," *Proceedings of the Physical Society*, vol. 64, pp. 747-753, 1951.
- [4] N. Petch, "The Cleavage Strength of Polycrystals," *Journal of Iron and Steel Institute*, vol. 173, pp. 25-28, 1953.
- [5] M. Tabandeh Khorshid, S. Jenabali Jahromi and M. Moshksar, "Mechanical properties of tri-modal Al matrix composites reinforced by nano- and submicron-sized Al₂O₃ particulates developed by wet attrition milling and hot extrusion," *Materials and Design*, vol. 31, pp. 3880-3884, 2010.
- [6] J. Wei, Z. Li and F. Han, "Thermal Mismatch Dislocations in Macroscopic Graphite Particle-Reinforced Metal Matrix Composites Studied by Internal Friction," *physica status solidi (a)*, vol. 191, pp. 125-136, 2002.
- [7] L. Kollo, M. Leparoux, C. Bradbury, C. Jäggi, E. Carreno-Morelli and M. Rodríguez-Arbaizar, "Investigation of planetary milling for nano-silicon carbide reinforced aluminium metal matrix composites," *Journal of Alloys and Compounds*, vol. 489, pp. 394-400, 2010.

- [8] E. Rodrigues de Araujo, M. Sampaio de Souza, F. Filho, C. Gonzalez and O. De Araújo Filho, "Preparation of Metal Matrix Aluminum Alloys Composites Reinforced by Silicon Nitride and Aluminum Nitride through Powder Metallurgy Techniques," *Materials Science Forum*, Vols. 727-728, pp. 259-262, 2012.
- [9] C. Hofmeister, B. Yao, Y. Sohn, T. Delahanty, M. Van den Bergh and K. Cho, "Composition and structure of nitrogen-containing dispersoids in trimodal aluminum metal–matrix composites," *Journal of Materials Science*, vol. 45, pp. 4871-4876, 2010.
- [10] R. Derakhshandeh Haghighi, S. Jenabali Jahromi, A. Moresedgh and M. Tabandeh-Khorshid, "A Comparison Between ECAP and Conventional Extrusion for Consolidation of Aluminum Metal Matrix Composite," *Journal of Materials Engineering and Performance*, vol. 21, pp. 1885-1892, 2012.
- [11] Y. Li, Y. Zhao, W. Liu, Z. Zhang, R. Vogt, E. Lavernia and J. Schoenung, "Deformation twinning in boron carbide particles within nanostructured Al 5083/B4C metal matrix composites," *Philosophical Magazine*, vol. 90, pp. 783-792, 2010.
- [12] A. Knowles, X. Jiang, M. Galano and F. Audebert, "Microstructure and mechanical properties of 6061 Al alloy based composites with SiC nanoparticles," *Journal of Alloys and Compounds*, p. <http://dx.doi.org/10.1016/j.jallcom.2014.01.134>, 2014.
- [13] K. Kondoh, J. Umeda and R. Watanabe, "Cavitation resistance of powder metallurgy aluminum matrix composite with AlN dispersoids," *Materials Science and Engineering A*, vol. 499, pp. 440-444, 2009.

- [14] N. Saheb, A. Khalil, A. Hakeem, T. Laoui and N. Al-Aqeeli, "Carbon Nanotube reinforced Al6061 AND Al2124 nanocomposites," in *ECCM15-15TH European Conference on Composite Materials*, Venice, Italy, 2012.
- [15] A. Esawi, K. Morsi, A. Sayed, M. Taher and S. Lanka, "The influence of carbon nanotube (CNT) morphology and diameter on the processing and properties of CNT-reinforced aluminium composites," *Composites: Part A*, vol. 42, p. 234–243, 2011.
- [16] J. Wang, Z. Li, G. Fan, H. Pan, Z. Chen and D. Zhang, "Reinforcement with graphene nanosheets in aluminum matrix composites," *Scripta Materialia*, vol. 66, pp. 594-597, 2012.
- [17] S. Bartolucci, J. Paras, M. Rafiee, J. Rafiee, S. Lee, D. Kapoor and N. Koratkar, "Graphene–aluminum nanocomposites," *Materials Science and Engineering A*, vol. 528, pp. 7933-7937, 2011.
- [18] M. Bastwros, G.-Y. Kim, C. Zhu, K. Zhang, S. Wang, X. Tang and X. Wang, "Effect of ball milling on graphene reinforced Al6061 composite fabricated by semi-solid sintering," *Composites: Part B*, vol. 60, pp. 111-118, 2014.
- [19] M. Rashad, F. Pan, A. Tang and M. Asif, "Effect of Graphene Nanoplatelets addition on mechanical properties of pure aluminum using a semi-powder method," *Progress in Natural Science: Materials International*, vol. 24, pp. 101-108, 2014.
- [20] R. Pérez-Bustamante, D. Bolaños-Morales, J. Bonilla-Martínez, I. Estrada-Guel and R. Martínez-Sánchez, "Microstructural and hardness behavior of graphene-

- nanoplatelets/aluminum composites synthesized by mechanical alloying," *Journal of Alloys and Compounds*, p. <http://dx.doi.org/10.1016/j.jallcom.2014.01.225>, 2014.
- [21] J. Slonczewski and P. Weiss, "Band structure of graphite," *Physical Review*, vol. 109, pp. 272-279, 1958.
- [22] V. Singh, D. Joung, L. Zhai and S. Das, "Graphene based materials: Past, present and future," *Progress in Materials Science*, vol. 56, pp. 1178-1271, 2011.
- [23] Y. Zhu, S. Murali, W. Cai, X. Li, J. Suk, J. Potts and R. Ruoff, "Graphene and Graphene Oxide: Synthesis, Properties, and Applications," *Advanced Materials*, vol. 22, pp. 1-19, 2010.
- [24] W. Choi, I. Lahiri, R. Seelaboyina and Y. Kang, "Synthesis of Graphene and Its Applications: A Review," *Critical Reviews in Solid State and Material Sciences*, vol. 35, pp. 52-71, 2010.
- [25] D. Yoon, Y.-W. Son and H. Cheong, "Negative Thermal Expansion Coefficient of Graphene Measured by Raman Spectroscopy," *Nano Letters*, vol. 11, pp. 3227-3231, 2011.
- [26] C. Lee, X. Wei, J. Kysar and J. Hone, "Measurement of the elastic properties and intrinsic strength of monolayer graphene," *Science*, vol. 321, pp. 385-388, 2008.
- [27] K. Novoselov, A. Geim, S. Morozov, D. Jiang, Y. Zhang, S. Dubonos, I. Grigorieva and A. Firsov, "Electric Field Effect in Atomically Thin Carbon Films," *Science*, vol. 306, pp. 666-669, 2004.

- [28] K. Novoselov, D. Jiang, F. Schedin, T. Booth, V. Khotkevich, S. Morozov and A. Geim, "Two-dimensional atomic crystals," *Proceedings of the National Academy of Sciences of the United States of America*, vol. 102, pp. 10451-10453, 2005.
- [29] T. He, J. Li, L. Wang, J. Zhu and W. Jiang, "Preparation and Consolidation of Alumina/Graphene Composite Powders," *Materials Transactions*, vol. 50, pp. 749-751, 2009.
- [30] W. Zhao, M. Fang, F. Wu, H. Wu, L. Wang and G. Che, "Preparation of graphene by exfoliation of graphite using wet ball milling," *Journal of Materials Chemistry*, vol. 20, pp. 5817-5819, 2010.
- [31] Q. Li, A. Viereckl, C. A. Rottmair and R. F. Singer, "Improved processing of carbon nanotube/magnesium alloy composites," *Composites Science and Technology*, vol. 69, pp. 1193-1199, 2009.
- [32] L.-Y. Chen, H. Konishi, A. Fehrenbacher, C. Ma, J.-Q. Xu, H. Choi, H.-F. Xu, F. Pfefferkorn and X.-C. Li, "Novel nanoprocessing route for bulk graphene nanoplatelets reinforced metal matrix nanocomposites," *Scripta Materialia*, vol. 67, pp. 29-32, 2012.
- [33] A. Fadavi Boostani, S. Tahamtan, Z. Jiang, D. Wei, S. Yazdani, R. Azari Khosroshahi, R. Taherzadeh Mousavian, J. Xub, X. Zhang and D. Gong, "Enhanced tensile properties of aluminium matrix composites reinforced with graphene encapsulated SiC nanoparticles," *Composites: Part A*, vol. 68, pp. 155-163, 2015.

- [34] M. Rashad, F. Pan, A. Tang, M. Asif, S. Hussain, J. Gou and J. Mao, "Improved strength and ductility of magnesium with addition of aluminum and graphene nanoplatelets (Al + GNPs) using semi powder metallurgy method," *Journal of Industrial and Engineering Chemistry*, p. <http://dx.doi.org/10.1016/j.jiec.2014.08.024>, 2014.
- [35] S. Shin, H. Choi, J. Shin and D. Bae, "Strengthening behavior of few-layered graphene/aluminum composites," *Carbon*, vol. 82, pp. 143-151, 2015.
- [36] D. Graf, F. Molitor, K. Ensslin and C. Stampfer, "Spatially Resolved Raman Spectroscopy of Single- and Few-Layer Graphene," *Nano Letters*, vol. 7, pp. 238-242, 2007.
- [37] M. Rafiee, J. Rafiee, Z.-Z. Yu and N. Koratkar, "Buckling resistant graphene nanocomposites," *Applied Physics Letters*, vol. 95, pp. 223103-1-3, 2009.
- [38] D. Zheng, G. Tang, H.-B. Zhang, Z.-Z. Yu, F. Yavari, N. Koratkar, S.-H. Lim and M.-W. Lee, "In situ thermal reduction of graphene oxide for high electrical conductivity and low percolation threshold in polyamide 6 nanocomposites," *Composites Science and Technology*, vol. 72, pp. 284-289, 2012.
- [39] J. Ferguson, B. Schultz, D. Venugopalan, H. Lopez, P. Rohatgi, K. Cho and C.-S. Kim, "On the superposition of strengthening mechanisms in dispersion strengthened alloys and metal-matrix nanocomposites: Considerations of stress and energy," *Metals and Materials International*, vol. 20, pp. 375-388, 2014.

- [40] R. Vogt, Z. Zhang, M. Bonds, N. Browning, E. Lavernia and J. Schoenung, "The absence of thermal expansion mismatch strengthening in nanostructured metal–matrix composites," *Scripta Materialia*, vol. 61, pp. 1052-1055, 2009.
- [41] J. Ferguson, F. Sheykh-Jaberi, C.-S. Kim, P. Rohatgi and K. Cho, "On the strength and strain to failure in particle-reinforced magnesium metal-matrix nanocomposites (Mg MMNCs)," *Materials Science & Engineering A*, vol. 558, pp. 193-204, 2012.
- [42] T. Courtney, *Mechanical Properties of Materials*, Singapore: McGraw-Hill Book Co, 2000.
- [43] H. Ryu, S. Cha and S. Hong, "Generalized shear-lag model for load transfer in SiC/Al metal-matrix composites," *Journal of Materials Research*, vol. 18, pp. 2851-2858, 2003.
- [44] M.-K. Yeh, N.-H. Tai and J.-H. Liu, "Mechanical behavior of phenolic-based composites reinforced with multi-walled carbon nanotubes," *Carbon*, vol. 44, pp. 1-9, 2006.
- [45] M. Piggott, *Loading-bearing fiber composites*, Oxford: Pergamon, 1980.
- [46] K. Rajkumar and S. Aravindan, "Tribological behavior of microwave processed copper-nanographite composites," *Tribology International*, vol. 66, pp. 282-296, 2013.
- [47] A. Ghazaly, B. Seif and H. Salem, "Mechanical and tribological properties of AA2124-graphene self lubricating nanocomposite," *Light Metals*, pp. 411-415, 2013.
- [48] A. Dorri Moghadam, E. Omrani, P. Menezes and P. Rohatgi, "Mechanical and tribological properties of self-lubricating metal matrix nanocomposites reinforced by carbon nanotubes (CNTs) and graphene-A review," *Composites Part B*, vol. 77, pp. 402-420, 2015.

- [49] R. Petkovic-Luton and J. Vallone, "Exxon Research and Engineering Company". Florham Park, NJ, United States of America Patent US Patent Number 4619699, 1986.
- [50] M. Luton, C. Jayanth, M. Disko, S. Matras and J. Vallone, "Cryomilling of Nano-Phase Dispersion Strengthened Aluminum," *MRS Fall Meeting*, vol. 132, p. 79, 1988.
- [51] D. Witkin and E. Lavernia, "Synthesis and mechanical behavior of nanostructured materials via cryomilling," *Progress in Materials Science*, vol. 51, pp. 1-60, 2006.
- [52] E. Lavernia, B. Han and J. Schoenung, "Cryomilled nanostructured materials: Processing and properties," *Materials Science and Engineering A*, vol. 493, pp. 207-214, 2008.
- [53] J. Thornton, B. Han and E. Lavernia, "Grain Growth in Cryomilled Ni Powder during Degassing," *Metallurgical and Materials Transactions A*, vol. 38, pp. 1343-1350, 2007.
- [54] D. Witkin, B. Han and E. Lavernia, "Mechanical Behavior of Ultrafine-Grained Cryomilled Al 5083 at Elevated Temperature," *Journal of Materials Engineering and Performance*, vol. 14, pp. 519-527, 2005.
- [55] B. Han, J. Ye, F. Tang, J. Schoenung and E. Lavernia, "Processing and behavior of nanostructured metallic alloys and composites by cryomilling," *Journal of Materials Science*, vol. 42, pp. 1660-1672, 2007.
- [56] D. Witkin, B. Han and E. Lavernia, "Room-Temperature Mechanical Behavior of Cryomilled Al Alloys," *Metallurgical Materials Transactions A*, vol. 37, pp. 185-194, 2006.

- [57] H.-J. Fecht, "Nanostructure formation by mechanical attrition," *Nanostructured Materials*, vol. 6, pp. 33-42, 1995.
- [58] Z. Zhang, T. Topping, Y. Li, R. Vogt, Y. Zhou, C. Haines, J. Paras, D. Kapoor, J. Schoenung and E. Lavernia, "Mechanical behavior of ultrafine-grained Al composites reinforced with B₄C nanoparticles," *Scripta Materialia*, vol. 65, pp. 652-655, 2011.
- [59] R. Vogt, Z. Zhang, T. Topping, E. Lavernia and J. Schoenung, "Cryomilled aluminum alloy and boron carbide nano-composite plate," *Journal of Materials Processing Technology*, vol. 209, pp. 5046-5053, 2009.
- [60] Y. Li, W. Liu, V. Ortalan, W. Li, Z. Zhang, R. Vogt, N. Browning, E. Lavernia and J. Schoenung, "HRTEM and EELS study of aluminum nitride in nanostructured Al 5083/B₄C processed via cryomilling," *Acta Materialia*, vol. 58, pp. 1732-1740, 2010.
- [61] N. Koratkar, Graphene in Composite Materials, Synthesis, Characterization and Applications, Lancaster, Pensilvania, USA: DEStech Publication, 2013.
- [62] J. Ferguson, X. Thao, P. Rohatgi, K. Cho and C.-S. Kim, "Computational and analytical prediction of the elastic modulus and yield stress in particulate-reinforced metal matrix composites," *Scripta Materialia*, vol. 83, pp. 45-48, 2014.
- [63] J. Shackelford and W. Alexander, CRC Materials Science and Engineering Handbook, 3rd ed., Boca Raton, FL, USA: CRC Press, 2000.
- [64] J. Ferguson, B. F. Schultz, D. Venugopalan, H. F. Lopez, P. K. Rohatgi, K. Cho and C.-S. Kim, "On the superposition of strengthening mechanisms in dispersion strengthened alloys

- and metal matrix nano composites: Consideration of Stress and Energy," *Metals and Materials International*, p. Accepted, 2013.
- [65] G. Tatten and D. Mackenzie, Handbook of Al, New York, NY, USA: Marcel Dekker, 2003.
- [66] J. Kong, C. Xu, J. Li, W. Chen and H. Hou, "Evolution of fractal features of pores in compacting and sintering process," *Advanced Powder Technology*, vol. 22, pp. 439-442, 2011.
- [67] M. Tabandeh-Khorshid, J. Ferguson, B. F. Schultz, C.-S. Kim, K. Cho and P. K. Rohatgi, "Strengthening mechanisms of graphene- and Al₂O₃-reinforced aluminum nanocomposites synthesized by room temperature milling," *Materials and Design*, vol. 92, pp. 79-87, 2016.
- [68] M. Tabandeh-Khorshid, E. Omrani, P. L. Menezes and P. K. Rohatgi, "Tribological performance of self-lubricating aluminum matrix nanocomposites: Role of graphene nanoplatelets," *Engineering Science and Technology, an International Journal*, vol. 19, pp. 463-469, 2016.
- [69] M. Tabandeh-Khorshid, B. Schultz, P. Rohatgi and R. Elhajjar, "The Diametrically Loaded Cylinder For The Study Of Nanostructured Aluminum-Graphene And Aluminum-Alumina Nanocomposites Using Digital Image Correlation," *Frontiers in Materials*, vol. 3, 2016.
- [70] Z. Zhang, S. Dallek, R. Vogt, Y. Li, T. Topping , Y. Zhou, J. Schoenung and E. Lavernia, "Degassing behavior of nanostructured Al and its composites," *Metallurgical and Materials Transactions A*, vol. 41, pp. 532-541, 2010.

- [71] V. Kumar, T. Hanel, L. Giannini, M. Galimberti and U. Giese, "Graphene Reinforced Synthetic Isoprene Rubber Nanocomposites," *KGK rubberpoint*, vol. 67, pp. 38-46, 2014.
- [72] J. Ye, B4C Reinforced Nanocrystalline Aluminum Composites: Synthesis, Mechanical Behavior and Cost Analysis, University of California, Davis: Thesis, 2005.
- [73] C. Goh, J. Wei, L. Lee and M. Gupta, "Properties and deformation behavior of Mg-Y2O3 nanocomposites," *Acta Materialia*, vol. 55, pp. 5115-5121, 2007.
- [74] L. Dai, Z. Ling and Y. Bai, "Size-dependent inelastic behavior of particle-reinforced metal–matrix composites," *Composite Science and Technology*, vol. 61, pp. 1057-1063, 2001.
- [75] Z. Zhang and D. Chen, "strength, Consideration of Orowan strengthening effect in particulate-reinforced metal matrix nanocomposites: A model for predicting their yield," *Scripta Materialia*, vol. 54, p. 1321, 2006.
- [76] N. Hansen, "Hall–Petch relation and boundary strengthening," *Scripta Materialia*, vol. 51, pp. 801-806, 2004.
- [77] K. R. Van Horn, Aluminum Volume I. Properties, Physical Metallurgy and Phase Diagrams, Metals Park, Ohio: American Society For Metals, 1967.
- [78] D. Yoon, Y.-W. Son and H. Cheong, "Negative Thermal Expansion Coefficient of Graphene Measured by Raman Spectroscopy," *Nano Letters*, vol. 11, pp. 3227-3231, 2011.

- [79] K. Maung, J. C. Earthman and F. A. Mohammed, "Inverse Hall–Petch behavior in diamantane stabilized bulk nanocrystalline aluminum," *Acta Materialia*, vol. 60, pp. 5850-5857, 2012.
- [80] S. Guo, J. Qiu, P. Yu, S. Xie and W. Chen, "Fe-based bulk metallic glasses: Brittle or ductile?," *Applied Physics Letters*, vol. 105, p. 161901, 2014.
- [81] P. K. Rohatgi, M. Tabandeh-Khorshid, E. Omrani, M. Lovell and P. Menezes, "Tribology of Metal Matrix Composites," in *Tribology for Scientists and Engineers*, New York, Springer, 2013, pp. 233-268.
- [82] C. Guiderdoni, E. Pavlenko, V. Turq, A. Weibel, P. Puech, C. Estournes, A. Peigney, W. Bacsa and C. Laurent, "The preparation of carbon nanotube (CNT)/copper composites and the effect of the number of CNT walls on their hardness, friction and wear properties," *Carbon*, vol. 58, pp. 185-197, 2013.
- [83] P. L. Menezes, M. Nosonovsky, S. Kailas and M. Lovell, "Friction and Wear," in *Tribology for Scientists and Engineers: From Basics to Advanced Concepts*, New York, Springer, 2013, pp. 43-91.
- [84] M. Kozma, "Friction and wear of aluminum matrix composites," in *National Tribology Conference*, Galati, Romania, 2003.
- [85] R. A. Al-Samarai, Haftirman, K. R. Ahmad and Y. Al-Douri, "Evaluate the Effects of Various Surface Roughness on the Tribological Characteristics under Dry and Lubricated

- Conditions for Al-Si Alloy," *Journal of Surface Engineered Materials and Advanced Technology*, vol. 2, pp. 167-173, 2012.
- [86] P. L. Menenzes, Kishore and S. Kailas, "studies on friction and transfer layer using inclined scratch," *Tribology International*, vol. 39, pp. 175-183, 2006.
- [87] M. Cowap, S. Moghaddam, P. L. Menzes and K. Beschorner, "Contributions of adhesion and hysteresis to the coefficient of friction between shoe and floor surfaces: effects of floor roughness and sliding speed," *Tribology - Materials, Surfaces & Interfaces*, vol. 9, pp. 77-84, 2015.
- [88] P. L. Menzes, P. K. Rohatgi and M. Lovell, "Self-Lubricating Behavior of Graphite Reinforced Metal Matrix Composites," in *Green Tribology*, Springer Berlin Heidelberg, 2012, pp. 445-480.
- [89] P. Hung and A. Voloshin, "In-plane strain measurement by digital image correlation," *Journal of the Brazilian Society of Mechanical Sciences and Engineering*, vol. 25, pp. 215-221, 2003.
- [90] S. Shams and R. El-Hajjar, "Effects of scratch damage on progressive failure of laminated carbon fiber/epoxy composites," *International Journal of Mechanical Sciences*, vol. 67, pp. 70-77, 2013.
- [91] R. El-Hajjar, S. Shams and D. Kehrl, "Colsed form solutions for predicting the elastic behavior of quasi-isotropic triaxially braided composites," *Composite Structures*, vol. 101, pp. 1-8, 2013.

- [92] N. Muskhelishvili, Some basic problems of the mathematical theory of elasticity, 2013.
- [93] H. Hertz, W. Gesammelte and I. Leipzig, "Also Ueber die Beruehrung festes elastisches Koerper," *Journal of Fuer Mathematik*, vol. 92, p. 156, 1882.
- [94] Y. Jianhong, F. Wu and J. Sun, "Estimation of the tensile elastic modulus using Brazilian disc by applying diametrically opposed concentrated loads," *International Journal of Rock Mechanics and Mining Sciences*, vol. 46, pp. 568-576, 2009.

7. CURRICULUM VITAE

Meysam Tabandeh-Khorshid

Place of birth: Shiraz, Iran

Education

B.Sc., Islamic Azad University Najafabad Branch, July 2006

Major: Materials Science and Engineering

M.Sc., Shiraz University, July 2010

Major: Materials Science and Engineering

Teaching Experiences

- Instructor of MATLENG-411: Materials Laboratory (Fall 2014)
- Teaching Assistant of MATLENG-201: Engineering Materials (Fall 2012-Spring 2014 & Spring 2015)
- Teaching Assistant of MATLENG-457: Composite Materials (Spring 2014)
- Teaching Assistant of MATLENG-490: Senior Design (Spring 2014 & Spring 2015)
- Teaching Assistant of MATLENG-411: Materials Laboratory (Fall 2013)
- Teaching Assistant of MATLENG-465: Friction and Wear (Fall 2013)
- Teaching Assistant of MATLENG-511: Advanced Materials Characterization (Fall 2013)

Honors & Awards

2016	Academic Excellence Award-University of Wisconsin Milwaukee
2016	American Foundry Society (AFS) Northeastern Wisconsin Scholarship
2016	Foundry Education Foundation (FEF) Scholarship
2015-2016	Distinguished Dissertation Fellowship-University of Wisconsin Milwaukee
2015	1 st Annual Spoon, Cup & Saucer Casting Competition-AFS Wisconsin Chapter
2012 & 2014	Two Chancellor Awards-University of Wisconsin Milwaukee
2012	Research Assistantship-University of Wisconsin Milwaukee

Publications

International Journal

1. **Meysam Tabandeh-Khorshid**, Benjamin F. Schultz, Pradeep K. Rohatgi, Rani ELhajjar, *Diametrical loaded cylinder for study of nanostructured aluminum-graphene and aluminum-alumina nanocomposites using digital image correlation*, Frontiers in Materials-Composite Materials, 2016; 3, 22-30.
2. **Meysam Tabandeh-Khorshid**, J.B. Ferguson, Benjamin F. Schultz, Chang-Soo Kim, Kyu Cho, Pradeep K. Rohatgi, *Graphene and Al₂O₃ Reinforced Nano-Crystalline Aluminum Nanocomposites Synthesized by Room Temperature Milling*, Materials & Design, 2016; 92, 79-87.
3. **Meysam Tabandeh-Khorshid**, Emad Omrani, Pradeep L. Menezes, Pradeep K. Rohatgi, *Tribological performance of self-lubricating aluminum matrix nanocomposites: Role of graphene nanoplatelets*, Engineering Science and Technology, an International Journal.

4. J.B. Ferguson, **Meysam Tabandeh-Khorshid**, John Mantas, Pradeep Rohatgi, Kyu Cho, Chang-Soo Kim, *Predicting the Effect of Pouring Temperature on the Crystallite Density, Remelting, and Crystal Growth Kinetics in the Solidification of Aluminum Alloys*, Metallurgical and Materials Transactions B, DOI: 10.1007/s11663-014-0044-9.
5. J.B. Ferguson, **Meysam Tabandeh-Khorshid**, Pradeep Rohatgi, Kyu Cho, Chang-Soo Kim, *Predicting Tensile and Compressive Mechanical Properties of Bimodal Nano-Aluminum Alloys*, Scripta Materialia, 2014; 72–73, 13–16.
6. Reza Derakhshandeh.H, Amir Moresedegh, S. A. Jenabali Jahromi and **Meysam Tabandeh-Khorshid**, *A Comparison Between Equal Channel Angular Pressing (ECAP) and Conventional Extrusion for Consolidation of Aluminum Metal Matrix Composite*, Journal of Materials Engineering and Performance, 2012; 21, 1885–1892.
7. **Meysam Tabandeh-Khorshid**, S. A. Jenabali Jahromi, M. M. Moshksar, *Mechanical properties of tri-modal Al matrix composites reinforced by nano- and submicron-sized Al_2O_3 particulates developed by wet attrition milling and hot extrusion*, Materials & Design, 2010; 31, 3880-3884.
8. **Meysam Tabandeh-Khorshid**, Benjamin F. Schultz, Pradeep K. Rohatgi, *Graphene reinforced Metal Matrix nano-Composites: Synthesis, Characterization and Properties-A Review*, Submitted to Composites Part B: Engineering.

Book Chapter

1. P.L. Menezes, S. Ingole, M. Nosonovsky, S.V. Kailas, M.R. Lovell, "Tribology for Scientists and Engineers", 2013, X, 946 p., Springer, ISBN 978-1-4614-1944-0; Jan 2014. Chapter 8: Pradeep K. Rohatgi, **Meysam Tabandeh-Khorshid**, Emad Omrani, Michael R. Lovell, and Pradeep L. Menezes, "Tribology of Metal Matrix Composite"

Presentations

1. Steven Eric Zeltmann, Nikhil Gupta, **Meysam Tabandeh-Khorshid**, Pradeep K. Rohatgi, *Compressive characterization of ZA8 matrix glass hollow microsphere syntactic foams at quasi-static and high strain rates*, 9th Pacific Rim International Conference on Advanced Materials and Processing (PRICM9), Kyoto, Japan, August 2016.
2. **Meysam Tabandeh-Khorshid**, and Pradeep K. Rohatgi, *Developing a new method to synthesize of nanocrystalline Metal Matrix Nanocomposites reinforced by graphene or nanoalumina and investigating their mechanical properties*, 2016 CEAS Research Poster Competition, University of Wisconsin-Milwaukee, Milwaukee, WI, USA, April 2016.
3. **Meysam Tabandeh-Khorshid**, Emad Omrani, Pradeep L. Menezes, Pradeep K. Rohatgi, *Self-Lubricating Aluminum Matrix Nanocomposites Reinforced by Graphene Nanoplatelets*, TMS 2016, 145th Annual Meeting & Exhibition, Nashville, TN, USA, February 2016.
4. **Meysam Tabandeh-Khorshid**, Hydrophobicity and Oleophobicity in Metallic Alloys and Composites, Invited Talk, Isfahan University of Technology, Isfahan, Iran, December 2015.
5. **Meysam Tabandeh-Khorshid**, *Characterization of Al/Graphene nanoplatelets MMNCs synthesized by powder metallurgy*, Poster session at 32 Annual Metallography and Materials Characterization Contest, ASM-Milwaukee chapter, Milwaukee, WI, USA, May 2015.
6. **Meysam Tabandeh-Khorshid**, J. B. Ferguson, B.F. Schultz, Pradeep K. Rohatgi, *Exfoliating graphene nanoplatelets and preparing alumina/exfoliated graphene composite powders by mechanical milling*, 2014 CEAS Research Poster Competition, University of Wisconsin-Milwaukee, Milwaukee, WI, USA, April 2014.

7. **Meysam Tabandeh-Khorshid**, S. A. Jenabali Jahromi, M. M. Moshksar, *Synthesizing aluminum-alumina nanocomposite by attritor mill in wet atmosphere and investigating its mechanical properties*, The 2nd National Nano Materials & Nano Technology Conference, Islamic Azad University Najafabad Branch, Najafabad, Iran, May 2010.
8. **Meysam Tabandeh-Khorshid**, S. A. Jenabali Jahromi, *Synthesis and investigating the mechanical properties of aluminum matrix composite reinforced by nano- and sub micron-size alumina*, 7th Nano Technology Conference, Tarbiat Modares University, Tehran, Iran, May 2010.

Professional Organization Activities

- Session Chair-Metal and Polymer Matrix Composites, TMS2016, Feb 2016, Nashville, TN
- Member of Material Advantage (The Student Program for Materials Science and Engineering)
- Member of American Foundry Society (AFS)
- Member of Foundry Education Foundation (FEF)